Spring 1-1-2017

An Investigation of Engineered Injection and Extraction as an in Situ Remediation Technique for Uranium-Contaminated Groundwater

John Arthur Greene
University of Colorado at Boulder, john.greene@colorado.edu

An investigation of Engineered Injection and Extraction as an in situ remediation technique for uranium-contaminated groundwater

by

John A. Greene

B.S., University of Colorado, 2017

A thesis submitted to the

Faculty of the Graduate School of the

University of Colorado in partial fulfillment

of the requirements for the degree of

Master of Science

Department of Civil, Environmental, and Architectural Engineering

2017

This thesis entitled:
An investigation of Engineered Injection and Extraction as an in situ remediation technique for uranium-contaminated groundwater
written by John A. Greene
has been approved for the Department of Civil, Environmental, and Architectural Engineering

Prof. Roseanna M. Neupauer

Prof. Joseph R. Kasprzyk

Prof. Joseph N. Ryan

Date

The final copy of this thesis has been examined by the signatories, and we find that both the content and the form meet acceptable presentation standards of scholarly work in the above mentioned discipline.

Greene, John A. (M.S., Civil Engineering)

An investigation of Engineered Injection and Extraction as an in situ remediation technique for uranium-contaminated groundwater

Thesis directed by Prof. Roseanna M. Neupauer

During *in situ* remediation of contaminated groundwater, a treatment chemical is injected into the contaminated groundwater to degrade a contaminant through chemical reaction that occurs in the subsurface. Reactions and subsequent contaminant degradation occur only where the treatment chemical contacts the contaminant long enough to complete degradation reactions. Traditional *in situ* groundwater remediation relies on background groundwater flow to spread an injected treatment chemical into a plume of contaminated groundwater.

Engineered Injection and Extraction (EIE), in which time-varying induced flow fields are used to actively spread the treatment chemical into the contaminant plume, has been developed to increase contact between the contaminant and treatment chemical, thereby enhancing contaminant degradation. EIE has been investigated for contaminants degrading through irreversible, bimolecular reaction with a treatment chemical, but has not been investigated for a contaminant governed by complex biogeochemical processes. Uranium fate and transport in subsurface environments is governed by adsorption, oxidation reduction, solution, and solid-phase interactions with naturally occurring solution species, microbial communities, minerals and aquifer media. Uranium primarily occurs in aqueous, mobile U(VI) complexes in the environment but can be reduced to sparingly soluble, immobile U(IV) solid-phase complexes by native dissimilatory metal reducing bacteria.

This work investigates the ability of EIE to promote subsurface delivery of an acetate-amended treatment solution throughout a plume of uranium-contaminated groundwater to promote *in situ* growth of native microbial communities to immobilize uranium. Simulations in this investigation are conducted using a semi-synthetic flow and reactive transport model based on physical and biogeochemical conditions from two uranium contaminated sites: the Naturita Uranium

Mill Tailings Remedial Action (UMTRA) Project site in southwestern Colorado and the Old Rifle UMTRA Project site in western Colorado.

Dedication

To my late grandfather, Leslie E. Howell.

Acknowledgements

I would like to thank Roseanna Neupauer for being the best advisor, mentor, and motivator, for giving me my first gig as a researcher and for pushing me to give presentations at conferences and submit a paper as an undergraduate. I would also like to thank Joe Kasprzyk for being a wonderful resource, and mentor throughout the past few years at CU and Joe Ryan for being a member of my committee, along with the two aforementioned, and being a great undergraduate advisor, who first introduced this newfound passion for reclamation of legacy mining activity in the American West. I am grateful for Amy Piscopo for mentoring me as an undergraduate researcher and teaching me about EIE, groundwater modeling, and research in general. I wouldn't be here without Fernando Rosario-Ortiz pushing me to apply for the B.S./M.S. program despite my lack of interest in graduate school at the time. I am grateful for Ming Ye, Gary Curtis and Steven Yabusaki for developing the precursor models from which my model for this work is based and for being irreplaceable resources in learning to use the PHREEQC/PHT3D framework. I love my parents, Jim and Lucinda, and my sister, Nora, for their undying love and support.

I am grateful for funding from the Division of Earth Sciences of the National Science Foundation through grant: EAR-1552351. This work utilized the RMACC Summit supercomputer, which is supported by the National Science Foundation (awards ACI-1532235 and ACI-1532236), the University of Colorado Boulder, and Colorado State University. The Summit super computer is a joint effort of the University of Colorado Boulder and Colorado State University.

Contents

Chapter

Tables

Table

Figures

Figure

Chapter 1

Introduction

Remediation of uranium in the subsurface environment is complicated due to the complex kinetic, adsorption, and oxidation reduction biogeochemical processes governing its fate and transport in groundwater. A technique recently developed for enhancing subsurface remediation called Engineered Injection and Extraction (EIE) has shown promising results for enhanced *in situ* degradation of contaminated groundwater. The technique promotes increased contact between an injected treatment chemical and the contaminant through selective pumping and recharge of clean water increasing contaminant degradation efficiency. This work investigates EIE for its ability to remediate a uranium contaminant governed by complex biogeochemistry with enhancements from biogeochemical models from field investigations on legacy uranium-contaminated sites in Naturita, Colorado and Rifle, Colorado.

1.1 Motivation

The motivation for this project is to investigate a novel *in situ* groundwater remediation technique to immobilize uranium in contaminated groundwater still present at many sites throughout the American West. Throughout this region, many legacy mine, mill and processing sites are contaminated with uranium. Uranium contamination at these sites covers large areas of the surface and subsurface. Uranium present on the surface as tailings and legacy infrastructure has been largely remediated. However, uranium leached into underlying aquifers from precipitation infiltration has been left to naturally attenuate at many sites primarily due to high cost.

The onset of nuclear weapons development in the United States during World War II and into the Cold War produced large volumes of hazardous waste from uranium mining and processing activities [151]. Processing of uranium ores removed only 15% of radioactivity initially present in extracted material. Radon gas and other radioactive heavy metals present in processed ores can be mobilized through wind into air or through runoff to surface water or leaching into underlying aquifers. These materials are produce gamma radiation, which is extremely hazardous to human and environmental health [171, 151]. During the first few decades of significant uranium extraction in the early 1940s, negligible effort was made to contain the introduction of radioactive material into the surrounding environment as federal law did not recognize uranium tailings as radioactive waste until the late 1970s. As a result, 50 sites throughout the US, almost exclusive to the American West, housed radioactive tailings from uranium mining and processing activities [151].

In 1978, the Uranium Mill Tailings Radiation Control Act (UMTRCA) tasked the US Department of Energy (DOE) with the long-term monitoring of the affected sites: 24 abandoned sites were the responsibility of the DOE to remediate and responsibility of 28 others, active at the time, will be transferred to the DOE following remediation by their owners [151]. In association with the 22 sites under the responsibility of the DOE for remediation, an additional 5,276 nearby sites were contaminated as a result of uranium mining, processing and lackluster tailings disposal [163].

Under the DOE's Uranium Mill Tailings Remedial Action (UMTRA) Project, remediation consisted of two phases, tailings and associated material stabilization, which the DOE conducted by constructing and disposing of such material in 19 engineered disposal cells on or near the processing sites [123, 163, 122]. The disposal cells collectively contain approximately 40 million cubic yards of material, about equivalent to a city block piled 14-stories tall with processed tailings and legacy infrastructure [122]. The DOE conducted soil remediation between 1979 – 1998 and groundwater associated work began in 1991[163]. By 2003, the DOE implemented supplementary standards for groundwater Maximum Contaminant Levels (MCLs), institutional controls on land and water use, and were remediated via passive natural attenuation [151]. A handful of sites in northwest New Mexico and northeast Arizona required active groundwater remediation [151]. As of the end of

fiscal year 1999, the UMTRA Project had spent 1.5 billion USD [5]. The projected total annual cost of long-term stewardship associated with supplemental standards was estimated to cost 2.2 million USD per year. Additionally, the cost of required active remediation is projected to cost over 50 million USD per year through 2025 [151].

1.2 Uranium

Uranium is comparatively abundant on Earth relative to other metals – 40 times more than silver, and 500 times more than gold; however, it is dispersed throughout the globe [40]. Uranium occurs in increased concentrations in rocks with higher silica content, e.g. granites, shale, and phyllosilicate (layered-silicate) natural sediments [90, 40]. The International Atomic Energy Agency (IAEA) classifies uranium deposit types in fifteen different categories, but uranium deposited in sandstone formations in the Colorado Plateau are most relevant to this work [11]. Mineralized sandstone confined by impermeable shale/mudstone contains carbonaceous material, sulfides, hydrocarbons and volcanic ash with ferro-magnesian minerals. These constituents react in oxidation reduction reactions with hexavalent uranium species, U(VI), to form tetravalent uranium, U(IV). U(VI) forms strong aqueous species and is therefore mobile in the environment. However, when reduced, U(IV) forms strong solid-phase species and becomes immobile in the environment. On a geologic timescale, uranium has accumulated in mineralized sandstone deposits through oxidation reduction reactions with the aforementioned materials to form solid-phase uranium species. These types of deposits house approximately 18% of world uranium resources and account for the majority of the domestic uranium resources in the United States [11].

Gold prospectors discovered the first uranium deposit in the United States outside of a Central City, Colorado gold mining operation in 1871. The region produced 50 tons of high grade ore between 1871 and 1895. However, the majority of the domestic uranium production prior to World War II was extracted from uranium/vanadium deposits in the Colorado Plateau. Following WWII, demand for uranium was created solely by the US Atomic Energy Commission (US AEC) [29]. The steady demand facilitated a uranium mining boom in the American Southwest that replaced

a much smaller radium and vanadium mining industry present in the area [29]. Vanadium and radium operations were easily updated to incorporate uranium extraction because the three metals have similar characteristics and are found the same mineral deposits [71, 150]. During the peak of uranium mining in the Colorado Plateau, approximately 750 mines were in operation [53, 126]. The US AEC continued as the sole proprietor of uranium until 1971 when the US government began to allow private entities to buy uranium primarily for nuclear power. Commercial purchasers eventually took over the demand created by the US AEC by 1971, which remained until the market crashed largely due to the Three-Mile Island accident in 1979 [77, 117].

1.2.1 Uranium in the environment

Of all actinide elements, elements with molecular weights between 89 – 103 amu, only thorium (Th) and uranium (U) are primordial, having a long enough half-lives to have existed in their current form before the formation of the Earth and not decayed since then. As a result of their extremely long half-lives, uranium and thorium are the most abundant actinides in the natural environment. All non-anthropogenically enriched uranium in the natural environment are assumed to be $^{238}_{92}$U, which is non-fissile, or unable to sustain chain reactions. None of the daughter products of $^{238}_{92}$U are relevant due to excessively long time scale on which $^{238}_{92}$U decays. The first step in the radioactive decay series of U is

$$^{238}_{92}\mathrm{U} \xrightarrow[4.51\times10^{9}\ \mathrm{y}]{\alpha} {}^{234}_{90}\mathrm{Th}, \tag{1.1}$$

which shows the α-decay of $^{238}_{92}$U is slow [90].

Uranium occurs naturally in seawater and natural surface and subsurface waters in concentrations on the order of μg/L [90]. Naturally occurring uranium is found in three oxidation states: U(IV), U(V), and U(VI) [90]. U(V) occurs as the $UO_2{}^+$ ion and forms weak aqueous complexes compared to those formed by U(IV) and U(VI) [66]. U(IV) and U(VI) are the two most common natural oxidation states of uranium. In aqueous oxidized surface and groundwater environments, uranium most commonly occurs in the U(VI) oxidation state in aqueous uranyl $UO_2{}^{2+}$ complexes. Uranyl is highly soluble and therefore mobile in aquatic environments. Uranyl-carbonate and

uranyl-hydroxide species account for the majority of uranium present in aqueous systems [90].

In terms of fate and transport of uranyl in natural environments, uranyl-carbonate species are the most important in governing uranium complexation, sorption, and mobility. The formation of uranyl-carbonate species is influenced by aqueous pH and partial pressure of CO_2. In solutions with pH $>$ 6, uranyl-carbonate species account for the majority uranium mass in the system. Uranyl-carbonate complexes form strong species and have great influence on the fate and transport of uranium in natural waters. Uranyl-carbonate species are more thermodynamically stable than uranium contained in mineral species or adsorbed to aquifer media. With the addition of carbonate into aqueous subsurface environments, uranium in mineral and surface species dissolves and forms uranyl-carbonate species. These uranyl-carbonate species are mobile in the environment, traveling with ambient groundwater flow [90].

Adsorption of uranium to aquifer media aids in the attenuation of uranium in subsurface aqueous environments [130, 112]. In solutions at circumneutral pH, high alkalinity can inhibit the adsorption of U(VI) to aquifer media [111, 48]. pH and competition of U(VI) between sorption sites and the formation of $Ca-U(VI)-CO_3$ complexes influence U(VI) adsorption in groundwater systems [186, 62, 110, 101, 158, 28, 97, 164]. Ambient chemical concentrations and pH influence the distribution of uranium between aqueous and adsorbed phase [47, 37, 174]. Kohler et al. [86] found a decrease in uranium adsorption in solutions with fluoride in column experiments. Uranium and fluoride form strong aqueous complexes which decreases the affinity of uranium to adsorb to porous media[86]. Davis and Curtis [47] found that field-scale adsorption modeling of U(VI) at the former uranium and vanadium processing site outside of Naturita, CO, is highly dependent on alkalinity. They concluded surface reactions, and therefore their predictions of fate and transport of uranium, could be highly dependent on pH or concentrations of other geochemically prevalent ligands.

Adsorbent surfaces can provide sites for oxidation/reduction reactions. Singer et al. [157] found the speciation of uranium species adsorbed to magnetite (an iron-oxide mineral) surfaces depends on the relative abundance of ferric (Fe(II)) iron present in the magnetite surface. Iron

primarily occurs as ferric or ferrous iron (Fe(III)), so lower Fe(III) content indicates elevated indicates higher Fe(II) content on the magnetite surfaces. Reduced iron (Fe(II)) can act as an acceptor donor for oxidation reduction reactions [157]. Singer et al. [157] found that magnetite surfaces with higher Fe(II) content also contained higher reduced uranium U(IV) species. Latta et al. [91] further investigated surface reduction of U(VI) on magnetite. The reduced form of uranium, U(IV), was believed to form only crystalline solid phases (i.e. uraninite UO_2) upon creation in the subsurface environment [76, 13, 30]. Recently, vast evidence has been presented for less organized (and therefore less stable) U(IV) phases as a result of biotic or abiotic reduction of U(VI) by various reducing agents. Work by Latta et al. [91] is broadly focused on characterizing the process and geochemical conditions leading to the formation of crystalline UO_2 and those promoting the formation of non-uraninite U(IV) species. In terms of magnetite-promoted reduction, Latta et al. [91] found that with increased fractions of Fe(II) in magnetite minerals, more Fe(II) acts as a reducing agent for U(VI), and therefore more uranium occurs as U(IV) species [91].

Aside from forming aqueous complexes with ligands, U(VI) interacts with sulfide-containing minerals, e.g. mackinawite (FeS) and pyrite (FeS_2) [183, 25, 14, 176, 51, 76, 91, 157, 125, 3, 75, 20, 107, 70, 99, 19]. Wersin et al. [176] was one of the early groups to report the interaction of U(VI) and sulfide minerals based on spectroscopic imaging of uranium-containing samples. Bargar et al. [14] and Bone et al. [25] used various image processes to categorize sediments collected following an *in situ* bioremediation study conducted at the uranium-contaminated aquifer at the Rifle Integrated Field Research (IFRC) site in Rifle, Colorado. Bargar et al. [14] proposed two redox pathways responsible for the formation of solid-phase U(VI) following an acetate amendment. Bargar et al. [14] found approximately 75% of U(IV) was formed through reduction by FeS while the rest of the U(IV) mass formed precipitated as crystalline uraninite ($UO_{2(s)}$). Grain-scale association of non-uraninite U(IV) and FeS presented in Bargar et al. [14] shows U(VI) is abiotically reduced by FeS confirmed by other work [176, 51, 76, 91, 157, 125] showing FeS and other ferrous sulfides act as a reducing agent for U(VI). However, Bargar et al. [14] found grain-scale association between uranium and FeS, but the relationship broke down at micrometer scales. As a result, Bargar et

al. [14] proposed that non-uraninite U(IV) forms in U(IV)$-PO_4$ aqueous complexes, solids, and polymers linked to biomass, concluding that in the absence of biomass pure crystalline uraninite formation would be expected.

Bone et al. [25] proposes that adsorption of non-uraninite U(IV) species competes with the formation of U(IV)-containing minerals, i.e. crystalline uraninite. As a follow up to Bargar et al. [14], Bone et al. [25] proposes the existence of reduction hot spots, which include cell aggregates, organic matter, FeS and aluminosilicates, all of which promote the reduction of ambient U(VI) to U(VI) species. Once reduced, U(IV) adsorbs to ligands from cell aggregates inhibiting the formation of crystalline uraninite [25].

U(IV) has also been shown to adsorb to metal surfaces: Latta et al. [94], and Wang et al. [175] both investigated the adsorption of U(IV) to rutile (TiO_4), magnetite ($Fe^{II}Fe_2{}^{III}O_4$) and hematite ($Fe_2{}^{III}O_3$). Much like reduction hot spots presented in Bone et al. [25], Latta et al. [94] proposes that rutile serves as either a high or low affinity site for uranium oxidation reduction (redox) reactions via two mechanisms. The first mechanism is the adsorption of U(VI) to high affinity sites allowing microorganisms to perform electron transfer, while uranium stays adsorbed to inner-sphere rutile sites. The second mechanism consists of low affinity outer-sphere sites where U(VI) can adsorb and undergo reduction via microbial activity and then detach [94]. The first mechanism would most likely produce adsorbed U(IV), while the second pathway would most likely form crystalline uraninite [94].

Wang et al. [175] created a surface complexation model for rutile, magnetite and hematite surfaces adsorbing U(IV) and found that at circumneutral pH rutile exhibited the most coverage and magnetite exhibited an order of magnitude lower amount of surface loading. However, Wang et al. [175] concludes that adsorption of U(IV) to high affinity metal sites can be a significant sink of uranium in natural subsurface environments [175].

Biotic processes can reduce U(VI) to U(IV) as well – Lovley et al. [101] found that dissimilatory iron-reducing organisms effectively use U(VI) as a terminal electron acceptor in their metabolism, which was proven by an experiment showing more extensive and rapid reduction of

U(VI) in biologically amended sediments compared to similar sediments relying on abiotic reduction processes [101].

Uranium lingers in subsurface environments because of the lack of electron donating compounds available to promote microbial activity. Microbial activity converts U(VI) into immobile U(IV) phases and consumes oxidants, which contribute to the re-mobilization of U(IV) phases. Microbial activity is also very dependent on the complex cycles of carbon and nitrogen [183]. Microbial activity introduces bicarbonate species, which promote the removal of adsorbed U(VI) species increasing the mobility of uranium in subsurface environments [183, 180, 54]. Bioavailable carbon produced from fermenters promotes further microbial activity of sulfate-, iron- and nitrate-reducers, which produce sulfide, ferric iron and nitrite, respectively [183]. Iron reducers also produce reduced, immobile uranium in as solid-phase U(IV). However, nitrite promotes re-oxidation of U(IV) back into its mobile, U(VI) valence state. Nitrate (NO_3^-) in the vadose zone is produced through nitrification of ammonium (NH_4^+) and nitrite (NO_2^-) by obligate aerobic autotrophic reactions [183]. Although DO and nitrite are absent in the saturated, naturally reduced zone (NRZ), DO and nitrate are introduced into the underlying aquifer through percolation of spring runoff and denitrification occurring above the NRZ, respectively [183]. Uranium is present in the NRZ as surface-complexed monomeric species of U(IV) [175, 14, 183]. U(IV) has many potential oxidants: DO, nitrate, and Fe(III); direct biotic oxidation by denitrifying bacteria or indirect biotic oxidation (i.e. by Fe(III) produced from nitrate mitigated oxidation of Fe(II)) [16, 17]. In subsurface environments, U(IV) is reductively desorbed to form aqueous U(VI) species promoted by aqueous nitrite from microbial activity and DO [183].

1.3 Remediation of contaminated groundwater

Many methods for remediating uranium contaminated groundwater exist. Methods can be grouped by the area where treatment occurs: *ex situ* remediation involves treatment of the contaminated groundwater at the surface via pumping water from the subsurface, treating it, and disposing of it appropriately, also known as "pump and treat." *In situ* remediation stimulates the

treatment, degradation or immobilization of contaminants in the subsurface.

1.3.1 *Ex situ* remediation

Advantages of *ex situ* remediation include the ability to completely monitor the quality of all of contaminated water treated and to provide adequate mixing needed to promote high amounts of contaminant degradation. Disadvantages of *ex situ* include treatment infrastructure needs and careful handling of potentially hazardous contaminants pumped from the subsurface. Often, once contaminants are pumped to the surface, contaminated water cannot be re-injected for disposal. According to the United States Government Accountability Office [124], experts believe *ex situ* technologies are best in the cases where:

- the contaminant is deep in the subsurface making site characterization and remediation "prohibitively expensive,"
- the geology of the site is complex enough to limit the effectiveness of *in situ* technologies (e.g., highly fractured systems),
- *in-situ* approaches are not viable to remediate a site (e.g., chlorinated solvents in fractured bedrock),
- the interim goal is containment of the plume, while an *in situ* system is being developed, or
- an *ex situ* system is needed to enhance an *in situ* system.

Because of the performance limitations and high cost of *ex situ* systems, interest and research has increased in developing *in situ* methods [156, 124]. According to Siegrist et al. [156], remediation using pump-and-treat alone is virtually impossible. Because of the ineffectiveness of pump and treat alone, there has been increased interest, and development of *in situ* remediation methods [124, 83]

1.3.2 *In situ* remediation

In situ systems stimulate degradation reaction pathways involving the contaminant and an introduced treatment chemical amendment. Common groundwater contaminants include nutrients, heavy metals and organics, which can be introduced to the subsurface from gasoline stations, dry cleaners, manufacturing plants, energy generation facilities, mining operations, disposal facilities, and nuclear and military installations among others [156]. Contaminants can be remediated through a series of reaction pathways, which include oxidation, reduction, attenuation, air sparging, phytoremediation, aerobic cometabolism, or thermal treatments producing less harmful products [166, 124].

In situ remediation avoids surface handling of potentially hazardous chemicals at the surface, and the need to construct treatment infrastructure needed for pump and treat systems. However, *in situ* systems are limited by incomplete mixing of the treatment chemical amendment and the contaminant because they rely on ambient groundwater flow to provide spreading of the treatment chemical into the contaminant plume[105, 113, 114, 138, 136]. The efficiency of *in situ* systems is often limited due to incomplete spreading of the treatment chemical throughout the contaminant plume promoted by ambient groundwater flow.

1.3.3 Engineered Injection and Extraction

Mays and Neupauer [105] presented a novel method called Engineered Injection and Extraction (EIE) for spreading a treatment chemical into a contaminant plume during *in situ* remediation of contaminated groundwater. In EIE, injection and extraction of clean water creates unsteady flow fields that enhance the spreading of the treatment chemical into the contaminant plume [105]. A 12-step heuristic sequence of injection and extraction at one well per step was developed to produce chaotic advection to enhance spreading of the treatment chemical into the contaminant plume. Mays and Neupauer [105] investigated EIE for a non-sorbing governed by irreversible, instantaneous

bimolecular reaction given as

$$C_1 + C_2 \rightarrow C_3 \tag{1.2}$$

where C_1 is the treatment chemical, C_2 is the contaminant, and C_3 is the reaction product. They found that by strategically extracting and injecting clean water at wells surrounding a plume of contaminated groundwater, the unsteady flow field stretched and folded the fluid interface, where the two chemicals are in close proximity [105].

Piscopo et al. [138] evaluated the degradation promoted by EIE, and found that EIE facilitated higher contaminant degradation in both homogeneous and heterogeneous aquifers than a remediation scheme that relied on passive spreading by ambient groundwater flow.

Piscopo et al. [138] also found that while heterogeneity also produces spreading (and therefore promotes contaminant degradation), the increased spreading and contaminant degradation due to EIE exceeds the contaminant degradation promoted by aquifer heterogeneity [138].

Neupauer et al. [114] further investigated the effect of aquifer heterogeneity on the success of EIE. They found that EIE schemes are more effective in heterogeneous aquifers because of the additional spreading caused by the spatial variability in aquifer properties. Neupauer et al. [114] also found that cumulative contaminant degradation promoted by the EIE sequence increases at a slower rate as heterogeneity in the aquifer increases [114].

Piscopo et al. [136] performed an optimization of the EIE sequence using the Borg multi-objective evolutionary algorithm (MOEA) to maximize the amount of contaminant degraded, while minimizing energy used for injection and extraction and the amount of treatment chemical used [136]. They found that many of the sequences outperformed the heuristic sequence of from Mays and Neupauer [105], although some sequences spread the plume a considerable distance through the aquifer.

Greene [65] investigated relationships between the size and distribution of the contaminant plume and separation distance between the wells. Greene [65] found increasing plume sizes need larger well separation distance to achieve the maximum amount of contaminant degradation possi-

ble. This relationship increases more quickly with increasingly uniform distributions of contaminant within the contaminant plume. Greene [65] found that cumulative contaminant degradation was higher for plumes with the contaminant more centrally concentrated, or less uniformly distributed.

Subsequent EIE investigations by Neupauer and Mays [113] and Piscopo et al. [137] investigated contaminants governed by kinetic degradation reactions and adsorption to aquifer media. Neupauer and Mays [113] found that an EIE remediation system with a longer treatment chemical injection period can achieve complete degradation of a contaminant governed by instantaneous degradation reactions and adsorption. In this system, a plume of injected treatment chemical overtakes the contaminant plume due to contaminant retardation from adsorption. As the treatment chemical overtakes the contaminant plume, contaminant is degraded. Neupauer and Mays [113] found that for a contaminant governed by equilibrium sorption and rate-limited degradation, nearly complete degradation of the contaminant can be achieved if the remediation time period is scaled with the inverse of the dimensionless rate constant, $k^* \approx 50$, given by

$$k^* = k_a C_1' T_{inj} \tag{1.3}$$

where k_a is the reaction rate constant for the aqueous contaminant and C_1 is the concentration of the aqueous contaminant [113].

Through this work, Neupauer and Mays [113] investigated the bounds of EIE's effectiveness on different types of contaminant transport. On one end, the contaminant is completely aqueous and therefore non-sorbing. Mays and Neupauer [105], and Piscopo et al. [138, 136] concluded that the strategy for remediating a non-sorbing contaminant was to stretch and fold the aqueous fluid interface to promote increased contact of the aqueous contaminant and treatment chemical. On the other end of the spectrum, a contaminant governed by linear equilibrium sorption, is less mobile and there is less need to stretch and fold the fluid interface between the aqueous treatment chemical and contaminant because the sorbing contaminant is not as mobile compared to an aqueous contaminant. The strategy for remediating an adsorbing contaminant is to spread an injected treatment chemical radially away from an injection well in the center of the contaminant plume to chase the

slower-moving adsorbing contaminant with the faster-moving aqueous treatment chemical. As the treatment chemical plume overtakes the contaminant plume, the treatment chemical degrades the contaminant [113].

Piscopo et al. [137] expanded on the work of Neupauer and Mays [113] by applying the Borg MOEA [67] to explore the effects of heterogeneity and ambient groundwater flow on adsorbing contaminants governed by rate-limiting degradation reactions. Piscopo et al. [137] found 1) solutions with slower rate constants need higher amounts of treatment chemical injected to increase the treatment chemical concentration and therefore the rate constant for the contaminant degradation reaction, 2) contaminants with slower sorption rate constants are spread farther from the treatment chemical injection well and therefore need higher pumping rates over longer periods of time for the treatment chemical plume to overtake the contaminant plume, 3) contaminants in increasingly heterogeneous aquifers increased treatment chemical injection rates and mass to catch the leading edge of the contaminant plume, which can flow through preferential flow paths of high hydraulic conductivity more quickly spreading the leading edge of the plume further from the origin.

Investigations done by Neupauer and Mays [113] and Piscopo et al. [137] were conducted for contaminants whose degradation was rate limited and transport was subject to retardation due to sorption to aquifer media. These contaminants were modeled as one-way reactions meaning once the contaminant is degraded, it stays degraded. All of the previous investigations were conducted using contaminant degradation governed by a single reaction. Many contaminants like hexavalent uranium, U(VI), are subject to biogeochemically complex remediation pathways. The novel portion of this work is investigating the ability of EIE to promote increased immobilization of hexavalent uranium, U(VI), employing a flow and reactive-transport model based on geochemical conditions at two uranium contaminated sites.

1.3.4 Uranium removal from contaminated groundwater

Uranium contaminated groundwater can be treated via pump and treat methods; however, extensive lab and field research has been done evaluating *in situ* methods for uranium contaminated

groundwater. The DOE designated three legacy sites for field research involving legacy radioactive was in subsurface environments. The Old Rifle site is the only one of three DOE research sites located in the Colorado Plateau and therefore the only one relevant to this investigation. This site has been used for a number of investigations to gain insight into biogeochemical processes of uranium in the natural environment.

Bioremediation was primarily investigated through lab, field and modeling studies for *in situ* immobilization of U(VI) present on the site [178, 173, 9, 181, 182, 180, 55]. In uranium bioremediation, the removal pathway is just as important as the pathway through which uranium can re-mobilize following active remediation. The primary removal path for bioremediation is the addition of an electron donating compound to stimulate the growth and metabolic activity of native microbes as initially proposed in Lovley et al. [101]. Field and laboratory based research shows that stimulation promotes an array of oxidation reduction reactions with uranium and other geochemically relevant compounds that have interactions with both valence states of uranium.

Abdelouas et al. [1] investigated bioreduction of uranium contaminated groundwater at the UMTRA Project site outside of Tuba City, AZ using an ethanol amendment. They found presence of denitrifying sulfate- and iron-reducing bacteria throughout the study – denitrification, reduction, of ambient nitrite was complete within one week of the introduction of the ethanol amendment, U(VI) reduction to U(IV) took place over three weeks and was accompanied by sulfate reduction; the reduced form of uranium, precipitated as uraninite solid decreasing U(VI) solution concentrations to below 1 μg/L [1].

Similar investigations done on the Old Rifle IFRC site highlight similar mechanisms of legacy U(VI) in groundwater solution using an acetate amendment [9, 36, 173]. Many studies [100, 1, 57, 72, 9, 168] document that stimulating U(VI) contaminated aquifers with acetate can concomitantly reduce U(VI) along with the reduction of Fe(III) minerals present in aquifer systems via dissimilatory metal-reducing bacteria, *Geobacter*. Sulfate reduction is also present at significant quantities, evidenced by the decrease in sulfate concentrations with relatively equal and opposite formation of sulfide, which has been shown to inhibit reduction of U(VI) compared to reduction

promoted by metal-reducing bacteria [102, 127, 9].

In addition to the competition of U(VI) and Fe(III) for metabolism by metal-reducing bacteria, U(VI) aqueous speciation affects the distribution of U(VI) in the aqueous and sorbed phases, which has been shown by Pabalan et al. [130] and Moyes et al. [112]. In subsurface solutions at circumneutral pH found at the Old Rifle IFRC site, increased bicarbonate levels promote the desorption of uranium from aquifer media, [111, 49]; $Ca-U(VI)-CO_3$ complexes and pH have also been shown to compete with sorption sites for U(VI) species [186, 62, 110].

Work following field investigations conducted in 2002, 2003 and 2007 involved creating geochemical models describing the processes occurring based on acetate amendments at the Old Rifle IFRC site. Yabusaki et al. [181] was the first to create a one-dimensional reactive transport model based on field observations to model microbial reduction of Fe(III), U(VI), and S(VI). $CaUO_2(CO_3)_3^{2-}$ and $Ca_2UO_2(CO_3)_{3(aq)}$ are neglected in the bioavailable U(VI) pool because Brooks et al. [28] reports U(VI) in those complexes is thermodynamically unavailable for microbial processes. A 2007 field investigation discovered that phyllosilicate ferrous iron, $Fe(III)_{(ls)}$ and ferrous oxides provide the pool of bioavailable Fe(III) for metal-reducing bacteria to use as terminal electron acceptors in their metabolism. The majority of the bioavailable Fe(III) reduced during biostimualtion was phyllosilicate iron; however, only a small fraction (10%) of the Fe(II) created through reduction was observed in the aqueous phase [89, 78, 88, 87]. As a result, Fang et al. [54] expanded the modeling work done in Yabusaki et al. [181] to model data from 2007 experiments and geochemical dynamics created from the newly discovered pool of bioavailable Fe(III) present in Fe-bearing layer-silicate materials, mineral interactions of calcite ($CaCO_3$), siderite ($FeCO_3$), mackinawite (FeS), goethite (FeOOH) and elemental sulfur (S^0) and adsorption of Fe(II) and U(VI) species to aquifer media [54].

In field and lab studies, Bargar et al. [14] found the presence of two distinct pools of U(IV) present in aquifer sediments following the biostimulation of groundwater at the Old Rifle IFRC site, which is evidence for multiple reduction pathways. Crystalline uraninite ($UO_{2(s)}$) is the bioreduction product commonly found in lab studies, however the majority of U(IV) was found in non-crystalline

U(IV) species indicating presence of other pathways for bioreduced U(IV) to take following microbial metabolism [14].

U(IV) forms strong complexes with PO_4 species, which can only be associated with microbial biomass because ambient concentrations of phosphate at the Old Rifle IFRC site are fairly low. Although correlation of non-crystalline U(IV) is spatially associated with FeS, which can act as an oxidant for ambient oxidizing agents that would otherwise reoxidize U(IV) back to its mobile form [3, 23]. Although FeS could theoretically protect U(IV) from re-oxidation, it is less stable than crystalline uraninite [14].

1.4 Goals and Organization

The goal of this investigation is to evaluate the ability of EIE to promote increased levels of uranium immobilization compared to a three-well injection gallery remediation system. This investigation is based on the ability to model all of the biogeochemical processes occurring in the subsurface aqueous environment that affect the fate and transport of uranium. This investigation was conducted by updating a reactive-transport model developed to track fate and transport of uranium on the Naturita UMTRA Project site outside of Naturita, Colorado. No previous bioremediation field or lab work has been conducted based on biogeochemical conditions at the Naturita site. The nearest site where bioremediation field-work and biogeochemical reaction characterization occurred was at the Old Rifle IFRC site. The only available reaction framework developed to model bioremediation field studies at the Old Rifle IFRC site was developed for 1D transport and batch simulations. The second goal of this investigation is to apply the reaction framework developed for the Old Rifle IFRC site to the field-scale model at the Naturita site.

A description of the Naturita UMTRA Project site follows this chapter in Chapter 2. The milling and remediation history of the Naturita site is presented in Chapter 2 along with the simulated location of the uranium-contaminated groundwater plume at the site. Methods for conducting batch, 1D transport and field scale simulations of the uranium bioremediation reaction framework are presented in Chapter 3. Two field-scale systems are simulated using the Naturita

site model: a three-well injection gallery system designed based on previous bioremediation field investigations conducted at the Old Rifle site and an EIE system. Results from these investigations are presented in Chapter 4. Conclusions and suggestions for future work are presented in Chapter 5 and a non-technical summary is included in Appendix A.

Chapter 2

Site Description

The Naturita Uranium Mill Tailings Remedial Action (UMTRA) Project site is located in southwestern Colorado in the west end of Montrose County approximately 2 miles north of Naturita, CO. Uranium and vanadium ore processing activity occurred on site from the 1930s into the late 1960s. The 79-acre site contains the former mill site in the San Miguel floodplain between Colorado Highway 141 and the San Miguel River and the former ore storage site across Colorado Highway 141 as shown in Figure 2.1.

As a result of windblown tailings and transport of groundwater containing uranium and vanadium originating from the regulatory site, institutional controls have been enacted in areas adjacent to the site Figure 2.1. The Maupin property surrounding the regulatory site to the north and east is now largely under institutional controls. Rockwood Lithium GmbH owns the majority of the former mill and ore storage site except for an area owned by the City of Naturita in the central portion of the former mill site.

2.1 Site History

2.1.1 Processing History

The first ore processing activity occurred on the site around 1930 when Rare Metals Company built a mill financed by the Vanadium Corporation of America (VCA). When Rare Metals folded in mid-1930s, VCA obtained the property, performed improvements, and reopened the property in 1939 for vanadium processing. Additional process improvements occurred in 1942 to recover

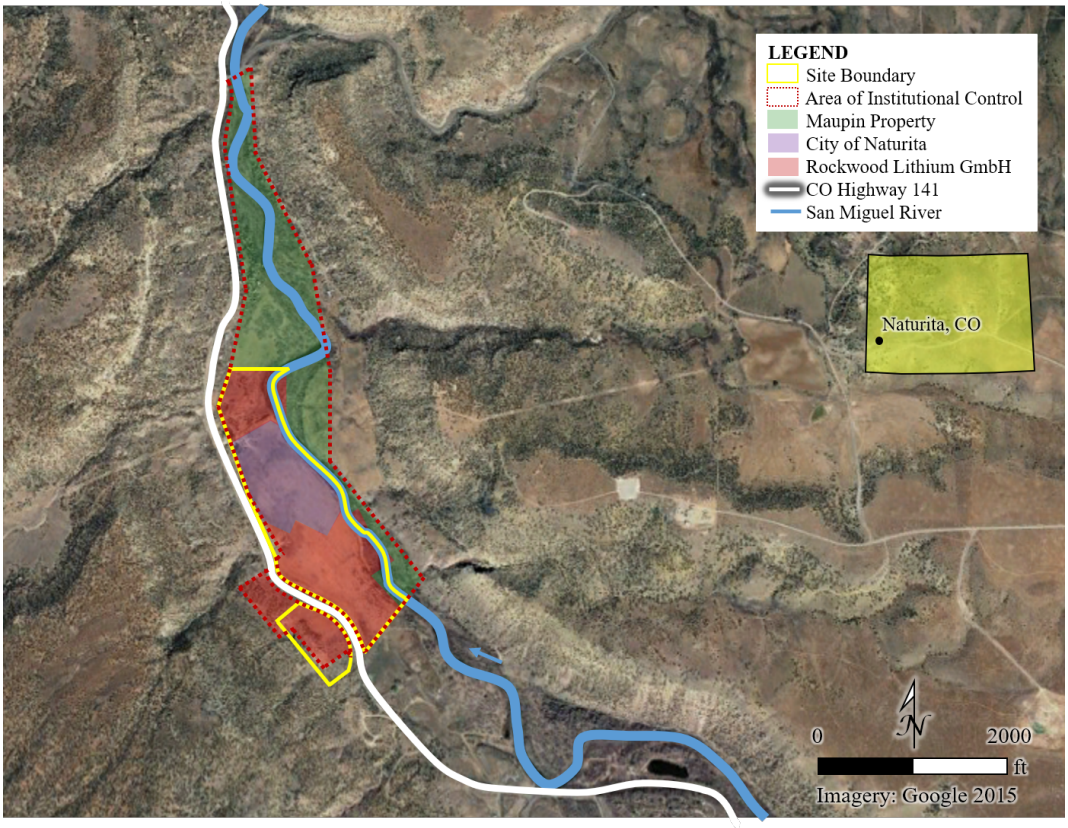

Figure 2.1: Aerial view of the extent of the regulatory area and area of institutional controls at the Naturita site. The path of the San Miguel River and Colorado Highway 141 are shown in blue and white respectively. Property ownership is also delineated through the opaque shaded areas.

uranium for use in the Manhattan Engineering District Project [119, 155].

Ore was salt-roasted and quenched in a carbonate solution and then was carbonate-leached. Solution was treated with excess sodium bicarbonate to form uranium- and vanadium-containing carbonate leach liquor. The liquor was treated with sulfuric acid and boiled to expel carbon dioxide. Metal-containing filtrate was treated with a reducing mixture of salt, soda ash and either sawdust or fuel oil. Ash containing the products was then water-leached dissolving vanadium leaving uranium. The solution following water leaching was then further processed to extract vanadium. The mill had an original capacity of 150 tons per day, but was upgraded in 1954 to process 350 tons of ore per day [119]. Approximately 704,000 tons of ore were processed by the facility before its contract with the DOE (US Atomic Energy Commission, at the time) expired in 1958 [60]. VCA continued

to operate an upgrader plant from 1961 – 1963 at the site, producing concentrates exported from the site for additional processing. Until 1978, VCA used the site as a headquarters for downsizing their greater company activities, while also bringing processing and mining equipment from all areas of the Colorado Plateau to the site to sell to other mining interests [118].

When uranium became commercially available in the 1970s, the Nuclear Division of General Electric leased part of the property as a procurement station for uranium ore extracted from the greater Uravan mineral belt until the 1980s. The Uravan mineral belt is an area extending between northwest New Mexico through southwest Colorado and northeast Arizona into southeast Utah containing large, high-grade uranium ores. In 1976, the Ranchers Exploration and Development Corporation bought part of the site with approximately 360 thousand tons of tailings for further processing. Ranchers extracted an additional 380 thousand pounds of uranium and 1.84 million pounds of vanadium from tailings removed from the site [170].

2.1.2 Remedial Action History

Following the passing of the Uranium Mill Tailings Radiation Control Act (UMTRCA) in 1978, widespread remedial action was conducted through the US DOE's UMTRA Project. During this project, 771,400 cubic yards of residual radioactive material (RRM) was removed from the site between January 1993 and September 1998. RRM mostly consisted of earthen material, but also contained razed infrastructure present at the site. RRM was largely from the former mill yard, tailings area, and windblown areas surrounding the site. Small amounts of RRM were removed from the former ore storage site and stockpiled demolition debris. All RRM was trucked to the Upper Burbank Engineered Disposal Cell located 15 miles northwest of the site near the former town site of Uravan, CO. At the end of the process, the site was graded and reseeded [120].

Naturita is unique among other UMTRA Project sites because a large amount of radioactive materials were left in place, both on and off site, during surface remediation. 11 acres on the site and 11 acres on the Maupin property still house radioactive material from historical processing activity.

Following soil remediation, the DOE conducted investigations to determine if groundwater remedial action was needed. Uranium and vanadium are the only contaminants present at the site that could pose a risk to human health, but it was determined that exposure risks resulting from these metals at the site would result only in occupational and residential scenarios. Supplemental standards have been granted and institutional controls forbidding the use of this water have been implemented. As part of these controls, surface and groundwater monitoring is in place to ensure institutional controls are followed and uranium and vanadium concentrations decrease into the future.

2.2 Site Conceptual Model

2.2.1 Geology

The site is located near the eastern edge of canyon lands country in the northeastern part of Colorado Plateau Physiographic Province. Geologic stratigraphy underlying the site consists of three main members. A shallow alluvium is the uppermost layer underlain by bedrock consisting of two members of the Morrison formation. The alluvium is thickest in the direct vicinity to the river and becomes only a few feet thick near CO Highway 141. Directly under the alluvium is the approximately 100-foot thick Brushy Basin Member characterized as a fine-grained shale deposit. The Salt Wash Member of sandstone underlies the Brushy Basin Member [119].

2.2.2 Surface and Groundwater Hydrology

A shallow alluvial aquifer exists in the shallow alluvium. The near-surface shallow alluvial aquifer is separated from the Salt Wash aquifer by fine-grained shale of the Brushy Basin Member. Hydraulic head reported from a well drilled into the Salt Wash aquifer are greater than those present in the alluvial aquifer, showing a potential for upward flow and transport; however, chlorine concentrations in Salt Wash aquifer are 200 times higher than in the shallow alluvial aquifer indicating minimal upward flow [47].

The alluvial aquifer is recharged by precipitation and interactions with the San Miguel River (see Figure 2.1. The region is semiarid with high temperature variations and evaporation, and low humidity and precipitation [119]. Precipitation occurs as short-duration, high intensity, late afternoon thunderstorms conducive to runoff and as snow. Annual precipitation is approximately nine inches. The San Miguel River is the only perennial water body present at the site and acts as both a source and sink of water. Maximum stream flow in the San Miguel River occurs in the early summer months resulting from snowmelt or summer thunderstorms. A USGS stream gauge station upstream in Naturita, shows average maximum flow of 2000 cubic feet per second (cfs) and average minimum flows of 60 cfs [118]. Groundwater in the shallow alluvial aquifer is recharged by the river southeast of the former mill site, then flows north parallel to the river through the former mill site onto the Maupin property. Groundwater flow paths turn to the northeast and then drain back into the river [47].

2.2.3 Contamination

Uranium and vanadium ore from nearby mines was transported to the site and processed at the mill. The site housed processing activity for more than thirty years during which more than 704,000 tons of ore was processed. Ores were mainly processed for uranium and vanadium but also contained elevated levels of arsenic, molybdenum, selenium and sulfate [119]. Sulfuric acid, bases and other chemicals were used in the metal extraction process. According to the US DOE [119], no data are available on the amounts of water used in the process nor the subsequent wastewater generated, but the US DOE approximates that several million gallons of contaminated water seeped into the alluvial aquifer. Elevated levels of alkalinity, sulfate, sodium, and chloride near the former mill site may be due to leaching of water or chemicals into the alluvial aquifer.

Uranium and vanadium are the primary contaminants in the shallow alluvial aquifer. These metals were introduced into the subsurface primarily through leaching of residual metals left in processed tailings by precipitation. Leaching of residual metals in tailings occurred most significantly between the late 1930s until the completion of surface remediation in late 1998. Legacy material

left on the site due to human health risks associated with its removal probably still supply uranium and vanadium to the shallow alluvial aquifer.

Uranium is of greater concern than vanadium at this site because of its radioactive properties and greater mobility in aqueous environments compared to vanadium. Reactive transport models calibrated to well samples show the plume of uranium-contaminated groundwater originating under the former mill site has spread north and east into the San Miguel and the adjacent Maupin property as shown in Figure 2.2. Contaminated water flowing into the San Miguel River has been shown to not affect water quality [47]. Samples indicate uranium is still present in the alluvial aquifer in concentrations greater than established maximum contaminant limit (MCL) established for the UMTRA Project. [119].

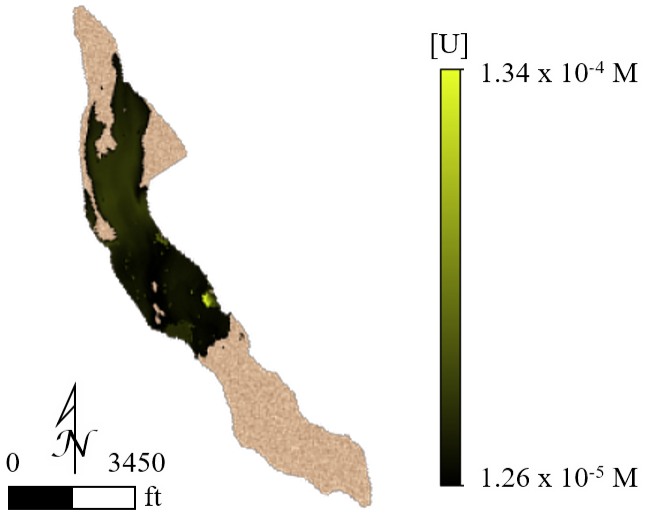

Figure 2.2: The spatial extent and concentration of aqueous uranium in the groundwater of the shallow alluvial aquifer underlying the Naturita site as simulated by the model from Curtis et al. [45].

Chapter 3

Methods

The remediation pathway employed for removing uranium from groundwater is stimulating native dissimilatory metal-reducing bacteria via an acetate amended treatment solution. Microbes use electrons donated from introduced acetate in their metabolism and use uranium, along with sulfate and ferric iron, as terminal electron acceptors. When electrons are transferred to U(VI) species present in the subsurface, U(VI) is reduced to U(IV) and subsequently forms solid-phase species removing uranium from contaminated groundwater present at the Naturita site. The fate of reduced uranium species forming from the U^{+4} ion is a subject of ongoing research. Dissolved organic carbon has the potential to inhibit the formation of solid-phase uranium species. Dissolved organic carbon is present in groundwater at the Naturita site in concentrations on the order of mg/L [119], which may affect the precipitation of solids forming from the U^{+4} ion produced by microbial metabolism. However, since no reaction frameworks exist to model the formation of species other than uraninite resulting from microbial metabolism and the fact that work on which the reaction framework is largely based ignored non-uraninite U^{+4} species, this work assumes all reduced uranium precipitates as crystalline uraninite, $UO_{2(s)}$.

To promote widespread removal of uranium from contaminated groundwater, it is critical to deliver the acetate amended treatment solution throughout the plume of uranium-contaminated groundwater. Engineered Injection and Extraction (EIE) is scored against a three-well injection gallery for its ability to promote *in situ* removal of U(VI) to solid-phase U(IV). To score these two systems, a flow and reactive transport model was developed for the Naturita site. Curtis

et al. [45] developed a flow and reactive transport model to the track fate of uranium present in the shallow alluvial aquifer underlying the Naturita site. This model encompasses the half-century period during which uranium from tailings and wastewater ponds was introduced into the underlying aquifer and the half-decade time period during which removal of residual radioactive material (RRM) was conducted on the site. Other known chemicals used in the milling process were also introduced to the underlying aquifer at elevated concentrations, like bicarbonate used in the leaching process and NaOH used in the salt-roasting process. Calibration of the model conducted in Curtis et al. [45] was based on head and concentration data from wells present at the Naturita site. Yabusaki et al. [180] developed a kinetic reaction framework based on field experiments conducted at the Old Rifle IFRC site outside of Rifle, CO. Although the reaction framework developed in Yabusaki et al. [180] was based on the Old Rifle IFRC site, employing these pathways can be implemented into the Naturita site model to create a semi-synthetic model for use in evaluating EIE as a remediation technique for uranium-contaminated groundwater.

To accurately investigate these processes at a field scale, benchmarking exercises were conducted to characterize dynamics between biological processes competing for acetate, mineral interactions, and adsorption and then implemented into the field scale model as shown in Figure 3.1. Batch and one-dimensional transport results using physical and chemical conditions present in the model from Curtis et al. [45] were conducted and compared to those presented in Yabusaki et al. [180] to confirm reaction pathways are correctly represented before employment at the field scale. This chapter presents a conceptual model, mathematical model and numerical formulation for the benchmark, 1D transport, and field scale model.

3.1 Benchmark Simulation

3.1.1 Conceptual Model

Native dissimilatory metal-reducing bacteria exist in the subsurface and can be stimulated via acetate. Following the injection of this electron donating compound, Fe^{+2}, $SO_4{}^{-2}$, and $UO_2{}^{+2}$

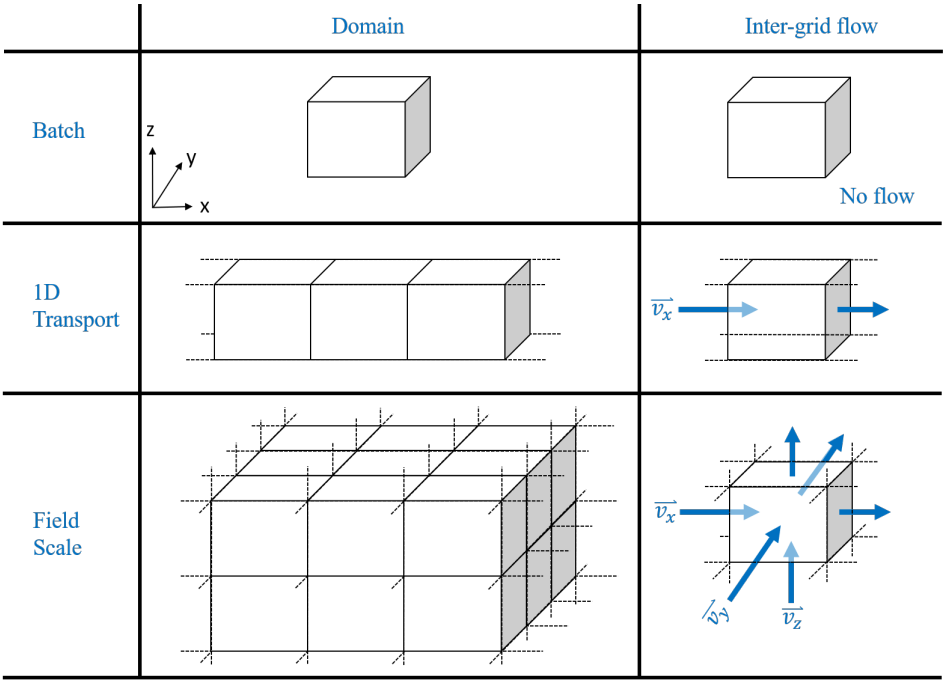

Figure 3.1: Discretization of each of the scales investigated in this study from batch-scale, occurring in the equivalent of one grid block to field-scale occurring in a three-dimensional grid. The batch-scale simulations are conducted to investigate how reaction dynamics evolve with time absent of flow. A one-dimensional column simulation was conducted to monitor how reaction kinetics evolve in a simple, homogeneous flow scenario. The field-scale simulation is conducted to track the ability of different remediation systems to influence flow to enhance uranium immobilization.

"compete" for use as a terminal electron acceptor in bacterial metabolism. To accurately model this process, all relevant geochemical processes need to be modeled including aqueous species: Ca^{+2}, CH_3COO^-, $CO_3{}^{-2}$, Cl^-, K^+, Na^+, $NH_4{}^+$, Mg^{+2}, and HS^-; minerals: calcite ($CaCO_{3(s)}$), siderite ($FeCO_{3(s)}$), mackinawite ($FeS_{(s)}$), elemental sulfur ($S_{(s)}{}^0$), goethite ($FeOOH_{(s)}$) ferrous and ferric phyllosilicates ($Fe(II)_{(ls)}$, $Fe(III)_{(ls)}$) and uraninite ($UO_{2(s)}$); and surface species. To investigate the dynamics of these processes, a batch simulation and 1D transport simulation were conducted. The batch simulation involves the addition of the treatment solution to the groundwater within the plume of uranium-contaminated groundwater. The 1D transport simulation involves a sustained release of treatment solution at the upstream boundary followed by areal groundwater entering the upstream boundary representing the period following the treatment solution injection.

3.1.2 Mathematical Model

3.1.2.1 Reactive Transport

Batch and 1D transport simulations were conducted using PHREEQC – a computer program for speciation, batch-reaction, one-dimensional transport, and inverse geochemical calculations [133]. PHREEQC calculates equilibrium between aqueous, exchange, surface species and pure solid and gas phases through a modified Newton-Raphson method [133]. The distribution of aqueous, mineral, and surface species existing at equilibrium under a given set of conditions are found through solutions to a set of nonlinear equations describing aqueous charge balance, mass balance encompassing all phases, alkalinity, activity of water and ionic strength. For kinetically controlled reactions generating a solid or non-equilibrium solution species, changes in aqueous species mass, m_i, is governed by the rate equation

$$\frac{dm_i}{dt} = c_{i,k} R_k \tag{3.1}$$

where $c_{i,k}$ is the stoichiometric coefficient of species i in the in the kinetic reaction and and R_k is the overall rate for substance k in moles per kilogram of water per second [133]. 1D transport is

governed by the 1D advection-dispersion-reaction equation given as

$$\frac{\partial C_i}{\partial t} = -v\frac{\partial C_i}{\partial x} + D_L\frac{\partial^2 C_i}{\partial x^2} - \frac{\partial q_i}{\partial t} + R_{r,i} \tag{3.2}$$

where C_i is the aqueous concentration of species i, t is time, v is pore water flow velocity, and x is distance, q_i is the concentration of i in the solid phase and D_L is the hydrodynamic dispersion coefficient,

$$D_L = D_e + \alpha_L|v|$$

where D_e is the effective diffusion coefficient, α_L is the dispersivity and $R_{r,i}$ is the mass action term governing the accumulation or loss species i through equilibrium (mass balance) or kinetic reaction (Equation 3.1) [133].

3.1.2.2 Equilibrium Reactions

The reaction framework consists of aqueous, surface, ion exchange and mineral species governed by equilibrium and kinetic reactions. Formation equations for all species included in this work are listed in Tables 3.1 and 3.2.

In natural aqueous systems, mineral constituents can precipitate to form solid-phase minerals under geochemical conditions present in this study. In this aquifer system, calcite is in equilibrium with groundwater at the Naturita site. The solubility product K_{sp} for biogenic uraninite found in Spycher et al. [162] is employed in this study to describe the formation of $UO_{2(s)}$. Only the formation of $UO_{2(s)}$ was investigated in this study. Both mineral equilibrium association reactions and solubility products are shown in Table 3.3.

Ion exchange occurs in solutions due to a charge developing on surfaces of aquifer media. These charges result in ions of opposite charge becoming associated with aquifer media in significant quantities. Including ion exchange in the reactive transport simulation can aid in modeling heterogeneity present at the site as is the case at Naturita [43]. Ion exchange species and their aqueous/solid-phase distribution coefficient, K_d are shown in Table 3.4.

Table 3.1: Relevant non-uranium solutions species, their formation equations and equilibrium constants at $T = 298$ K as in Lu et al. [103] unless otherwise noted.

Equation	Log(K)
$H_2O \rightleftharpoons OH^- H^+$	-14.0
$2H_2O \rightleftharpoons O_2 + 4H^+ + 4e^-$	-86.08
$2H^+ + 2e^- \rightleftharpoons H_2$	-3.15
${CO_3}^{-2} + H^+ \rightleftharpoons {HCO_3}^-$	10.329
${CO_3}^{-2} + 2H^+ \rightleftharpoons CO_2 + H_2O$	16.681
${CO_3}^{-2} + 10H^+ + 8e^- \rightleftharpoons CH_4 + 3H_2O$	41.071
${SO_4}^{-2} + H^+ \rightleftharpoons {HSO_4}^-$	1.988
$HS^- \rightleftharpoons S^{2-} + H^+$	-12.918
${SO_4}^{-2} + 9H^+ + 8e^- \rightleftharpoons HS^- + 4H_2O$	33.65
$HS^- + H^+ \rightleftharpoons H_2S$	6.994
$CH_3COO^- + H^+ \rightleftharpoons CH_3COOH$	5.00
${}^a{Ca}^{+2} + CH_3COO^- \rightleftharpoons Ca(CH_3COO)^+$	1.18^a
${}^a{Fe}^{+2} + CH_3COO^- \rightleftharpoons Fe(CH_3COO)^+$	1.82^a
${}^a{Mg}^{+2} + CH_3COO^- \rightleftharpoons Mg(CH_3COO)^+$	1.14^a
${}^a{Na}^+ + CH_3COO^- \rightleftharpoons Na(CH_3COO)$	-0.18^a
${NH_4}^+ \rightleftharpoons NH_3 + H^+$	-9.252
${NH_4}^+ + {SO_4}^{-2} \rightleftharpoons {NH_4HSO_4}^-$	1.11
${Ca}^{+2} + H_2O \rightleftharpoons CaOH^+ + H^+$	-12.78
${Ca}^{+2} + {CO_3}^{-2} \rightleftharpoons CaCO_3$	3.224
${Ca}^{+2} + {CO_3}^{-2} + H^+ \rightleftharpoons {CaHCO_3}^+$	11.435
${Ca}^{+2} + {SO_4}^{-2} \rightleftharpoons CaSO_4$	2.3
${Ca}^{+2} + {HSO_4}^- \rightleftharpoons {CaHSO_4}^+$	1.08
${Mg}^{+2} + H_2O \rightleftharpoons MgOH^+ + H^+$	-11.44
${Mg}^{+2} + {CO_3}^{-2} \rightleftharpoons MgCO_3$	2.98
${Mg}^{+2} + H^+ + {CO_3}^{-2} \rightleftharpoons {MgHCO_3}^+$	11.399
${Mg}^{+2} + {SO_4}^{-2} \rightleftharpoons MgSO_4$	2.37
${Na}^+ + H_2O \rightleftharpoons NaOH + H^+$	-14.18
${Na}^+ + {CO_3}^{-2} \rightleftharpoons {NaCO_3}^-$	1.27
${Na}^+ + {HCO_3}^- \rightleftharpoons NaHCO_3$	-0.25
${Na}^+ + {SO_4}^{-2} \rightleftharpoons {NaSO_4}^-$	0.7
${K}^+ + H_2O \rightleftharpoons KOH + H^+$	-14.46
${K}^+ + {SO_4}^{-2} \rightleftharpoons {KSO_4}^-$	0.85
${Fe}^{+2} + H_2O \rightleftharpoons FeOH^+ + H^+$	-9.5
${Fe}^{+2} + Cl^- \rightleftharpoons FeCl^+$	0.14
${Fe}^{+2} + {CO_3}^{-2} \rightleftharpoons FeCO_3$	4.38
${Fe}^{+2} + {HCO_3}^- \rightleftharpoons {FeHCO_3}^+$	2.0
${Fe}^{+2} + {SO_4}^{-2} \rightleftharpoons FeSO_4$	2.25
${Fe}^{+2} + {HSO_4}^- \rightleftharpoons {FeHSO_4}^+$	1.08
${Fe}^{+2} + 2\,HS^- \rightleftharpoons Fe(HS)_2$	8.95
${Fe}^{+2} + 3\,HS^- \rightleftharpoons {Fe(HS)_3}^-$	10.987

[a] Yabusaki et al. [180].

Table 3.2: Uranium solutions species, their formation equations and equilibrium constants at $T = 298$ K as in Lu et al. [103] unless otherwise noted.

Equation	Log(K)
$UO_2^{2+} + H_2O \rightleftharpoons UO_2OH^+ + H^+$	-5.25
$UO_2^{2+} + 2\,H_2O \rightleftharpoons UO_2(OH)_2 + 2\,H^+$	-12.15
$UO_2^{2+} + 3\,H_2O \rightleftharpoons UO_2(OH)_3^- + 3\,H^+$	-20.25
$UO_2^{2+} + 4\,H_2O \rightleftharpoons UO_2(OH)_4^{2-} + 4\,H^+$	-32.4
$2\,UO_2^{2+} + H_2O \rightleftharpoons (UO_2)_2OH^{3+} + H^+$	-2.7
$2\,UO_2^{2+} + 2\,H_2O \rightleftharpoons (UO_2)_2(OH)_2^{2+} + 2\,H^+$	-5.62
$3\,UO_2^{2+} + 4\,H_2O \rightleftharpoons (UO_2)_3(OH)_4^{2+} + 4\,H^+$	-11.9
$3\,UO_2^{2+} + 5\,H_2O \rightleftharpoons (UO_2)_3(OH)_5^+ + 5\,H^+$	-15.55
$3\,UO_2^{2+} + 7\,H_2O \rightleftharpoons (UO_2)_3(OH)_7^- + 7\,H^+$	-32.2
$4\,UO_2^{2+} + 7\,H_2O \rightleftharpoons (UO_2)_4(OH)_7^+ + 7\,H^+$	-21.9
$UO_2^{2+} + CO_3^{2-} \rightleftharpoons UO_2CO_3$	9.94
$UO_2^{2+} + 2\,CO_3^{2-} \rightleftharpoons UO_2(CO_3)_2^{2-}$	16.61
$UO_2^{2+} + 3\,CO_3^{2-} \rightleftharpoons UO_2(CO_3)_3^{4-}$	21.84
$3\,UO_2^{2+} + 6\,CO_3^{2-} \rightleftharpoons (UO_2)_3(CO_3)_6^{6-}$	54.0
$2\,UO_2^{2+} + CO_3^{2-} + 3\,H_2O \rightleftharpoons (UO_2)_2CO_3(OH)_3^- + 3\,H^+$	-0.855
$3\,UO_2^{2+} + CO_3^{2-} + 3\,H_2O \rightleftharpoons (UO_2)_3(CO_3)(OH)_3^+ + 3\,H^+$	0.66
$UO_2^{2+} + NO_3^- \rightleftharpoons UO_2NO_3^+$	0.3
$UO_2^{2+} + Cl^- \rightleftharpoons UO_2Cl^+$	0.17
$UO_2^{2+} + 2\,Cl^- \rightleftharpoons UO_2Cl_2$	-1.1
$UO_2^{2+} + SO_4^{2-} \rightleftharpoons UO_2SO_4$	3.15
$UO_2^{2+} + 2\,SO_4^{2-} \rightleftharpoons UO_2(SO_4)_2^{2-}$	4.14
$^aUO_2^{2+} + CH_3COO^- \rightleftharpoons UO_2CH_3COO^+$	3.04
$^aUO_2^{2+} + 2\,CH_3COO^- \rightleftharpoons UO_2(CH_3COO)_2$	5.54
$^aUO_2^{2+} + 3\,CH_3COO^- \rightleftharpoons UO_2(CH_3COO)_3^-$	6.94
$Ca^{2+} + UO_2^{2+} + 3\,CO_3^{2-} \rightleftharpoons CaUO_2(CO_3)_3^{2-}$	27.18
$2\,Ca^{2+} + UO_2^{2+} + 3\,CO_3^{2-} \rightleftharpoons Ca_2UO_2(CO_3)_3$	30.7
$Mg^{2+} + UO_2^{2+} + 3\,CO_3^{2-} \rightleftharpoons MgUO_2(CO_3)_3^{2-}$	26.11

[a] Yabusaki et al. [180].

Table 3.3: Formation equilibrium equations for relevant minerals in equilibrium with groundwater at the Naturita site.

Equation	Log(K_{sp})
$Ca^{+2} + CO_3^{-2} \rightleftharpoons CaCO_{3(s)}$	8.48
$U^{+4} + 2\,H_2O \longrightarrow UO_{2(s)} + 4\,H^+$	-1.42[c]

[a] Biogenic uraninite K_{sp} from Spycher et al. [162].

Table 3.4: Formation equations for ion exchange species and aqueous/solid-phase distribution coefficients.

Equation	$\text{Log}(K_d)$
$\text{Na}^{+} + {}^{a}\text{X}^{-} \rightleftharpoons \text{NaX}$	0.0
$\text{K}^{+} + \text{X}^{-} \rightleftharpoons \text{KX}$	0.7
$\text{Ca}^{+2} + 2\,\text{X}^{-} \rightleftharpoons \text{CaX}_2$	0.8
$\text{Mg}^{+2} + 2\,\text{X}^{-} \rightleftharpoons \text{MgX}_2$	0.5

[a] Ion exchange species representing negatively charged aquifer media.

Surface complexation is similar to ion exchange in that both involve the association of aqueous ions to aquifer media. However, surface complexation differs from ion exchange in the mechanism by which aqueous ions associate with charged surfaces present on aquifer media. In contrast to ion exchange, surface complexation involves chemical bond formation with species creating non-zero charge on the aquifer media surface. The composition and thermodynamics of these complexes is highly uncertain as these processes occur at ionic scales, so these interactions can be modeled empirically by surface complexation models. Surface complexation models consist of generic adsorption sites with different affinities to adsorb aqueous ions present in the surrounding groundwater. Thermodynamic-esque relationships are developed based on calibration to laboratory data collected to describe these processes. Much of the previous work based on the Naturita site has been focused on developing surface complexation models to effectively track changes to the distribution coefficient, K_d, under different geochemical conditions [47, 45]. As part of the creation of the model in Curtis et al. [45], a surface complexation model was developed to model uranium adsorption based on Naturita aquifer sediment characterizations and calibration with uranium adsorption laboratory experiments as shown in Table 3.5 for use in benchmark experiments.

For the batch and 1D transport simulations, uranium adsorption is modeled by a surface complexation model Lu et al. [103]. The surface complexation model has three surfaces – R, S, and T – for each facies employed in the field-scale model to model aquifer field-scale heterogeneity. Field-scale heterogeneity is formally presented in Section 3.1.3 and was simplified for the purpose

Table 3.5: Formation equilibrium equations for uranium surface species used in the column simulation based on the field-scale surface complexation model from Lu et al. [103].

Equation	$\mathrm{Log}(K_d)$	Concentration[a]
$\mathrm{Rw\_OH} + {\mathrm{UO_2}}^{+2} \rightleftharpoons \mathrm{Rw\_OUO_2}^{+} + \mathrm{H}^{+}$	2.8	2.24×10^{-3}
$\mathrm{Rs\_OH} + {\mathrm{UO_2}}^{+2} + {\mathrm{CO_3}}^{-2} \rightleftharpoons \mathrm{Rs\_OUO_2CO_3}^{-} + \mathrm{H}^{+}$	10.0	4.59×10^{-5}
$\mathrm{Sw\_OH} + {\mathrm{UO_2}}^{+2} \rightleftharpoons \mathrm{Sw\_OUO_2}^{+} + \mathrm{H}^{+}$	2.7	6.42×10^{-3}
$\mathrm{Ss\_OH} + {\mathrm{UO_2}}^{+2} + {\mathrm{CO_3}}^{-2} \rightleftharpoons \mathrm{Ss\_OHUO_2(CO_3)_2}^{-2}$	22.0	1.98×10^{-4}
$\mathrm{Tw\_OH} + {\mathrm{UO_2}}^{+2} + {\mathrm{CO_3}}^{-2} \rightleftharpoons \mathrm{Tw\_OUO_2CO_3}^{-} + \mathrm{H}^{+}$	7.4	3.51×10^{-2}
$\mathrm{Ts\_OH} + {\mathrm{UO_2}}^{+2} + {\mathrm{CO_3}}^{-2} \rightleftharpoons \mathrm{Ts\_OUO_2CO_3}^{-} + \mathrm{H}^{+}$	9.2	1.20×10^{-3}
$\mathrm{Ts\_OH} + {\mathrm{UO_2}}^{+2} + 2\,{\mathrm{CO_3}}^{-2} \rightleftharpoons \mathrm{Ts\_OUO_2(CO_3)_2}^{-3} + \mathrm{H}^{+}$	15.4	
$\mathrm{Tv\_OH} + {\mathrm{UO_2}}^{+2} + 2\,{\mathrm{CO_3}}^{-2} \rightleftharpoons \mathrm{Tv\_OUO_2(CO_3)_2}^{-3} + \mathrm{H}^{+}$	16.4	5.85×10^{-5}

[a]Concentrations are given as moles per liter of bulk aquifer volume (L_b).

of the batch and 1D transport simulations by constructing a homogeneous porous medium and a surface complexation model indicative field-scale conditions. In this study, names of surface species are in the form

[Surface Name][Site Name]_[Adsorbed Species].

Surface and site names have no chemical meaning and are used only in the identification of the species. All three surfaces have two sites named for their affinity to adsorb uranium: "w" for weak and "s" for strong; the "T" surface has an additional very strong "v" adsorption site. Concentrations and equilibrium distribution coefficients for each of the sites and species in each surface is given in Table 3.5.

3.1.2.3 Kinetic Reactions

In addition to equilibrium reactions, the microbial and non-equilibrium minerals are modeled by kinetic reactions. There are four biologically mediated reactions, which model the competition between sulfate-reducing and iron-reducing bacteria for the injected electron donor to use in microbial metabolism. These reactions proceed forward only and are governed by the following reactions

and rate expressions

$$0.125\ \mathrm{CH_3COO^-} + 0.6\ \mathrm{FeOOH_{(s)}} + 1.155\ \mathrm{H^+} + 0.02\ \mathrm{NH_4{}^+} \xrightarrow{R_{Ac}^{bio}}$$
$$0.02\ \mathrm{FeRB} + 0.6\ \mathrm{Fe^{2+}} + 0.92\ \mathrm{H_2O} + 0.15\ \mathrm{HCO_3{}^-}$$

$$R_{Ac}^{bio} = -\mu_{\mathrm{FeRB,FeOOH_{(s)}}} S_{Ac}(C_{Ac})(C_{>\mathrm{FeOH}})$$

$$0.125\ \mathrm{CH_3COO^-} + \mathrm{Fe(III)_{(ls)}} + 0.5\ \mathrm{H_2O} \xrightarrow{R_{Ac}^{bio}}$$
$$0.25\ \mathrm{HCO_3{}^-} + 0.9\ \mathrm{Fe(II)_{(ls)}} + 0.1\ \mathrm{Fe^{2+}} + 1.125\ \mathrm{H^+}$$

$$R_{Ac}^{bio} = -\mu_{\mathrm{FeRB,Fe(III)_{ls}}} S_{Ac}(C_{Ac})(C_{\mathrm{Fe(III)_{ls}}})$$

$$0.125\ \mathrm{CH_3COO^-} + 0.0057\ \mathrm{H^+} + 0.0038\ \mathrm{NH_4{}^+} + 0.1155\ \mathrm{SO_4{}^{2-}} \xrightarrow{R_{Ac}^{bio}}$$
$$0.0038\ \mathrm{SRB} + 0.1155\ \mathrm{HS^-} + 0.0114\ \mathrm{H_2O} + 0.231\ \mathrm{HCO_3{}^-}$$

$$R_{Ac}^{bio} = -\mu_{SRB,\mathrm{SO_4{}^{-2}}} S_{Ac} B_{SRB} \left(\frac{C_{Ac}}{K_{s,Ac} + C_{Ac}} \right) \left(\frac{[\mathrm{SO_4{}^{-2}}]}{K_{s,\mathrm{SO_4{}^{-2}}} + [\mathrm{SO_4{}^{-2}}]} \right)$$

$$0.125\ \mathrm{CH_3COO^-} + 0.3538\ \mathrm{H_2O} + 0.0113\ \mathrm{NH_4{}^+} + 0.3875\ \mathrm{UO_2{}^{2+}} \xrightarrow{R_{Ac}^{bio}}$$
$$0.0113\ \mathrm{FeRB} + 0.855\ \mathrm{H^+} + 0.1938\ \mathrm{HCO_3{}^-} + 0.3875\ \mathrm{UO_{2(s)}}$$

$$R_{Ac}^{bio} = -\mu_{\mathrm{FeRB,UO_2{}^{+2}}} S_{Ac} \left(\frac{C_{Ac}}{K_{s,Ac} + C_{Ac}} \right) \left(\frac{[\mathrm{UO_2{}^{+2}_{avail.}}]}{K_{s,\mathrm{UO_2{}^{+2}}} + [\mathrm{UO_2{}^{+2}_{avail.}}]} \right)$$

where R_{Ac}^{bio} is the rate of acetate consumption in microbial metabolic processes, $\mathrm{Fe(III)_{(ls)}}$ and $\mathrm{Fe(II)_{(ls)}}$ are Fe(III) and Fe(II) bound in layer-silicate (phyllosilicate) materials, FeRB and SRB are iron and sulfate reducing bacteria, respectively, $\mu_{m,eA}$ is the intrinsic rate constant of microorganism m and the electron acceptor eA, S_{Ac} is the acetate stoichiometric coefficient, B_m is the biomass concentration for m, and $K_{s,eA}$ is the half-saturation constant for eA. $\mathrm{C_5H_7O_2N}$ is the molecular formula for FeRB and SRB. SRB biomass also exhibits first-order decay in time given as

$$\frac{dB_{SRB}}{dt} = -k_{decay,SRB} B_{SRB}$$

with first-order rate constant, $k_{decay,SRB}$. [${UO_2}^{+2}{}_{\text{avail.}}$] refers to the concentration of aqueous uranium species thermodynamically available for use in microbial metabolic processes. All uranyl-containing aqueous species except ${CaUO_2(CO_3)_3}^{-2}{}_{(aq)}$ and $Ca_2UO_2(CO_3)_{3(aq)}$ are available for reduction based on results from field and laboratory work at the Old Rifle site [180, 28] and therefore are excluded from the concentration of aqueous uranium for the calculation of the reaction rate.

While biological reactions are the mechanism to transforming U(VI) into solid-phase, $UO_{2(s)}$, several mineral reactions affect rates of U(VI) removal from contaminated groundwater and therefore need to modeled. Minerals governed by kinetic processes are siderite, $FeCO_{3(s)}$, mackinawite, $FeS_{(s)}$, and elemental sulfur, $S^0_{(s)}$ and are governed by reactions and rate expressions given as

$$Fe^{2+} + {HCO_3}^- \underset{r_{-i}}{\overset{r_i}{\rightleftharpoons}} FeCO_{3(s)} + H^+$$

$$r_{\pm i} = \begin{cases} k_i(\Omega_i - 1) & \text{for } \Omega_i \geq 1 \\ k_{-i}[Q_i](\Omega_i - 1) & \text{for } \Omega_i < 1 \end{cases}$$

$$Fe^{2+} + HS^- \underset{r_{-i}}{\overset{r_i}{\rightleftharpoons}} FeS_{(s)} + H^+$$

$$r_{\pm i} = \begin{cases} k_i(\Omega_i - 1) & \text{for } \Omega_i \geq 1 \\ k_{-i}[Q_i](\Omega_i - 1) & \text{for } \Omega_i < 1 \end{cases}$$

$$2\,FeOOH + HS^- + 5\,H^+ \xrightarrow{r_i} 2\,Fe^{+2} + S^0_{(s)} + 4\,H_2O$$

$$r_i = k_i[FeOOH_{(s)}][HS^-],$$

where r_i is the forward reaction rate for the precipitation of solid-phase species i, r_{-i} is the reverse reaction rate for the dissolutions of solid-phase species i, k_i is the precipitation rate constant of species i, k_{-i} is the dissolution rate constant of species i, Ω_i is the saturation ratio of species i and Q_i is the reaction quotient of species i. Ω_i and Q_i describe the distribution of species relative to the

distributions of reaction constituents at equilibrium. Unlike the four kinetic reactions describing microbial processes, mineral reactions can proceed in either direction. Deviation from equilibrium determines which way reactions will proceed, either to form mineral species i or dissolve species i into solution. For example, the saturation quotient of $CaCO_3$ is given as

$$Q_{\mathrm{FeCO_3}} = \frac{[\mathrm{H^+}]}{[\mathrm{Fe^{+2}}][\mathrm{HCO_3^-}]},$$

and the saturation ratio for $FeCO_3$ is given as

$$\Omega_{\mathrm{CaCO_3}} = \frac{Q_{\mathrm{FeCO_3}}}{K_{sp,\mathrm{FeCO_3}}}$$

where K_{sp} is the solubility product of $FeCO_3$, in this example.

3.1.2.4 Initial and boundary conditions

Batch and 1D transport calculations to investigate the dynamics of the kinetically controlled reaction processes are governed by Equation 3.1, which is first-order with respect to time, thus needing only an initial condition to solve given as

$$C_i(t=0) = C_{i,I}$$

where $C_{i,I}$ is the initial concentration of species i in the plume of uranium-contaminated groundwater. Batch calculations are zero-order with respect to distance and therefore do not need boundary conditions. However, 1D transport simulations are second-order with respect to distance, x, in Equation 3.2, and therefore need two boundary conditions. The boundary condition at the upstream boundary is a time-varying specified concentration and the boundary condition at the downstream boundary is a zero-gradient condition given as

$$C_{i,\text{ upstream}} = \begin{cases} C_{i,\text{ treat. sol.}} & \text{for } t \leq t_{inj} \\ C_{i,\text{areal}} & \text{for } t > t_{inj} \end{cases}$$

$$\frac{d}{dx} C_{i,\text{ downstream}} = 0$$

where $C_{i,\text{upstream}}$ and $C_{i,\text{ downstream}}$ is the concentration of species i at the upstream and downstream boundary, respectively, $C_{i,\text{ treat. sol.}}$ and $C_{i,\text{areal}}$ is the concentration if species i in the treatment solution and areal groundwater, respectively, and t_{inj} is the duration of the treatment solution injection.

3.1.3 Numerical Formulation

3.1.3.1 Flow and Transport Formulation

PHREEQC was employed for reactive transport in the batch and 1D transport simulations. Batch calculations were based on a volume of 1.0 L of water. 1D transport simulations were conducted using a 25 foot-long column discretized into 50 6-inch-wide cells. Darcy flux reported in site documents produced by the DOE [119] as $v = 0.7$ ft/d and the longitudinal dispersivity and effective diffusion coefficient from Curtis et al. [45] are $\alpha_L = 9.86$ ft and $D_e = 9.30 \times 10^{-4}$ ft^2/d. A time-step of $\Delta t_{transp.} = \Delta t_{reaction} = 0.7$ days was used for transport simulations. To avoid numerical dispersion, the spatial and temporal discretization was checked for numerical dispersion using the Peclet number $Pe \leq 2$ and the Courant number $Cr \leq 1$:

$$Pe = \frac{\Delta x}{\alpha_L} = \frac{0.5 \text{ ft}}{9.86 \text{ ft}} = 0.05 < 2$$

$$Cr = \frac{v\Delta t}{\Delta x} = \frac{(0.7 \text{ ft/d})(0.7 \text{ d})}{0.5 \text{ ft}} = 0.98 < 1$$

$K = 10$ ft/d and $n = 0.35$ were used to describe the porous medium used in batch and 1D transport simulations as these are the physical aquifer properties governing facies 2 of the hydrofacies model to describe heterogeneity at the field scale. Hydrofacies present in the field scale model are presented and discussed in Section 3.1.3.

Table 3.6 lists concentrations of the initial conditions occurring in the uranium-contaminated plume, the concentrations of constituents in the treatment solution and concentrations of areal flow used in batch calculations and 1D transport simulations. Treatment solution is the same as areal groundwater with an acetate amendment as treatment solution is often created mostly with uncontaminated groundwater present at the site [99].

3.1.3.2 Reaction Formulation

Plume concentrations of constituents present in the model from Curtis et al. [45] were set to values predicted by the model. If constituents were not present in the model from Curtis et al. [45], initial concentrations from Yabusaki et al. [180] were used in this investigation. Constituents present

Table 3.6: Concentrations of constituents present in each source in the batch and 1D transport simulation. Concentrations of aqueous, mobile species are in moles per liter of water (M), and solid-phase, immobile species are expressed in moles per liter of bulk aquifer volume (mol/L_b). All values are based on output from the model developed for Curtis et al. [45] unless otherwise noted.

Constituent	Plume	Treatment Solution	Areal[b]
Mobile species (M)			
[a]CH_3COO^-	–	3.84×10^{-3}	–
C(IV)	9.20×10^{-3}	5.39×10^{-3}	5.39×10^{-3}
Ca	3.70×10^{-3}	8.80×10^{-3}	8.80×10^{-3}
Cl	4.92×10^{-2}	5.00×10^{-3}	5.00×10^{-3}
[a]Fe(II)	7.00×10^{-5}	7.00×10^{-5}	7.00×10^{-5}
[a]FeRB	1.00×10^{-2}	1.00×10^{-2}	1.00×10^{-2}
K	2.30×10^{-4}	2.30×10^{-4}	2.30×10^{-4}
Na	1.68×10^{-1}	7.05×10^{-2}	7.05×10^{-2}
[a]NH_4^+	2.00×10^{-4}	2.00×10^{-4}	2.00×10^{-4}
Mg	2.73×10^{-3}	2.73×10^{-3}	2.73×10^{-3}
pH	7.3	7.1	7.1
S(VI)	6.15×10^{-2}	4.20×10^{-2}	4.20×10^{-2}
[a]SRB	1.00×10^{-7}	1.00×10^{-7}	1.00×10^{-7}
U(VI)	3.52×10^{-5}	6.08×10^{-8}	6.08×10^{-8}
Immobile species (mol/l_s)			
X	1.0×10^{-2}	–	–
$CaCO_{3(s)}$	1.0	–	–
[a]$FeOOH_{(s)}$	4.89×10^{-2}	–	–
[a]$Fe(III)_{(ls)}$	4.89×10^{-2}	–	–
Sw_OH	3.21×10^{-2}	–	–
Ss_OH	9.92×10^{-4}	–	–

Species not shown but present in the model: S(−II), $S(0)_{(s)}^{a}$, $Fe(II)_{(ls)}^{a}$, $FeS_{(s)}^{a}$, ${FeCO_3}^{a}{}_{(s)}$, ${UO_2}^{a}{}_{(a)}$ and decayed SRB, SRB_d^a, are set to initial concentrations of $[C_i] = 1 \times 10^{-20}$ as to not be ignored by the program.

[a] Concentrations used in Yabusaki et al. [180].

[b] Groundwater harvested from upgradient of the uranium plume used to make treatment solution as done in Long et al. [99].

in the Yabusaki et al. [180] model not present in the Curtis et al. [45] are all iron containing aqueous and mineral species, acetate (CH_3COO^-), ammonium (NH_4^+), and microbial species (FeRB and SRB). Constants used in the calculation of rates for kinetic reactions are shown in Table 3.7.

3.2 Field Scale Model

3.2.1 Conceptual Model

The shallow alluvial aquifer underlying the Naturita site is modeled as an unconfined aquifer discretized into a three-dimensional spatial grid oriented in the northeast direction as shown in

Table 3.7: Rate constants used in kinetic microbial reactions and kinetic mineral formation. All constants come from Yabusaki et al. [180] unless otherwise noted.

Rate Parameters		Value	Units
Microbial reaction rate parameters			
Goethite reduction rate constant	$\mu_{FeRB,\mathrm{FeOOH_{(s)}}}$	1.6×10^{-2}	$\mathrm{M^{-1}d^{-1}}$
Goethite adsorption site concentration	$\mathrm{C_{>FeOOH}}$	3.28×10^{-2}	M
Phyllosilicate iron reduction rate constant	$\mu_{FeRB,\mathrm{Fe(III)_{(ls)}}}$	7.5×10^{-2}	$\mathrm{M^{-1}d^{-1}}$
Sulfate reduction rate constant	$\mu_{SRB,\mathrm{SO_4{}^{-2}}}$	$4.00 \times 10^{+2}$	$\mathrm{d^{-1}}$
SRB first-order decay constant	$k_{decay,SRB}$	1.5×10^{-3}	$\mathrm{d^{-1}}$
Sulfate reduction rate maximum	R_{Ac}^{SRB}	3.3×10^{-3}	$\mathrm{M\ d^{-1}}$
[a]Sulfate half saturation	$K_{s,\mathrm{SO_4{}^{-2}}}$	1.0×10^{-5}	M
Uranyl reduction rate constant	$\mu_{FeRB,\mathrm{UO_2{}^{+2}}}$	2.5×10^{-6}	$\mathrm{M^{-1}\ d^{-1}}$
Uranyl half saturation	$K_{s,\mathrm{UO_2{}^{+2}}}$	1.0×10^{-7}	M
Acetate stoichiometric coefficient	S_{Ac}	0.125	–
Acetate half saturation	$K_{s,Ac}$	5.0×10^{-4}	M
Mineral reaction rate parameters			
Siderite solubility product	$K_{sp,\mathrm{FeCO_{3(s)}}}$	6.50×10^{-1}	–
Siderite precipitation rate constant	$k_{i,\mathrm{FeCO_{3(s)}}}$	1.37×10^{-6}	$\mathrm{M\ d^{-1}}$
Siderite dissolution rate constant	$k_{-i,\mathrm{FeCO_{3(s)}}}$	1.37×10^{-7}	$\mathrm{d^{-1}}$
Mackinawite solubility product	$K_{sp,\mathrm{FeS_{(s)}}}$	5.11×10^{-6}	–
Mackinawite precipitation rate constant	$k_{i,\mathrm{FeS_{(s)}}}$	6.85×10^{-6}	$\mathrm{d^{-1}}$
Mackinawite dissolution rate constant	$k_{-i,\mathrm{FeS_{(s)}}}$	2.25×10^{-4}	$\mathrm{d^{-1}}$
Elemental sulfur precipitation rate constant	$k_{i,\mathrm{S^0_{(s)}}}$	$2.08 \times 10^{+2}$	$\mathrm{M^{-1}\ d^{-1}}$

[a] Fang et al. [54]

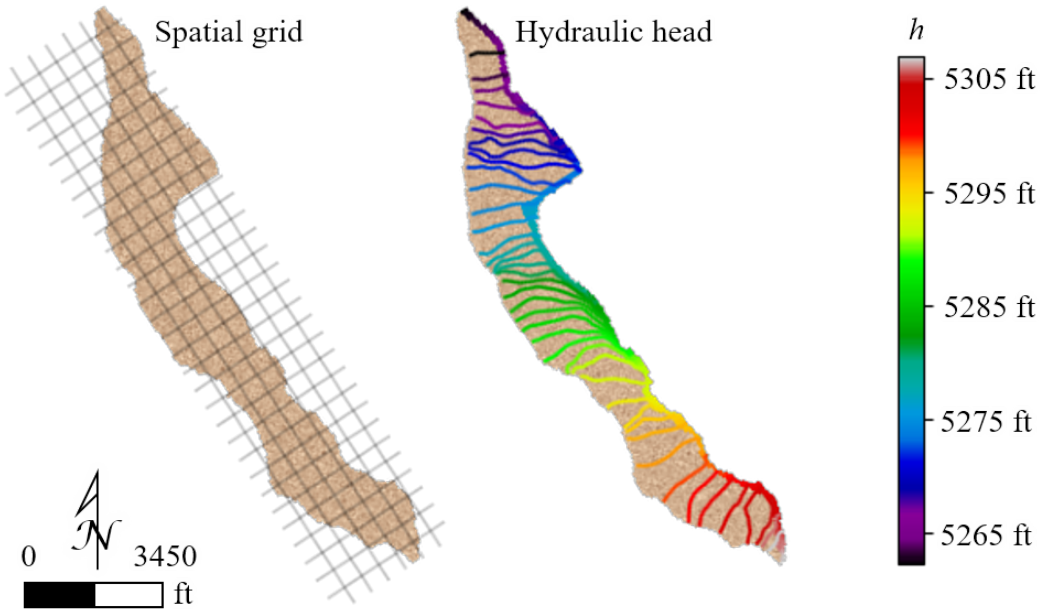

Figure 3.2: The left hand plot is a plan view of the site model boundaries and the orientation of the grid used in the flow and reactive transport model. Visible grid blocks represent a 10×10 area of model grid cells. The active model area is shown by the sand-textured, light brown area. The right hand plot shows the hydraulic head distribution occurring on the site. Hydraulic head contours are shown in one foot intervals with values corresponding to colors shown in the colorbar on the far right hand side of the plot. Shading of the river area is indicative of the head value in the river at that location.

Figure 3.2 to match the general direction of areal groundwater flow. As shown in the right hand plot in Figure 3.2, hydraulic head generally decreases along the centerline of the site from the southeast edge to the northern boundary of the site. The direction of groundwater flow runs generally parallel to the river from the southeast extent to the northern extent of the site.

The model encompasses a plan area of 141 acres discretized into a $310 \times 69 \times 3$ grid per Curtis et al. [45]. Grid cells are 25.0×25.1 ft in the $x - y$ plane and vary in the vertical direction. The thickness of layer one (top layer) varies in space between 38.0 ft and 75.0 ft generally increasing in thickness from the southeastern end of the site to the northern part of the site. The top layer was made sufficiently thick in order ensure no cells went dry during the simulation. Layers two and three are 1.0 ft and 5.0 ft thick, respectively [103].

3.2.1.1 Boundary Conditions

The site is bounded by CO Highway 141 to the south and west and the San Miguel River to the north and east which gives the site its general shape as shown in Figure 3.2. The thickness of the alluvium generally decreases away from the river to zero near CO Highway 141, where the underlying Brushy Basin Member becomes exposed to the surface. A zero head gradient boundary condition is used along the entire boundary of the active model domain.

3.2.1.2 Sources and Sinks

The aquifer system is subject to water fluxes from the San Miguel River, natural recharge, and active wells during *in situ* remediation, all of which recharge or drain water and aqueous species.

The San Miguel River acts as a source and sink for the alluvial aquifer. Flow from the river recharges the aquifer through the southeastern boundary and discharges to the river on the northern extent of the site on the Maupin property. The area modeled has been expanded (141 acres) compared to the regulatory area shown in Figure 2.1 (79 acres) because river interactions occur upgradient of the former mill site. A similar situation occurs north of the downgradient edge of the regulatory site. Groundwater flows from the area of former tailings in the center of the regulatory site into the Maupin property. Area of the Maupin property included in the model exists in the "bunny hat" of the site, in the area bounded by the river and the highway north until the river and highway nearly meet again. The area modeled has been extended upgradient to CO Highway 141 and the San Miguel River rendezvous at the southeastern point of the site and also downgradient to the confluence of the river and the highway on the northern edge of the model area on the Maupin property. The former ore storage area is not incorporated in this model because the alluvial aquifer does not extend across CO Highway 141.

The aquifer is also recharged by a constant flux boundary representing precipitation. Natural recharge from precipitation is uniformly distributed in the former location of tailings on the site shown in Figure 3.3.

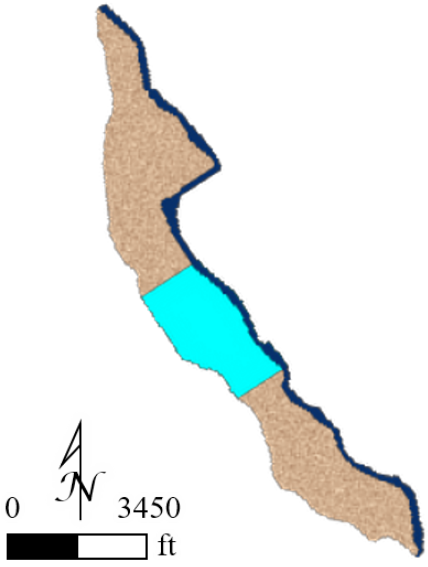

Figure 3.3: Plan view of the site showing the area of where recharge is applied. The sky blue shaded stripe is the area over which recharge is applied to the uppermost model layer in the unconfined aquifer Areas without the teal color do not receive recharge. The river flux boundary is shown as the navy blue area. Both of these process occur in the first layer only.

The well injecting the treatment chemical is placed near the center of the contaminant plume. EIE wells are placed in a five-spot well pattern about the plume oriented in the direction of areal groundwater flow. Following the injection of the treatment chemical of the five wells present are active for each of the twelve steps of the EIE sequence.

The wells used in three-well injection gallery remediation system are placed near the up-stream extent of the EIE wells. Two additional wells are placed on either side of the center well perpendicular to flow. The same mass of treatment solution is injected through the three wells employed in this approach active over the entire EIE remediation period. The rate of injection ensures that cumulative mass of treatment chemical and water are the same for the well-field and EIE process.

3.2.2 Mathematical Model

Field scale flow simulations were conducted using MODFLOW 2005 – the USGS three-dimensional finite-difference ground-water model [69] to solve the three-dimensional groundwater flow equation for an unconfined aquifer system given as

$$S_y \frac{\partial h}{\partial t} = \frac{\partial}{\partial x}\left(K(h-\xi)\frac{\partial h}{\partial x}\right) + \frac{\partial}{\partial y}\left(K(h-\xi)\frac{\partial h}{\partial y}\right) + N + \sum_{j=1}^{N_w} Q_j \delta(\mathbf{x} - \mathbf{x_{w,j}}) + \frac{G_r}{A_r}(h_r - h)\big|_{\mathbf{x}=\mathbf{x_r}}$$

where $S_y(\mathbf{x})$ is the spatially varying specific yield, $\mathbf{x} = (x, y, z)$ is the spatial coordinate, $h(\mathbf{x}, t)$ is the spatially and temporally varying hydraulic head, t is time, $\xi(\mathbf{x})$ is the spatially varying elevation of the aquifer bottom, $K(\mathbf{x})$ is the spatially varying hydraulic conductivity, $N(\mathbf{x})$ is the spatially varying recharge, Q_j is the pumping or recharge rate from a well located at $\mathbf{x_{w,j}}$, N_w is the total number of wells, $\delta(\cdot)$ is the Dirac delta function, and G_r is the conductance of river bed, A_r is the area of the riverbed in hydraulic connection with the underlying aquifer, and $h_r(\mathbf{x_r})$ is the head in the river at $\mathbf{x_r}$.

At the boundary of the active model domain, there exists a zero head gradient boundary condition given as

$$\nabla h \cdot \mathbf{n} = 0$$

and the initial conditions for head are given as

$$h(\mathbf{x}, t = 0) = h_{t=0}$$

where $\mathbf{n}$ is the outward unit-normal vector to the boundary, $h_{t=0}(\mathbf{x})$ is the spatially varying initial head distribution equal to the final head distribution from the Curtis et al. [45] model as shown in Figure 3.2.

Packages included in MODFLOW were employed to model the river, recharge, and well sources/sinks. The recharge and river packages were employed to model natural recharge and hydraulic interactions with the San Miguel River, respectively [69]. Version 1 of the Multi-Node Well Package was used to model well hydraulics specific to each aquifer layer [68] because the updated Version 2 of the Multi-Node Well Package is unable to interface with the transport package

used. The Link to the MT3DMS contaminant transport model (LMT) package was employed to pass flow model results to the reactive transport model.

Reactive transport simulations were conducted using PHT3D – a reactive multicomponent transport model for saturated porous media [142]. PHT3D version 2.10 [142] incorporates MT3DMS [185] release 5.3, a three-dimensional advection-dispersion multi-species transport code, with an earlier version (2.17) of PHREEQC [133]. PHT3D was employed to solve the three-dimensional advection-dispersion-reaction equation given as

$$n\frac{\partial C_i}{\partial t} = \nabla \cdot n\mathbf{D}\nabla C_i - \nabla \cdot n\mathbf{v}C_i + N\frac{C_{N,i}}{\Delta z} + \sum_{j=1}^{N_w} Q_{s,i,j} + R_s + R_{\mathrm{r},i}$$

where $n(\mathbf{x})$ is the spatially varying porosity, $C_i(\mathbf{x}, t)$ is the spatially and temporally varying concentration of species i, $\mathbf{D}(\mathbf{x})$ is the spatially varying dispersion tensor given as

$$D_{xx} = \alpha_L \frac{v_x^2}{|\mathbf{v}|} + \alpha_{TH}\frac{v_y^2}{|\mathbf{v}|} + \alpha_{TV}\frac{v_z^2}{|\mathbf{v}|} + D_e$$

$$D_{yy} = \alpha_L \frac{v_y^2}{|\mathbf{v}|} + \alpha_{TH}\frac{v_x^2}{|\mathbf{v}|} + \alpha_{TV}\frac{v_z^2}{|\mathbf{v}|} + D_e$$

$$D_{zz} = \alpha_L \frac{v_z^2}{|\mathbf{v}|} + \alpha_{TV}\frac{v_x^2}{|\mathbf{v}|} + \alpha_{TV}\frac{v_y^2}{|\mathbf{v}|} + D_e$$

$$D_{yx} = D_{xy} = (\alpha_L - \alpha_{TH})\frac{v_x v_y}{|\mathbf{v}|}$$

$$D_{zx} = D_{xz} = (\alpha_L - \alpha_{TV})\frac{v_x v_z}{|\mathbf{v}|}$$

$$D_{zy} = D_{yz} = (\alpha_L - \alpha_{TV})\frac{v_y v_z}{|\mathbf{v}|},$$

where α_L, α_{TH}, and α_{TV} are the longitudinal, transverse horizontal and the transverse vertical dispersivities, respectively, D_e is the diffusion coefficient, and $\mathbf{v}(\mathbf{x}, t)$ is the spatially and temporally varying groundwater velocity given in a solution to Darcy's Law as

$$\mathbf{v} = -\frac{K}{n}\nabla h,$$

$C_{i,N}$ is the concentration of species i in the recharge sources, $\Delta z(\mathbf{x})$ is the spatially varying aquifer thickness, Q_s is the source or sink term for well interactions given as

$$Q_{s,i,j} = \begin{cases} 0 & \text{for } Q_j = 0 \\ \frac{Q_j}{\Delta z} C_{w,i} \delta(\mathbf{x} - \mathbf{x_{w,j}}) & \text{for } Q_j > 0 \\ \frac{Q_j}{\Delta z} C_i \delta(\mathbf{x} - \mathbf{x_{w,j}}) & \text{for } Q_j < 0, \end{cases}$$

where $C_{w,i}$ is the concentration of species i present in injected water, R_s is the source or sink term for river interactions given as

$$R_s = \begin{cases} 0 & \text{for } h_r = h \\ \frac{G_r}{A_r} \frac{C_{r,i}}{\Delta z} (h_r - h)\big|_{river} & \text{for } h_r > h \\ \frac{G_r}{A_r} \frac{C_i}{\Delta z} (h_r - h)\big|_{river} & \text{for } h_r < h \end{cases}$$

where $C_{r,i}$ is the concentration of species i in the river, and $R_{\text{reaction},i}$ is the accumulation or loss of species i through chemical reaction.

Similar to the flow model, there exists a zero spatial concentration gradient boundary condition at the model boundary, given as

$$\nabla C_i \cdot \mathbf{n} = 0$$

and the initial conditions for concentration are given as

$$C_i(\mathbf{x}, t = 0) = C_{i,t=0}$$

where $C_i(\mathbf{x})$ spatially varying initial concentration distribution for species i, equal to the final concentration distribution from the Curtis et al. [45]

3.2.3 Numerical Formulation

3.2.3.1 Flow and Transport Formulation

Field scale aquifer heterogeneity is represented by varying distributions of three hydrofacies within each layer. Facies represent varying aquifer material exhibiting different aquifer properties

Table 3.8: Physical and temporal parameter values used in the governing equations for the field scale flow and transport model [103]. Parameters with one value listed implies the parameter is constant across all facies.

Parameter Name		Value			Units
		Facies 1	Facies 2	Facies 3	
Flow model parameters					
Mean hydraulic conductivity	$\bar{K}$	30.0	10.0	1.00	ft/d
Specific storage	S_s	1.050×10^{-4}	1.051×10^{-4}	1.052×10^{-4}	1/ft
Specific yield	S_y	0.25	0.20	0.10	–
Transport model parameters					
Porosity	n	0.40	0.35	0.25	–
Longitudinal dispersion coeff.	α_L		9.84		ft
Transverse horiz. dispersivity	α_{TH}		9.84×10^{-3}		ft
Transverse vert. dispersivity	α_{TV}		9.84×10^{-3}		ft
Effective diffusion coeff.	D_e		9.30×10^{-4}		ft^2/d

influencing flow and transport on the site. Facies 1 is the most permeable, facies 2 is moderately permeable, and facies 3 is the least permeable. Within each facies, K values are distributed about the respective mean K, $\bar{K}$, presented in Table 3.8. The development of the final spatial distribution of the K field for each layer is outlined in Lu et al. [103] and shown in Figure 3.4.

Site investigations conducted at the Naturita site show the distribution of facies 1, 2, and 3 within bulk sediment is 0.3, 0.2, and 0.5 [103]. Although the distribution of the total amount of each facies over all three layers distributed in the aforementioned way, different proportions of each facies exist in each layer. In layer 1, an increased amount of facies 1 and 2 is present to allow for increased infiltration into the lower 2 and the comparatively thin layer 2 houses an increased amount of facies 3 to represent a semi-confining layer [103]. The distribution of facies in each layer is shown in Figure 3.4 by the distribution of hydraulic conductivity. This distribution is used for the spatial distribution of other aquifer properties needed for transient flow and reactive transport models including specific storage (S_s), specific yield (S_y), and porosity (n) as presented in Table 3.8. A value for specific yield is needed in layer 1 only because it is the only model layer explicitly

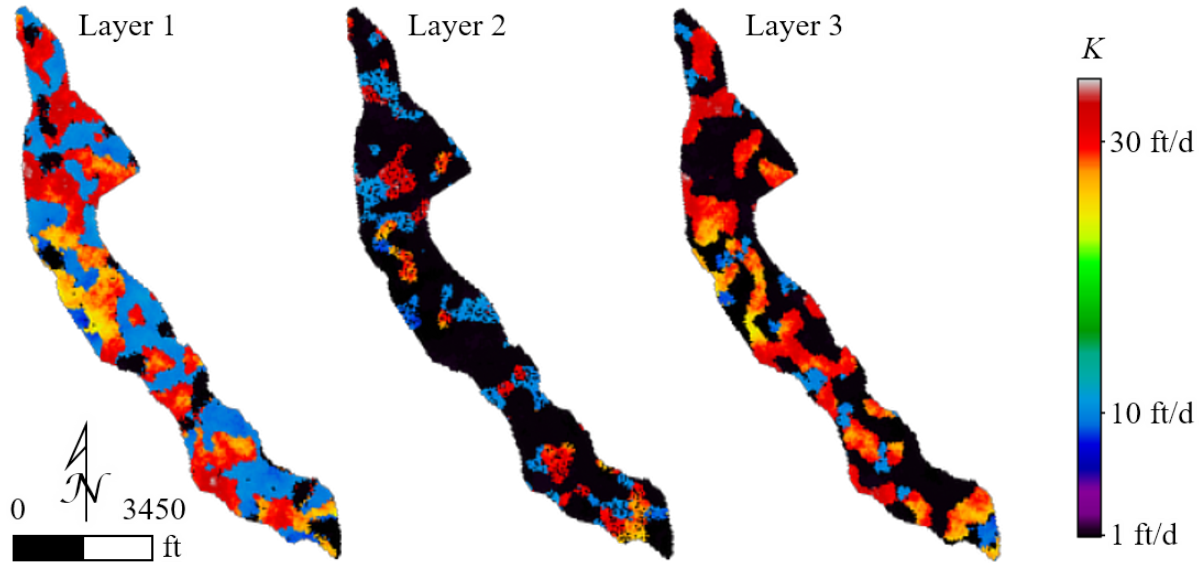

Figure 3.4: Hydraulic conductivity distribution in each layer from Lu et al. [103]. Values for the mean hydraulic conductivity $\bar{K}$ are labeled on the colorbar for facies 1 with $\bar{K} = 30.0$ ft/day, facies 2: $\bar{K} = 10.0$ ft/day, and facies 3: $\bar{K} = 1.0$ ft/day.

modeled as an unconfined layer. Specific yield was calculated using an estimated field capacity of $\Theta_u = 0.15$ in the following equation

$$S_y = n - \Theta_u$$

where $S_y(\mathbf{x})$ is the spatially varying specific yield, $n(\mathbf{x})$ is the spatially varying porosity. The field capacity was estimated based on field capacities presented in Saxton and Rawls [153] and Fitts [58] for various soils and soil characterizations conducted at the Naturita site [38, 119]. Specific storage (S_s) was calculated using

$$S_s = \gamma(n\beta + \alpha)$$

where $S_s(\mathbf{x})$ is the spatially varying specific storage over $\mathbf{x} = (x, y, z)$, γ is the specific weight of water ($\gamma = 62.43$ lb/ft^3), α is the compressibility of the bulk aquifer material ($\alpha = 1.68 \times 10^{-6}$ ft^2/lb) and β is the compressibility of water ($\beta = 2.15 \times 10^{-8}$ ft^2/lb).

Each EIE step including the treatment chemical injection step is 30 days. 30 days is not sufficiently long enough for the system to reach steady-state following abrupt pumping changes from

EIE one step to the next. As a result flow and transport simulations are transient to encompass head response to sharp changes in pumping occurring between EIE steps. Aquifer properties were used to determine the initial time-step size, subsequent time-step scaling and the number of time steps for each stress period. For unconfined layer 1, the initial time-step length, $t_0(z)$, based on properties in layer 1 is calculated through

$$t_0 = \frac{S_y \bar{a}^2}{4\bar{K}\overline{(h-\xi)}}$$

where $\bar{a}$ is the average of the horizontal grid discretization, $\bar{K}$ is the weighted average of hydraulic conductivity in the layer weighted by the relative amount of each facies is present in the layer, and $\overline{(h-\xi)}$ is the saturated thickness in unconfined layer 1. For confined layers 2 and 3, the initial time-step, $t_0(z)$, is found through

$$t_0 = \frac{S_s \bar{a}^2}{4\bar{K}b}$$

where b is the confined layer thickness. The initial time-step is the minimum value of t_0 found for each layer, z. The number of time steps, n_t is found through

$$n_t = \frac{\log[t_0 + L(r-1)] - \log(t_0)}{\log(r)}$$

where L is the total stress period length and r is the multiple by which time-steps increase throughout the stress period. Anderson et al. [9] suggests $r = 1.4$ is adequate to model transient changes present due to abrupt changes in the aquifer system without sacrificing computational efficiency. One stress period is used per injection and EIE step and based on the above calculation 20 steps per stress period are needed to accurately capture the abrupt changes in the model due to pumping rate and location changes from one EIE step to the next.

Parameters governing recharge, interactions with the San Miguel River and wells involved in both remediation systems tested are shown in Table 3.9 and additional information on the EIE sequence employed is given in Table 3.10. The EIE sequence employed was developed in Mays and Neupauer [105] to inject and extract a net neutral amount of water throughout the twelve-step EIE period. Long et al. [99] conducted field scale tests for *in situ* bioremediation of uranium-contaminated groundwater at the Old Rifle site and used an injection rate 6.0 ft^3/day for each

Table 3.9: Parameters employed for the recharge, well, and river flux boundary conditions. Here, injection refers to the injection of the treatment solution.

Flux parameter		**Value**	**Units**
Recharge			
Recharge flux	N_k	2.7×10^{-3}	ft/d
River			
River bed conductance	G_r	10.0	ft^2/d
Three-well injection gallery			
Injection Rate	Q_{inj}	6	ft^3/d/well
Injection Duration	T_{inj}	390	days
Five-spot EIE			
Injection Rate	Q_{inj}	234.0	ft^3/d
Injection Duration	T_{inj}	30	days

active well. This rate is used over a 390.0 day period in the three-well injection gallery remediation system to match the duration of the EIE remediation system. To ensure the mass of treatment chemical injected is constant over the two remediation systems, the 30 day injection in the center well, is 234.0 ft^3/day. The EIE sequence is shown in Table 3.10 defining the active pumping well and associated injection or extraction rate for each step.

Well locations for the three-well injection gallery and EIE system are shown in Figure 3.5. A general plume of uranium-contaminated groundwater exists in the rabbit hat portion of the site on the northern end of the regulatory site onto the Maupin property. This plume is much larger than can be expected to be fully remediated by one occurrence of a remediation system. For this investigation, three remediation systems are investigated for comparison to each other, not for the purpose of widespread remediation at the site.

Sources and sinks of water originating from wells, recharge and the river have different aqueous distributions. The distribution of aqueous species present in the field scale are shown for each other sources/sinks of water in Table 3.11. Conceptually, treatment solution is made by mixing acetate with water harvested from a pumping well upstream of the area of uranium-contaminated

Table 3.10: Active well location and injection rate for the two 12-step EIE sequences employed. Positive rates are rates of clean water injection, while negative rates are rates of clean water extraction.

Step	EIE 1		EIE 2	
	Well	**Rate (ft^3/d)**	**Well**	**Rate (ft^3/d)**
1	West	819.0	North	819.0
2	East	819.0	South	819.0
3	West	-234.0	North	-234.0
4	East	-702.0	South	-702.0
5	West	-374.4	North	-374.4
6	East	-327.6	South	-327.6
7	North	819.0	West	819.0
8	South	819.0	East	819.0
9	North	-234.0	West	-234.0
10	South	-702.0	East	-702.0
11	North	-374.4	West	-374.4
12	South	327.6	East	327.6

Table 3.11: Concentrations in moles per kilogram of water (M) of constituents present in each recharge source. Mineral and surface species are not included in this table because source water is assumed to be free of solid phase minerals and materials containing adsorption sites.

Constituent	River[a]	Natural Recharge	Treatment Solution
CH_3COO^-	0	0	3.84×10^{-3}
C(IV)	5.39×10^{-3}	9.40×10^{-3}	5.39×10^{-3}
Ca	8.80×10^{-3}	3.67×10^{-3}	8.80×10^{-3}
Cl	5.00×10^{-3}	5.00×10^{-2}	5.00×10^{-3}
Fe(II)	3.58×10^{-6}	3.58×10^{-6}	3.58×10^{-6}
FeRB	1.00×10^{-2}	1.00×10^{-2}	1.00×10^{-2}
K	2.30×10^{-4}	2.30×10^{-4}	2.30×10^{-4}
Na	7.06×10^{-2}	1.70×10^{-1}	7.06×10^{-2}
NH_3^+	6.25×10^{-6}	6.25×10^{-6}	6.25×10^{-6}
Mg	2.73×10^{-3}	2.73×10^{-3}	2.73×10^{-3}
pH	7.1	7.3	7.1
S(VI)	4.20×10^{-2}	6.20×10^{-2}	4.20×10^{-2}
SRB	1.00×10^{-7}	1.00×10^{-7}	1.00×10^{-7}
U(VI)	6.08×10^{-8}	4.95×10^{-5}	6.08×10^{-8}

[a] equivalent to background water quality.

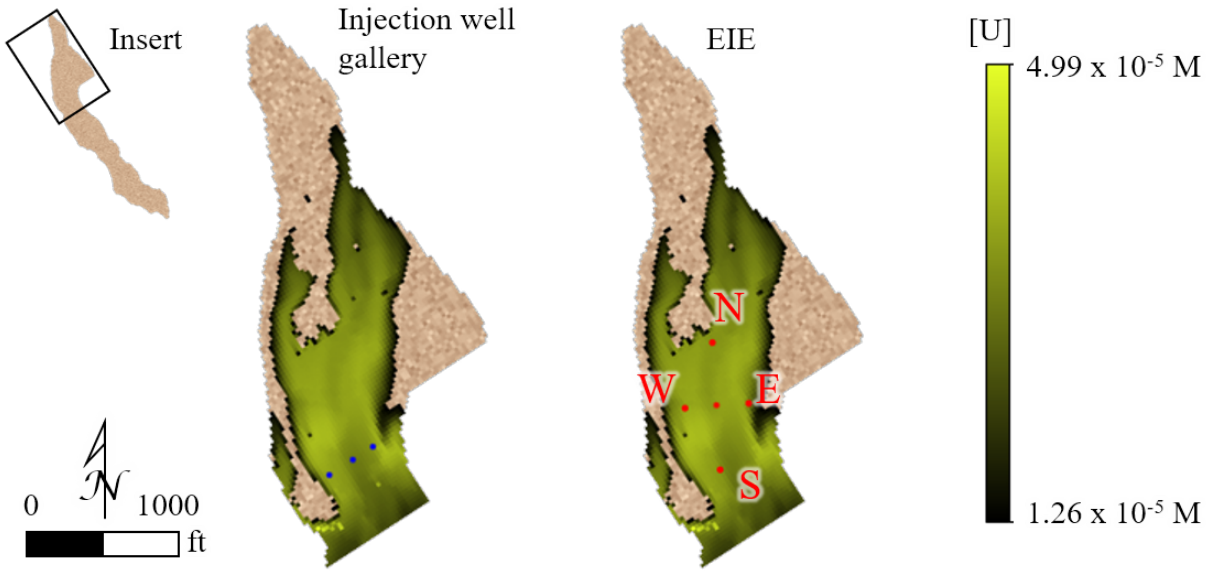

Figure 3.5: Plots showing the northern edge of the site along with the Maupin property. The plot on the right shows the location of wells as red dots used in EIE along with the well locations for the three-well injection well gallery system shown in the left hand plot as blue dots. EIE wells are referred to by the cardinal direction of the their location relative to the center well. Uranium concentration is shown in the aquifer plan area to show the distribution and extent of the uranium-contaminated groundwater plume. Areas shown without a color present on the colorbar are areas where the aqueous concentration of uranium is less than the EPA maximum contaminant level of $[\mathrm{U}]_{\mathrm{MCL}} = 1.26 \times 10^{-5}$ [120].

groundwater. In this investigation, water is theoretically harvested from a pumping well south of the south eastern boundary of the regulatory area. Groundwater in this area of the shallow alluvial aquifer is of much higher water quality and is generally water that has been introduced from the San Miguel River into the alluvial aquifer and therefore consists of the same distribution of aqueous species as in the San Miguel River. EIE injection steps have traditionally made use of "clean water," which was defined as pure water free of contaminants or treatment chemicals [138, 136, 137, 114, 113]. For this study and general applicability, "clean water" here refers to groundwater harvested upgradient from the area of uranium-contaminated groundwater, so injected water has the same species distribution as does San Miguel River water as shown in Table 3.11.

Initial conditions for the flow model are the output of the flow model from Curtis et al. [45].

Table 3.12: Equilibrium formation equations and distribution coefficients K_d for each hydrofacies for uranium species adsorbing to aquifer media at the Naturita site.

Equation	$\text{Log}(K_d)$	Concentration[a]
Facies 1		
$\text{Rw\_OH} + {UO_2}^{+2} \rightleftharpoons \text{Rw\_O}{UO_2}^{+} + H^{+}$	2.8	7.48×10^{-3}
$\text{Rs\_OH} + {UO_2}^{+2} + {CO_3}^{-2} \rightleftharpoons \text{Rs\_O}{UO_2}{CO_3}^{-} + H^{+}$	10.0	1.53×10^{-4}
Facies 2		
$\text{Sw\_OH} + {UO_2}^{+2} \rightleftharpoons \text{Sw\_O}{UO_2}^{+} + H^{+}$	2.7	3.21×10^{-2}
$\text{Ss\_OH} + {UO_2}^{+2} + {CO_3}^{-2} \rightleftharpoons \text{Ss\_OH}{UO_2}{(CO_3)_2}^{-2}$	22.0	9.92×10^{-4}
Facies 3		
$\text{Tw\_OH} + {UO_2}^{+2} + {CO_3}^{-2} \rightleftharpoons \text{Tw\_O}{UO_2}{CO_3}^{-} + H^{+}$	7.4	7.02×10^{-2}
$\text{Ts\_OH} + {UO_2}^{+2} + {CO_3}^{-2} \rightleftharpoons \text{Ts\_O}{UO_2}{CO_3}^{-} + H^{+}$	9.2	2.39×10^{-3}
$\text{Ts\_OH} + {UO_2}^{+2} + 2\,{CO_3}^{-2} \rightleftharpoons \text{Ts\_O}{UO_2}{(CO_3)_2}^{-3} + H^{+}$	15.4	
$\text{Tv\_OH} + {UO_2}^{+2} + 2\,{CO_3}^{-2} \rightleftharpoons \text{Tv\_O}{UO_2}{(CO_3)_2}^{-3} + H^{+}$	16.4	1.17×10^{-4}

[a]Concentrations are given as moles per liter of bulk aquifer volume (L_b).

The distribution of hydraulic head presented in Figure 3.2 is the initial distribution of hydraulic head employed. Initial conditions for other species present in varying concentrations from the Curtis et al. [45] model, Ca^{+2}, $CaCO_{3(s)}$ ${CO_3}^{-2}$, Cl^{-}, K^{+}, Na^{+}, ${Mg_2}^{+}$, ${SO_4}^{-2}$, ${UO_2}^{+2}$, and pH generally mimic the initial conditions from Figure 3.6 used in the batch and 1D transport studies. The remaining species are set to the initial concentrations presented in Table 3.6.

Reaction frameworks from the batch and 1D transport simulations previously presented in Sections 3.1.2.2 and 3.1.2.3 also govern kinetic and equilibrium reaction with the exception of the uranium-containing surface species. To model adsorption heterogeneity, uranium-containing surface species vary in each hydrofacies as shown in Table 3.12. All three facies have two sites named for their affinity to adsorb uranium: "w" for weak and "s" for strong; facies 3 has an additional very strong "v" site. Concentrations and equilibrium distribution coefficients for each of the sites and species in each Facies are also given in Table 3.12.

Chapter 4

Results and Discussion

Results from batch, 1D transport and field-scale investigations are presented in this chapter. Batch investigations provide insight into the dynamics of microbial and mineral kinetic reactions and their relationship with equilibrium species. 1D transport simulations provide insight into how these relationships develop as the treatment solution travels through the plume of uranium contaminated groundwater. Then the field-scale model was employed to compare the three-well injection gallery to engineered injection and extraction (EIE) for their simulated ability to remove uranium from contaminated groundwater at the Naturita site.

4.1 Batch Simulation

Batch simulations were conducted to simulate the chemical and biological reactions occurring following the injection of the treatment solutions (Table 3.6) into the plume of uranium-contaminated groundwater.

4.1.1 Carbon System

Acetate (CH_3COO^-) and the carbonate system ($CO_3{}^{-2}$ species) are the two chemical pools of carbon relevant to this investigation. During microbial metabolism, acetate is oxidized to form bicarbonate by native dissimilatory microbial communities for use in their metabolism. Figure 4.1 shows the concentration of acetate over time during the batch simulation. Acetate is consumed at an increasing rate by native dissimilatory microbes as time passes in the batch simulation. The

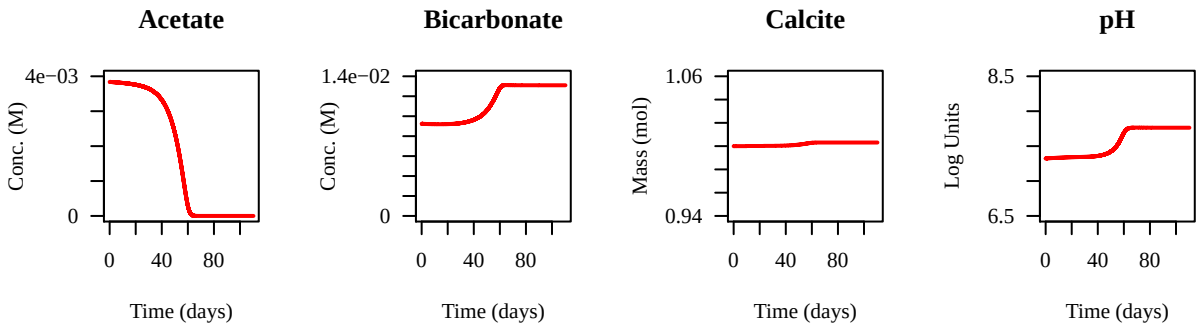

Figure 4.1: Concentrations of acetate (CH_3COO^-) and bicarbonate HCO_3^-, mass of calcite ($CaCO_3$) and pH with time during the batch simulation.

rate becomes very rapid near $t = 40$ days until $t \approx 60$ days when the introduced acetate has been completely consumed. Following the complete consumption of introduced acetate, all kinetic biological reactions cease and the system reaches steady state.

All carbon introduced to the system as acetate eventually becomes aqueous bicarbonate. The aqueous bicarbonate concentration increases at an increasing rate until acetate consumption begins to slow before complete consumption near $t = 60$ days. The calcite mineral $CaCO_{3(s)}$, in equilibrium with the batch solution, begins to precipitate as aqueous bicarbonate is introduced in solution resulting from acetate consumption by microbes. The precipitation of calcite mimics the temporal trend of bicarbonate as increased bicarbonate facilitates increase calcite precipitation. The pH of solution also increases in the same fashion as bicarbonate.

4.1.2 Sulfur System

Three valence states of sulfur are present in the reaction framework applied to the Naturita site for this work: S(VI) as ${SO_4}^{-2}$ species, S(0) as $S^0_{(s)}$, and S(−II) as HS^- species as shown in Figure 4.2. Sulfate reducing bacteria, SRB, reduce ${SO_4}^{-2}{}_{(aq)}$ to $HS-_{(aq)}$. Initially, the mass of SRB is five orders of magnitude lower than their iron-reducing counterparts FeRB because as SRB communities grow, they quickly dominate the consumption of acetate and microbial activity.

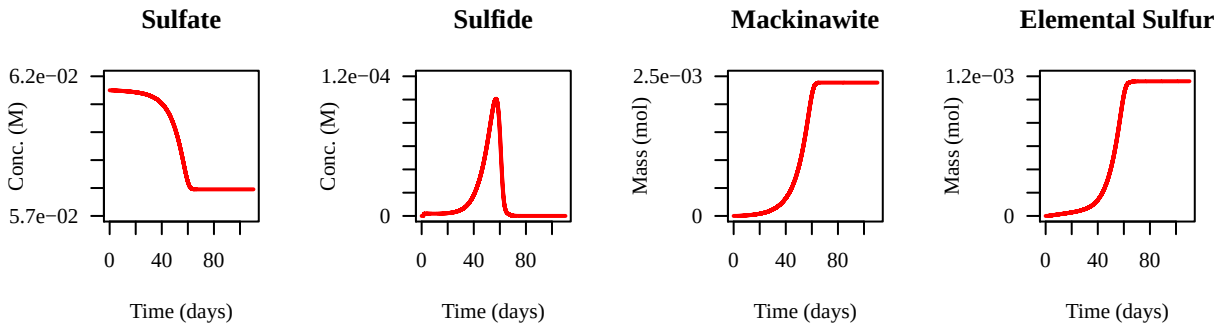

Figure 4.2: From the left, concentrations of sulfate ${SO_4}^{-2}{}_{(aq)}$], and hydrogen sulfide HS$-_{(aq)}$, mackinawite $FeS_{(s)}$, and elemental sulfur $S^0_{(s)}$ during the batch simulation. Sulfate reduction becomes significant near $t = 40$ days and dominates acetate consumption until acetate is completely consumed near $t = 60$ days.

Sulfate reduction is the only reduction process which its rate depends on the mass of microbial biomass. SRB mass is also governed by first-order decay and limited to a maximum rate. The dependence of sulfate reduction on the mass of SRB and low initial concentration was necessary to match field observations of sulfate reduction present during field investigations at the Old Rife site [180, 15].

Figure 4.2 shows concentrations of sulfur-containing aqueous (${SO_4}^{-2}$ and HS^-) and mineral species (mackinawite and elemental sulfur). Sulfur is initially present in the aquifer system as aqueous sulfate, ${SO_4}^{-2}{}_{(aq)}$, which is then reduced to aqueous hydrogen sulfide HS^-. HS^- resulting from sulfate reduction peaks just prior to the complete consumption of acetate near $t = 60$ days. Once the microbial reduction of ${SO_4}^{-2}$ ceases with the consumption of acetate, HS^- concentration sharply decreases back to zero. However, the steady state concentration of ${SO_4}^{-2}$ is lower than its initial value. During sulfate reduction, elevated aqueous HS^- drives the formation of two minerals, mackinawite ($FeS_{(s)}$) and elemental sulfur ($S^0_{(s)}$) through kinetic mineral processes.

Along with aqueous ferrous iron $Fe^{+2}_{(aq)}$ produced from iron reduction, HS^- forms mackinawite $FeS_{(aq)}$. Elemental sulfur reacts with solid-phase goethite $FeOOH_{(s)}$ to reduce ferric iron Fe(III) present in goethite to ferrous aqueous iron (Fe^{+2}) while oxidizing HS^- from S(-II) to S(0) forming

precipitating elemental sulfur $S^0_{(s)}$. The formation rate of mackinawite and elemental sulfur are directly correlated with the aqueous hydrogen sulfide concentration. As presented in Figure 4.2, HS^- formation is low until $t \approx 40$ days when the rate of sulfate reduction becomes pronounced. From $t \approx 40$ days until acetate is completely consumed, the rate of sulfate reduction increases at an increasing rate to values two orders of magnitude greater than those present in the other terminal electron acceptor processes (TEAPs) dependent on iron-reduction. Once acetate is completely consumed, the sulfur system reaches steady state. Residual aqueous HS^- in solution sharply decreases to zero because it is precipitated as mackinawite or elemental sulfur following the complete consumption of acetate.

4.1.3 Iron System

Iron present at the Naturita site is represented by aqueous ferrous iron Fe^{+2}, and goethite, ($FeOOH_{(s)}$), phyllosilicate ferric and ferrous iron, ($Fe(III)_{(ls)}$ and $Fe(II)_{(ls)}$, respectively), siderite ($FeCO_{3(s)}$) and mackinawite ($FeS_{(s)}$). Ferrous iron used in iron reduction is sourced from ferrous iron Fe(III) housed in goethite and phyllosilicates. Iron from these sources is reduced by iron-reducing microbes to from ferric iron species. When reduced, iron sourced from goethite produces aqueous ferric iron (Fe^{+2}), while iron sources from phyllosilicates primarily (90%) remains in mineral form, while the remaining (10%) is introduced into solution as $Fe^{+2}_{(aq)}$. Ferric iron is also introduced into solution through the sulfide-promoted dissolution of goethite to form elemental sulfur.

Figure 4.3 shows the concentration and iron species during the batch simulation. Phyllosilicate ferrous iron reduction is nearly constant resulting in a nearly linear decrease in phyllosilicate ferrous iron with time prior to complete acetate consumption near $t = 60$ days. When sulfate reduction becomes dominant and acetate is consumed very quickly $t = 40$ days and $t = 60$ days, the rate of ferrous phyllosilicate iron decreases to zero because the concentration of sharp acetate concentration decline. The rate of phyllosilicate ferrous iron reduction is also dependent on its mass. During the batch simulation less than 1% of the initial mass of phyllosilicate ferrous iron is lost to reduction, so the depletion of acetate drives the decrease in phyllosilicate ferrous iron

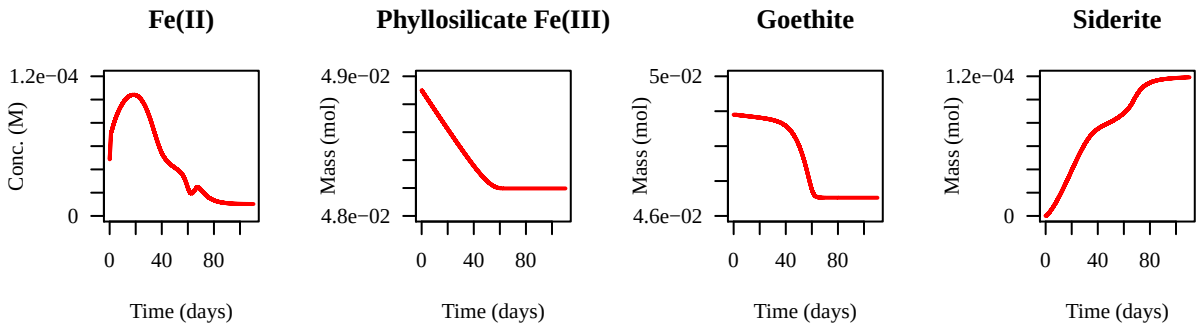

Figure 4.3: From the left, concentration vs. time plots for aqueous ferric iron ($Fe^{+2}_{(aq)}$), phyllosilicate ferrous iron ($Fe(III)_{(ls)}$), goethite ($FeOOH_{(s)}$), siderite ($FeCO_{3(s)}$).

reduction rate during the time when sulfate reduction dominates the consumption of acetate.

Mass of ferrous iron housed in goethite is dependent on iron reduction and dissolution via HS^-. Prior to $t \approx 40$ days, reduction of ferrous iron in goethite is nearly constant. Once sulfate reduction becomes dominant near $t = 40$ days, the mass of goethite sharply decreases to its steady state concentration. The increase in goethite mass loss is a result of increased formation of elemental sulfur previously discussed until acetate is completely consumed.

Ferric iron introduction into solution facilitates siderite $FeCO_{3(s)}$ and mackinawite $FeS_{(s)}$ precipitation. FeS formation is primarily driven by availability of HS^- and a result becomes significant during sulfate reducing conditions. Siderite precipitation is more dependent on aqueous ferric iron concentrations and therefore exhibits a different formation with time compared to mackinawite. Siderite precipitation occurs at an increasing rate until the onset of sulfate reducing conditions near $t = 40$ days, where aqueous iron forms mackinawite, slowing down the rate of siderite precipitation between the $t = 40$ days and $t = 60$ days time period. Once acetate is completely consumed near $t = 60$ days, the rate of siderite precipitation increases because a decreasing amount of ferric iron is used in the precipitation of mackinawite driven by the plummeting concentration of HS^-. All HS^- present when the acetate runs out forms mackinawite or elemental sulfur. The formation of elemental sulfur reduces ferrous iron from goethite which introduces more ferric iron into solution.

Mackinawite and elemental sulfur reach steady state once the concentration of HS^- decreases to zero very shortly after $t = 60$ days, but ferric iron produced from the formation of elemental sulfur facilitates the precipitation of siderite at a decreasing rate from $t = 60$ days on reaching a near steady state mass near $t = 100$ days.

The concentration of aqueous ferric iron relies on all of the previously described processes. During pre-sulfate reducing conditions $t < 40$ days, iron reduction dominates and introduces ferric iron into solution at a decreasing rate. The rate of aqueous ferric iron introduction into solution is initially very high due to the lack competition for acetate with SRB. Once the system becomes dominated by sulfate reducing conditions near $t = 40$ days, ferric iron peaks and then decreases at an increasing rate due to mackinawite formation. The rate of removal of ferric iron from solution due to the formation of mackinawite is constant for a short time period within the period when sulfate reduction dominates until the rate of acetate consumption begins to decrease near the point where it is completely consumed. Once acetate is completely consumed HS^- concentrations plummet to zero forming elemental sulfur and mackinawite with remaining HS^-, which is a net producer of ferric iron because the rate of elemental sulfur precipitation is greater than that of mackinawite formation. The oxidation of residual HS^- to elemental sulfur introduces additional ferric iron into solution, which is shown as the local maximum of aqueous ferric iron shortly after $t = 60$ days. Following the local maximum of aqueous ferric iron, siderite precipitate continues and drives aqueous ferric iron to decrease at a decreasing rate to its near steady state value.

4.1.4 Uranium System

Uranium is present at the Naturita site in aqueous uranyl (${UO_2}^{+2}{}_{(aq)}$) species presented in Table 3.2 and in adsorbed uranyl (>${UO_2}^{+2}$) species presented in Table 3.5 in Section 3.1 of Chapter 3. Throughout the batch simulation, iron-reducing microbes reduce ambient ${UO_2}^{+2}{}_{(aq)}$ to solid-phase uraninite ($UO_{2(s)}$).

Figure 4.4 shows the concentrations of aqueous ${UO_2}^{+2}$ species, the total mass of adsorbed uranium (<${UO_2}^{+2}$) and the total mass of solid-phase uraninite ($UO_{2(s)}$). During the batch sim-

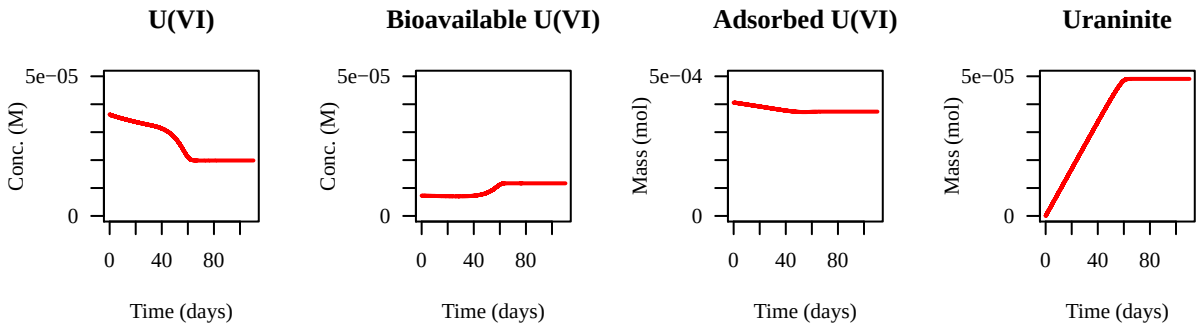

Figure 4.4: From the left, concentration with time of aqueous U(VI) ($UO_2{}^{+2}{}_{(aq)}$), aqueous bioavailable U(VI) ($UO_2{}^{+2}{}_{avail.}$), total adsorbed mass of uranium ($>UO_2{}^{+2}$) and mass of solid-phase uraninite ($UO_{2(s)}$) with time during the batch simulation.

ulation, the concentration of aqueous uranium generally decreases at two different rates. During iron reducing conditions prior to $t \approx 40$ days, uranium is reduced at a lower rate compared to the reduction rate during sulfate reducing conditions. Once sulfate reducing conditions take off after $t = 40$ days, increasing amounts of bicarbonate are added supersaturating the solution and precipitating calcite ($CaCO_{3(s)}$) as showing in Figure 4.1. Calcite precipitation removes ambient Ca^{+2}, which is a constituent for the two thermodynamically unavailable uranyl-containing species: $CaUO_2(CO_3)_3{}^{-2}{}_{(aq)}$ and $Ca_2UO_2(CO_3)_{3(aq)}$. Along with the aqueous uranyl concentration, the concentration of thermodynamically available aqueous uranyl [$UO_2{}^{+2}{}_{avail.}$] used in the rate equation for aqueous uranyl reduction is shown in Figure 4.4 as bioavailable $UO_2{}^{+2}{}_{(s)}$. At $t \approx 40$ days, the concentration of $UO_2{}^{+2}{}_{avail.}$ increases due to calcite formation, which increases the removal rate of uranyl from solution until the acetate has been completely consumed near $t = 60$ days. All aqueous uranium mass removed from solution was reductively transformed into solid-phase uraninite as $UO_{2(s)}$. The mass of uraninite increases at a constant, nearly linear rate during the period prior to complete consumption of acetate.

The adsorbed mass of uranium ($>UO_2{}^{+2}$) decreases linearly during the period prior to complete acetate consumption. Decreases in aqueous uranium, coupled with increasing bicarbonate

concentrations, and pH from acetate oxidation during TEAPs contribute to general desorption of uranium.

4.2 1D Transport Simulations

Building from chemical dynamics observed in batch simulations, 1D transport simulations provide insight into how biogeochemical processes occur as aqueous species are transported through a linear column of sediment.

Plots presented in this section show the distribution of species along the column at $t = 0$ days, $t = 30$ days and when the system reaches steady state at $t = t_{ss} = 390$ days. The treatment solution consists of different concentrations of constituents than that present in the plume of contaminated groundwater. A "blank" simulation was ran where no acetate was injected into the column to observe how concentrations evolve as the treatment chemical travels through the column. Then, an "active" simulation with acetate present in the treatment solution injected at the upstream boundary was run. Differences in these simulations show the amount of mass of each constituent presented that is gained or lost due to microbially-induced reactions, which will then motivate the final section of this chapter where the results of the field-scale pumping schemes are presented.

4.2.1 Carbon System

To track the mass of acetate reacted during the column simulation, an inert tracer was introduced into the treatment solution at the same concentration as acetate introduced into the treatment solution. Differences in concentrations presented in the column between acetate and the tracer result from the microbial consumption of acetate. Generally the mass of acetate consumed in the column is much smaller than in the batch simulations showing lower microbial activity. Figure 4.5 shows concentrations of acetate and carbonate and mass of calcite with column length at $t = 0$ days, $t = 30$ days, $t = 390$ days. At $t = 0$ days, no acetate is present in the column. At $t = 30$ days, the treatment solution has not yet engulfed the entire column showing higher acetate concentrations at the upstream boundary where the treatment solution is introduced and lower concentrations at

the downstream end. When the system reaches steady state, acetate is present in the entire column at the concentration of acetate presented in the treatment solution. The differences between the inert tracer and the acetate concentration are minor but present, showing significant, but small, consumption of acetate. At steady state, the difference between acetate and the inert tracer in the column increases with distance from the upstream column boundary. This difference shows consumption of acetate as treatment solution flows through the column.

Along with acetate concentrations, Figure 4.5 presents carbonate concentrations at $t = 0$ days, $t = 30$ days, and $t = 390$ days. Carbonate concentrations decrease over the duration of the column simulation primarily due to lower carbonate concentrations in the treatment solution compared to that present in the aquifer from process wastewater leached into the underlying aquifer at the Naturita site. Deviations between the blank and active simulation are due to carbonate precipitation with ferric iron (Fe^{+2}) in the formation of the siderite mineral throughout the duration of the column simulation. At steady state, the difference between carbonate concentrations with distance in the blank and active simulation is small, but significant. Microbial activity introduces ferric iron (Fe^{+2}) into solution from iron reduction (further discussed in Section 4.1.3) which precipitates with aqueous carbonate to form the siderite mineral $FeCO_{3(s)}$. Iron reduction is not active in the blank simulation and therefore less ferric iron is introduced into the system resulting in less siderite formation leaving more aqueous carbonate in solution.

Calcite precipitation/dissolution is negligible as evident by constant mass with column distance for all plot times shown in Figure 4.5.

4.2.2 Sulfur System

Reduced microbial activity limits hydrogen sulfide (HS^-) production which limits the formation of the mackinawite mineral ($FeS_{(s)}$). Figure 4.6 presents the concentrations of aqueous sulfate ($SO_4{}^{+2}$) and hydrogen sulfide (HS^-) and mass of the mackinawite mineral with column length at $t = 0$ days, $t = 30$ days, $t = 390$ days. As with carbonate, sulfate present in the contaminant plume is elevated relative to the treatment solution. At $t = 30$ days, the treatment solution has not yet

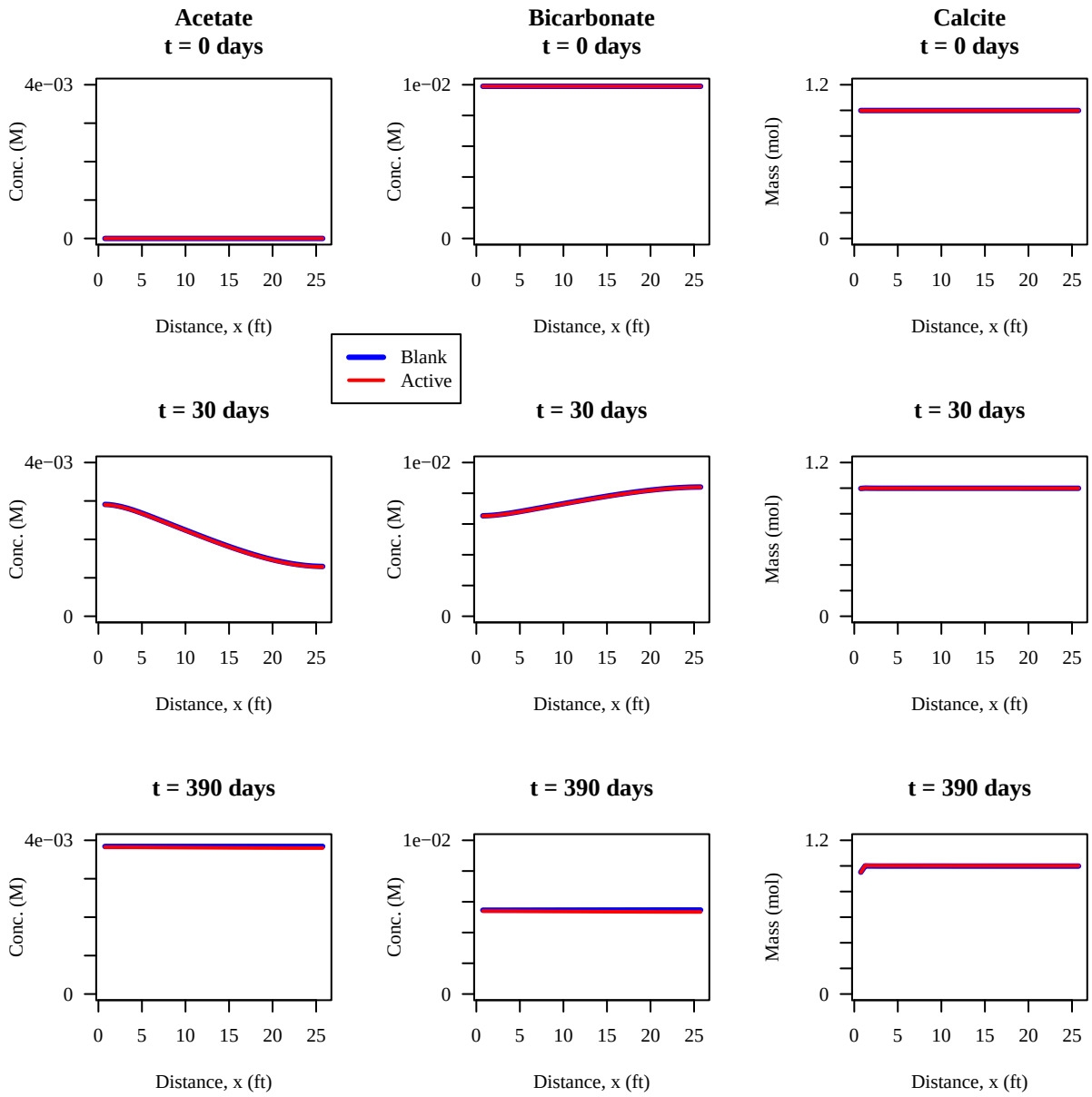

Figure 4.5: By row, concentrations of acetate (CH_3COO^-), carbonate ($CO_3{}^{-2}$), and mass of calcite ($CaCO_{3(s)}$) with column distance for the blank and active simulations for $t = 0,\ 30\ t_{ss}$ days are shown in red. The inert tracer is shown in blue behind the acetate concentrations. The concentration of carbonate and mass calcite in the blank simulations are shown in blue.

engulfed the column, so the concentration of sulfate at the upstream boundary is lower than that at the upstream boundary and is a general S-shaped curve in the central portion of the column. At steady state, the sulfate concentration is that present in the treatment solution.

Sulfide (most prevalent as hydrogen sulfide HS^-) forms as a result of microbial reduction of aqueous sulfate. In the blank simulation, no microbial activity is present due to the lack of acetate and therefore no sulfide forms. This causes no formation of sulfide and or mackinawite (formed from HS^-) in the blank simulation. However, in the active simulation when microbial activity is active, sulfate reduction occurs producing aqueous sulfide. Aqueous sulfide, along with ferric iron (Fe^{+2}) precipitates as the mackinawite mineral $FeS_{(s)}$. Although microbial activity contributes to the formation of sulfide, sulfide concentrations are two orders of magnitude smaller in the column simulation than those present in the batch simulation.

The distributions of sulfide in the column during the column simulation are primarily driven by the precipitation of mackinawite. Mackinawite precipitation is driven mostly by the aqueous ferric iron concentration. As shown in Figure 4.7, the concentration of ferric iron along the column length generally increases with column length as does the mass of precipitated mackinawite. Aqueous sulfide is inversely related to the mass of mackinawite, so because there is a smaller mass of mackinawite in the upstream portion of the column, there is more aqueous sulfide. Mackinawite precipitation generally increases with column distance in the steady state distribution resulting in a general decrease of sulfide concentration with column distance at steady state.

Elemental sulfur ($S^0_{(s)}$) precipitates through the reductive dissolution of goethite (FeOOH) promoted by HS^-. Sulfide concentration peaks near the upstream boundary at $t = 30$ days, which promotes the reductive dissolution of goethite as evident by the elemental sulfur peak near the same distance downstream as the sulfide peak $x \approx 5$ ft. As sulfide concentrations increase during the column simulation so does the formation of elemental sulfur. The mass of sulfur peaks near the upstream boundary and then decreases at a decreasing rate toward the downstream boundary due to competition with mackinawite for sulfide. Because aqueous ferric iron $Fe^{+2}_{(aq)}$ concentrations generally increase (shown in Figure 4.7) downstream promoting the preferential precipitation of

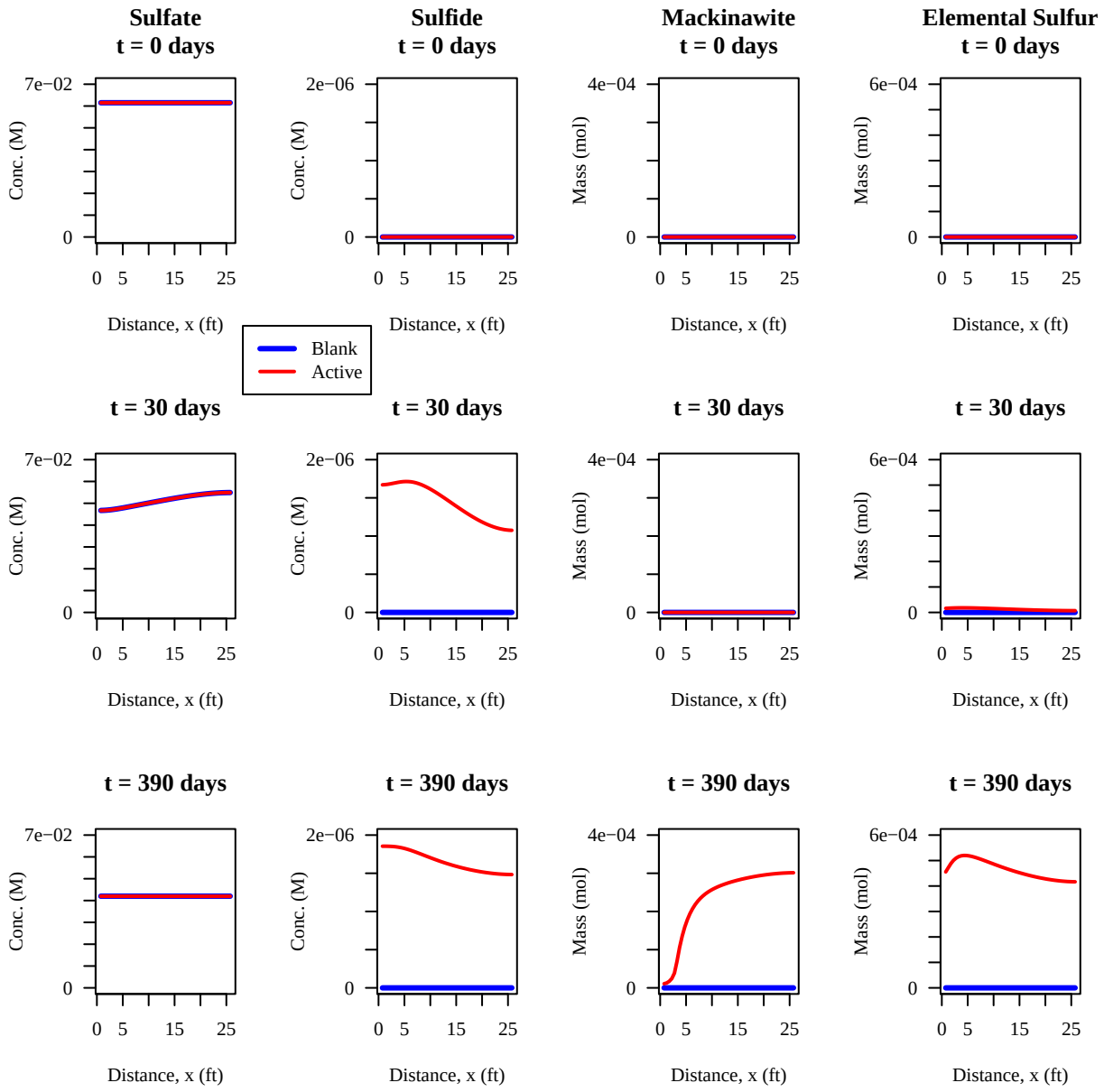

Figure 4.6: By row, concentrations of sulfate ($SO_4{}^{-2}$), sulfide (HS^-), and mass of mackinawite ($FeS_{(s)}$) and elemental sulfur $S^0_{(s)}$ with column distance for the blank and active simulations for $t = 0$ days, $t = 30$ days, $t = 390$ days are shown in red. The concentrations of sulfate and sulfide and mass mackinawite and elemental sulfur in the blank simulations are shown in blue.

mackinawite over elemental sulfur.

4.2.3 Iron System

The majority of iron relevant to uranium bioremediation is present in siderite ($FeCO_{3(s)}$), goethite ($FeOOH_{(s)}$) and housed in layer-silicate (phyllosilicate) minerals represented by $Fe(III)_{(ls)}$. Iron reduction sources iron from these minerals and dissolves into solution as ferric iron (Fe^{+2}). Figure 4.7 shows the concentration of aqueous ferric iron Fe^{+2}, and the mass of siderite, goethite, and phyllosilicate ferrous (Fe(III)) iron for the blank and active simulations at $t = 0$ days, $t = 30$ days, $t = 390$ days. These iron species change due to iron reduction promoted by microbial activity, and are therefore generally constant during the blank simulation. The only exception is the precipitation of siderite ($FeCO_{3(s)}$) due to supersaturation of the initial solution with respect to these species.

In the active simulation, aqueous concentrations of ferric iron are influenced by the concentration of ferric iron in the treatment solution which is shown at the upstream boundary by the blank line. At $t = 30$ days, little goethite is used in by iron-reducing bacteria as evidence by its general tracking with the blank value. However phyllosilicate ferrous iron reduction is occurring near near the upstream boundary as the active simulation mass distribution of phyllosilicate iron deviates from the blank mass distribution near the upstream boundary. This results in the peak of aqueous ferric iron near $x \approx 10$ ft. Downstream of the peak, siderite precipitation precipitates ferric iron from solution contributing to its general concentration decrease along the length of the column. At $t = 30$ days, elevated acetate concentrations have not yet advected through the column and promote iron reduction, which can also explain the peak near $x = 10$ ft.

At steady state, the upstream aqueous ferric iron concentration is still influenced by the treatment solution at the upstream boundary. With increasing distance downstream in the column, increased ferric iron concentration exists due to microbially promoted reduction of iron present in goethite and phyllosilicate minerals. The distribution of siderite mass is primarily influenced by the distribution of aqueous ferric iron – with increased aqueous ferric iron with increasing distance

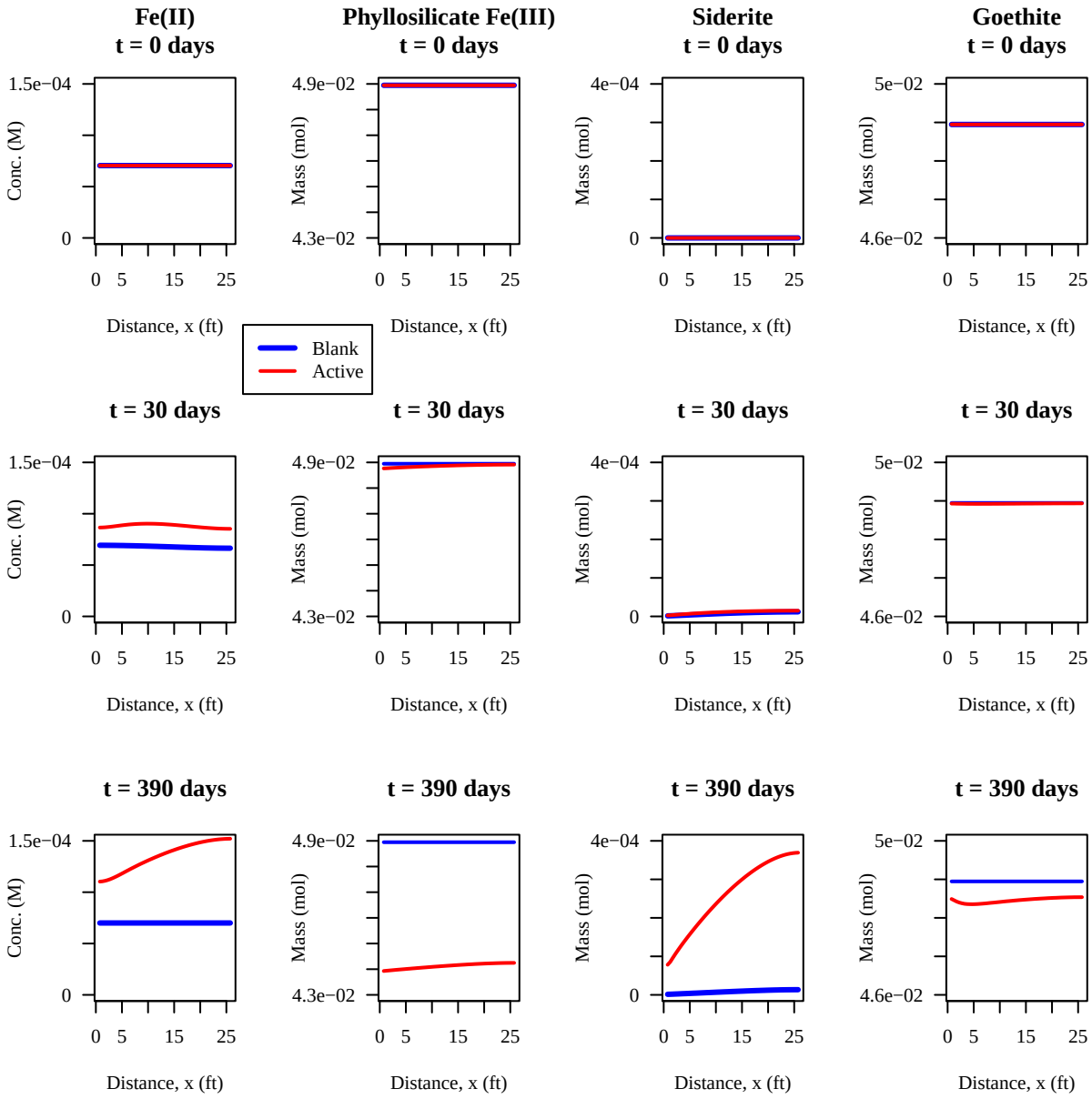

Figure 4.7: By row, concentrations of aqueous ferric iron ($Fe^{+2}_{(aq)}$), mass of siderite ($FeCO_{3(s)}$), goethite ($FeOOH_{(s)}$), and phyllosilicate ferrous iron ($Fe(III)_{(ls)}$) with column distance for the blank and active simulations for $t = 0$ days, $t = 30$ days, $t = 390$ days are shown in red. The concentrations of aqueous ferric iron and mass of siderite, goethite, and phyllosilicate ferrous iron in the blank simulations are shown in blue.

downstream, the mass of siderite precipitated also increases. The distribution of goethite through the column is influenced mostly by sulfide-promoted dissolution of goethite, which can be tracked by the distribution of elemental sulfur. As the mass of elemental sulfur peaks near the upstream boundary, the mass of goethite has its minimum value. Phyllosilicate ferrous iron significantly decreases between $t = 30$ days and $t = 390$ days, but generally has the same distribution throughout the column. Increased phyllosilicate iron is reduced by microbes at the upstream boundary due to increase acetate concentrations from fresh treatment solution introduced at the upstream boundary.

Aqueous ferric iron initially decreases due to the precipitation of the siderite mineral $FeCO_{3(s)}$ due to elevated carbonate concentrations present in the plume as shown in Figure 4.7. This occurs for a few days until the concentration of acetate increases at the end of the column from the step input of treatment solution. Acetate drives iron reducing microbial activity to increase as evident by the decreasing mass of the goethite mineral (FeOOH) and phyllosilicate ferric iron ($Fe(III)_{(ls)}$) during the simulation. As a result of these microbial processes, aqueous ferric iron is introduced into the system and trends toward a steady state solution toward the end of the simulation. Siderite formation through the experiment occurs at a constant rate throughout the simulation.

4.2.4 Uranium System

Uranium present in the plume of contaminated groundwater exists in aqueous uranyl complexes ${UO_2}^{+2}{}_{(aq)}$ and adsorbed the aquifer media ($>{UO_2}^{+2}$). Figure 4.8 shows the concentration of uranyl, mass of adsorbed uranyl and biotransformed uraninite ($UO_{2(s)}$) at $t = 0$ days, $t = 30$ days, $t = 390$ days. The treatment solution has a concentration of uranium three orders of magnitude lower than that initially present in the contaminant plume. At $t = 30$ days, the influence of the low level of uranium in the treatment solution becomes evident as the concentration of aqueous uranyl sharply decreases moving upstream from its initial concentration present in the contaminant plume. At steady state, the uranium concentration is that present in the treatment solution throughout the column. The deviation from the blank simulation is evidence of microbially promoted reduction of uranyl during the column simulation. If there were no uranium biotransformation occurring during

the column test, the distribution of uranyl in the active simulation would match that present in the blank simulation. Deviation of the distribution of aqueous uranyl in the active simulation from that present in the blank simulation shows that aqueous uranium is converted to solid phase uraninite during the column simulation.

Uranium adsorbed to aquifer media initially is mobilized due to decreased aqueous uranyl concentrations. Uranyl concentrations in the column decrease steadily due to the treatment solution advecting through the column. As uranyl concentrations decrease, equilibrium of all surface species is disturbed and uranium is removed from the adsorbed phase to attempt to re-equilibrate the system. Fortunately, some of the mass of previously adsorbed uranium is transformed into solid-phase uraninite. The deviation of the distribution of adsorbed uranium within the column is primarily influenced by the deviation of aqueous uranyl. With decreased aqueous uranyl concentrations throughout the column present in the active simulation compared to the blank, increased removal of uranyl from the adsorbed phase occurs resulting in a near-complete removal of uranyl from the adsorbed phase. The distribution of bioavailable uranium generally tracks with the distribution of aqueous uranyl throughout the simulation. In contrast to the batch simulation, calcite precipitation is negligible and therefore does not affect the amount of aqueous uranium available for microbial processes.

Less than half of the uranyl present in the aquifer as aqueous or adsorbed uranyl is transformed into solid-phase uraninite, with the rest of the uranium mass flushed out of the downstream end of the column by treatment chemical advection. Compared to the 85% of initial uranium mass present in the batch simulation converted to uraninite in the batch simulation, the column experiment percentage removal could be improved. If the mass lost out of the end of the column could be retained in the column for use in microbial processes, increased transformation to aqueous uranyl can occur. Moving to field-scale, dynamic flow fields introduced by EIE may be able to contain mobilized uranium initially present in the contaminant plume for use in microbial metabolism.

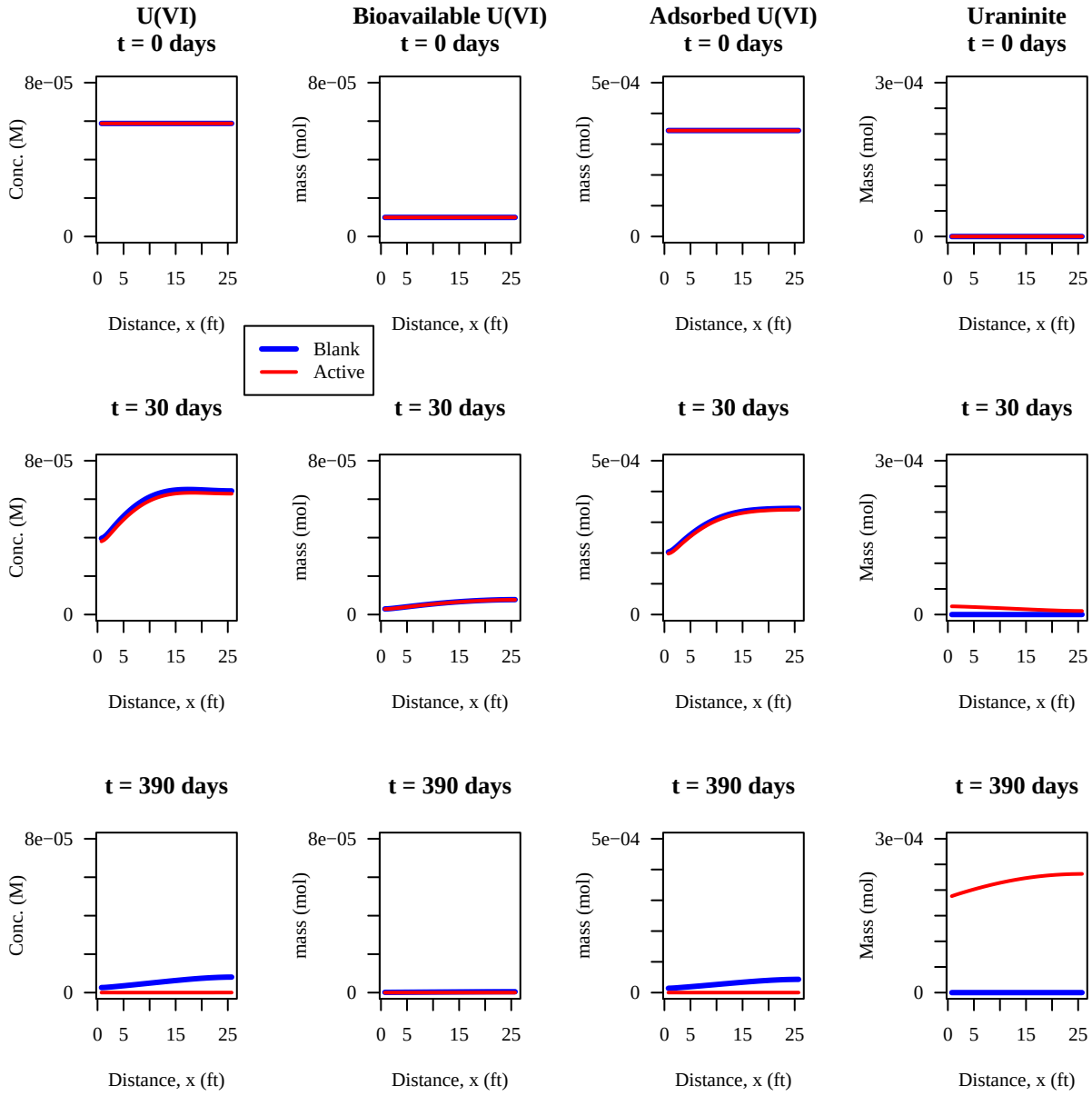

Figure 4.8: By row, concentrations of aqueous U(VI) ($UO_2^{+2}{}_{(aq)}$), aqueous bioavailable U(VI) ($UO_2^{+2}{}_{avail.}$), total adsorbed mass of uranium ($>UO_2^{+2}$) and mass of solid-phase uraninite ($UO_{2(s)}$) with column distance for the blank and active simulations for $t = 0$ days, $t = 30$ days, $t = 390$ days are shown in red. The concentrations of aqueous ferric iron and mass of siderite, goethite, and phyllosilicate ferrous iron in the blank simulations are shown in blue.

4.3 Field-scale Tracer Simulations

To investigate the ability of EIE to spread treatment solution throughout the plume of uranium contaminated groundwater present at the Naturita site, simulations to track a tracer chemical throughout the remediation period was conducted for the two EIE sequences and the three-well injection gallery system. Tracking the spatial distribution and concentration of a tracer chemical throughout the remediation period provides insight into the spatial distribution and concentrations of tracer resulting from pumping associated with each remediation system investigated. Removal of uranium from groundwater is highly dependent on the amount of acetate in the vicinity of aqueous uranium to allow microbes to promote transformation of aqueous uranium to solid-phase uraninite. When acetate is present at higher concentrations, more uranium can be transformed by microbes, so the goal of the tracer simulations is to investigate which system promotes the highest tracer concentration at the end of the $t = 390$ day remediation period. The tracer is used as a surrogate chemical to track the fate of acetate in the aquifer when the full biogeochemical reaction framework is included in the model. The field-scale model was used to track regional transport of the uranium-contaminated groundwater plume over the entire site, not for investigation of area-specific remediation occurring on site. Due to low resolution discretization of the grid present in the field-scale model, mixing can be severely over predicted, so grid refinement will need to occur before meaningful field-scale model results including the full reaction framework can be produced.

Figure 4.9 shows the distribution of the tracer chemical at the end of the $t = 390$ day remediation period for the three-well injection gallery system and EIE sequence 1 and EIE sequence 2 as presented in Table 3.10. In this investigation, the most effective remediation system will promote the smallest amount of attenuation of the injected acetate (modeled by an inert tracer) measured by the maximum concentration of the tracer present in the aquifer at the end of the remediation period.

The three-well injection gallery promotes the lowest peak concentration of acetate ($C_{max} = 1.48 \times 10^{-4}$ M) within the aquifer after the remediation period of the three tested. This is primarily

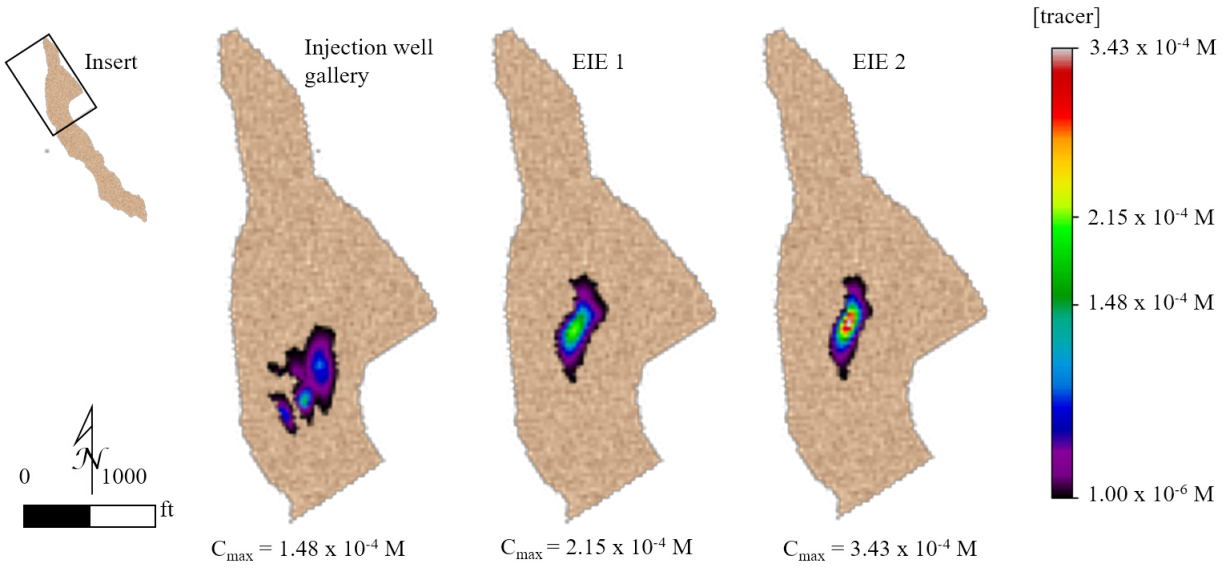

Figure 4.9: Final concentration and final distribution of the tracer for each of the remediation systems investigated. The respective maximum concentration of tracer present in of each systems is listed under each of the plots and shown on the colobar.

due nature at which these systems are built. Injection gallery systems are designed to introduce a treatment solution to be spread throughout the contaminant plume via ambient groundwater flow. Dispersion is extremely high at the Naturita site [44] and this contributes to the attenuation of the acetate plume created by the three-well injection system. With lower concentrations of tracer (acetate) present in the aquifer, lower transformation of uranium present in the contaminant plume can be expected.

Employing EIE sequence 1 (Table 3.10) nearly doubles the maximum concentration of acetate present in the aquifer ($C_{max} = 2.15 \times 10^{-4}$ M) at the end of the remediation time. Wells surrounding the plume combat the spreading of the tracer plume from the injection well. Through EIE, the trace plume is less able to disperse throughout the aquifer due to the containment provided by dynamic flow fields created by the first EIE sequence. The development of this sequence in Mays and Neupauer [105] was done in the absence of ambient flow and thus the employment of the west and east wells in the first six EIE steps was somewhat arbitrary. In this case, the employment of those wells contributes to containing the transverse dispersion, but allows for the tracer plume to disperse in the direction parallel to flow until the north and south wells are employed in the second half of the sequence. However, by this time, ambient groundwater flow has contributed to increased dispersion and subsequent attenuation of the tracer plume. Albeit and improvement from the three-well injection gallery, employing the north and south wells in the first six steps of the sequence further combats attenuation due to high dispersion present at the Naturita site.

In EIE sequence 2, the north and south wells are employed in the first six steps of the sequence followed by the employment of the east and west wells in the second half of the sequence. The change in general well employment order facilitates a peak concentration of acetate present in the aquifer at the end of the remediation period ($C_{max} = 3.43 \times 10^{-4}$ M) nearly three times that promoted by the three-well injection gallery and a significant improvement from the first EIE sequence employed. As discussed previously, the north and south wells are oriented parallel to ambient flow relative to the injection well at the center of the five-well diamond well pattern. By employing the north and south wells in the first six steps of the EIE sequence, attenuation due

to longitudinal dispersion in the direction of ambient groundwater flow is reduced relative to the previous two remediation systems.

Chapter 5

Conclusions and Future Work

5.1 Conclusions

This work created a reaction network to model *in situ* immobilization of uranium present in the alluvial aquifer present at the Naturita site for use in investigating the ability of Engineered Injection and Extraction (EIE) in a practical remediation scenario. The reaction network developed for this work was largely borrowed from the work done by Yabusaki et al. [180], which provides a benchmark to compared the results from this investigation to. In general batch results match those presented in Yabusaki et al. [180]. The slow consumption of acetate during iron-reducing conditions followed by the rapid consumption of acetate when sulfate reduction dominated the system is matched in this investigation.

During the column simulation, uranium present in aqueous and adsorbed uranyl species was almost completely transformed to solid-phase uraninite or flushed out of the downstream end of the column due to advection of the treatment solution through the column. Although reduction of iron, sulfate and uranium occurred as a result of microbial activity, the extent to which these processes occured in the column study was comparatively less than in the batch simulation, highlighting the need to promote containment of the treatment solution and contaminant allowing the two to react to immobilize uranium.

Through field simulations that track a tracer, EIE provides a solution to this problem by promoting delivery of acetate in the aquifer at elevated concentrations compared to that provided by the three-well injection gallery. The transformation efficiency of uranium vastly decreases from

the batch simulation to the column solution because the treatment solution flushes uranium out of the downstream end of the column. Because the majority of uranium is pushed out of the column by the treatment solution, there is little commingling of the two reactants, therefore decreasing the efficiency of removal of aqueous uranium from groundwater. Through field-simulations tracking a tracer to represent the fate of acetate in the contaminant plume, this investigation has shown that both EIE sequences investigated promote higher final peak concentrations of acetate within the aquifer than that promoted by the three-well injection gallery based on a system employed in field tests at the Old Rifle site. Further, operating wells placed parallel to ambient flow in the aquifer during EIE promotes an increased final peak concentration of the tracer in the aquifer at the end of the remediation period.

5.2 Modeling Accomplishments

5.2.1 Oxidation Reduction

Traditionally, oxidation reduction processes modeled using PHREEQC are done by decoupling the valence states of elements in the model. PHREEQC tracks "Master Species" and subsequent species formed with other Master Species present in the model. The reaction framework from Yabusaki et al. [180] conducted redox relationships by decoupling Sulfide/Sulfate, Ferric/Ferrous Iron and Carbonate/Acetate. Codes developed for the Naturita site model were able to keep redox species coupled with similar geochemical dynamics as presented in Yabusaki et al. [180]. At the batch and 1D transport scale computational differences are somewhat negligible, but at the field scale, coupling redox species under one master species allows the MT3DMS to track both under the umbrella of the elemental master species.

Iron and sulfate were modeled in this way, while carbon/acetate needed two species and a kinetic expression to correctly track the redox potential contribution of acetate in solution. When acetate as C(0) is introduced into the system, it instantly oxidizes into carbonate species leaving none leftover for use in microbial reaction pathways. Acetate is declared as a mobile kinetic

reactant (in transport simulations) and is used in the calculation of microbial reaction rates. The mass of acetate consumed per reaction step is then added as C(0) as CH_3COO^- and immediately consumed by the microbial processes. However, the "flash in the pan" of acetate is recommended by PHREEQC developers to lower the pe of the solution [132]. While this is not a new concept in PHREEQC, it is encouraging to create geochemically complex solutions that correctly model the oxidation reduction potential of the solution. The pe of the solution is important to accurately model because this allows for redox species to exist in the correct redox equilibrium.

For example, ${SO_4}^{-2}$ and HS^- can exist in solution equilibrium because the solution pe is low enough to allow for non negligible species amounts of each species.

5.2.2 Solution Charge Imbalance

Certain modeling frameworks for kinetic, surface, and ion exchange species can create a charge imbalance in solution. In the environment, this is not physically possible and can therefore create problems for transport calculations involving surface complexation reactions modeled without electrostatic potentials developed at surfaces. The concept behind using a surface complexation model instead of modeling electrostatic interactions is that electrostatic interactions and double layer's governing adsorption of solution ions to aquifer media is extremely complex and not easily measured in a lab. On the other hand, adsorption isotherms can be measured in laboratory settings and generalized surface reactions (see Table 3.12) can be fit to model adsorption dynamics under differing geochemical conditions. This provides an easy framework by which to track adsorption and retardation transport of adsorbed species However, when the "-no_edl" identifier is used in PHREEQC calculations (housed in PHREEQC or PHT3D), surface species are treated much like aqueous species mathematically [133]. If the adsorbed surface complexed species is not charge neutral, its formation will impart a charge imbalance in the solution. The surface species is immobile, while ions added to the solution when this occurs transport the charge imbalance. If this charge imbalance gets too large, it can impart errors or cause non-convergence of solution calculations [10]. This problem hindered the development of this model and caused convergence issues in the field

scale model. The culprit was an iron surface complexation model included in the general reaction framework from Yabusaki et al. [180]. The surface model was removed and tested for its affect on geochemical dynamics, which was negliglible. Surface species were part of the reaction rate for goethite $FeOOH_{(s)}$ reduction. The value included in the calculation remained near the amount of initial adsorbent sites, so that value was used in this investigation, as presented in Table 3.7.

The removal of the iron surface complexation model lowered the charge imbalance making the model calculations less likely to diverge. However, all of the surface species included in the reaction framework for this investigation are charged and therefore will impact charge imbalances in solution as these species are formed and dissociate. Another source of charge imbalance is the kinetic reaction for biological reduction of phyllosilicate ferrous iron ($Fe(III)_{(ls)}$) as the equation is charge imbalanced, so any forward progress in that equation will impart additional positive charge in solution. A significant effort was made to re-calibrate the surface complexation model with charge-neutral surface complexed uranium species. This task was abandoned due to high residuals and the calibration was conducted by trying to match simulated adsorption chemical distributions in solutions with varying pCO_2 and pH as done during the development of the surface complexation model used in this study. The original surface complexation model was calibrated to laboratory data.

5.3 Future Work

This investigation was another step towards developing the engineered injection and extraction (EIE) framework for employment in field remediation scenarios. Previous investigations have explored comparatively simple reaction frameworks to that of uranium. By employing a semi-synthetic model based on physical conditions based on two well characterized uranium contaminated sites, EIE was tested deterministically for its comparative ability to remediate an aquifer with uranium-contaminated groundwater over methods previously employed at contaminated sites. There are many limitations and uncertainties involved with conducting deterministic comparisons as done in this study. It is quite possible that the parameters related to the the EIE sequence –

pumping sequence, pumping rates, well locations, treatment solution injection location, treatment solution constituents, etc. – could have been near optimal while parameters related to the design of the three-well injection gallery system may have been further from optimal. Optimal refers to a set of design parameters that collectively facilitate the highest amount of degradation possible at the Naturita site. This uncertainty creates the need to employ an optimization algorithm to find this set of optimal parameters for both systems. Comparing the two systems that operate at the highest amount of uranium immobilization possible will provide deeper insight into the comparative advantage of lack thereof of the EIE remediation framework.

The model grid was far too coarse to model interactions of wells less than a few hundred feet apart. The model was originally set up to model regional transport of uranium on the site – not for tracking hydrologic response to pumping. Large grid cells also inherently over-predict subsurface mixing resulting inflated reaction. Realistically species 25 feet apart would not be in close enough proximity to react. As a result, grid refinement needs to occur before any robust conclusions can be drawn from this model.

The semi-synthetic (codes developed from multiple sites) provides a valid starting point to evaluate EIE on geochemically complex systems, but field work involving bioremediation or EIE could inform this model to better predict dynamics occurring at the site.

In terms of EIE, many new research questions have developed from this work. The creation of treatment solution presents an interesting problem in this context. Until now, treatment solution has been assumed to contain water and a treatment chemical and water used during EIE steps has been considered pure to this point. As in the field-scale investigation conducted by Long et al. [99], groundwater harvested from upgradient of the contaminant plume served as the basis for treatment solution and served as water used for injection steps. Because of the complex interactions with uranium and other geochemically relevant species, the quality of this water may enhance or inhibit widespread uranium immobilization.

This system is based off of physical conditions existing at the Naturita site and thus has finite pumping/recharge capacity. The model was built as a steady state model and has not been

calibrated for transient specific flow parameters, so the model should be recalibrated The model also consists of three layers, so the distribution of flow and well screen depths should be investigated.

The reaction framework in this investigation only models part of the complexity of uranium biogeochemical dynamics occurring in nature – many of which are still largely uncharacterized. The framework present in this investigation models biogeochemical dynamics governing the biotic transformation of aqueous U(VI) to solid-phase U(IV). However, it has been well documented that U(VI) interacts with minerals that also provide reducing agents to facilitate the reduction of U(VI) to U(IV). Singer et al. [157] and Latta et al. [91] found that magnetite with high Fe(III)/Fe(II) fractions can promote abiotic reduction of U(VI) to U(IV) using Fe(III) housed in magnetite as the reducing agent. Iron sulfide minerals – mackinawite ($FeS_{(s)}$) and pyrite ($FeS_{2(s)}$) – have also been well documented to have complex interactions with aqueous U(VI) and contribute to the reduction of U(VI). To make this model more robust, these reaction pathways for U(VI) conversion to U(IV) need to characterized and included in this model.

This investigation ends after U(VI) has been removed from solution and does not model any re-oxidation of biogenic U(IV) and subsequent re-mobilization of uranium. It has been well documented that U(IV) is readily able to be remobilized following the complete consumption of an introduced electron donor by oxidizing groundwater. In fact, Bargar et al. [14] found that two groups of solid-phase U(IV) species form as a result of bioremediation. A field-scale model encompassing both groups of solid-phase U(IV) species formed as a result of bioremediation has yet to be constructed.

Bibliography

[1] A. Abdelouas, Y. Lu, W. Lutz, and H. E. Nuttall. Reduction of U(VI) to U(IV) by indigenous bacteria in contaminated ground water. Journal of Contaminant Hydrology, 35(1 – 3):217 – 233, 1998.

[2] A. Abdelouas, W. Lutze, and E. Nuttall. Chemical reactions of uranium in ground water at mill tailings site. Journal of Contaminant Hydrology, 34(4):343 – 361, 1998.

[3] A. Abdelouas, W. Lutze, and H. E. Nuttall. Oxidative dissolution of uraninite precipitated on navajo sandstone. Journal of Contaminant Hydrology, 36:353 – 375, 1999.

[4] S. S. Adams and R. T. Cramer. Data-process-criteria model for roll-type uranium deposits. In Geological Environments of Sandstone-Type Uranium Deposits. International Atomic Energy Agency, 1985.

[5] United States Energy Information Administration. Uranium mill sites under the UMTRA project. online.

[6] D. S. Alessi, J. S. Lezama-Pacheco, N. Janot, E. I. Suvorova, J. M. Cerrato, D. E. Giammar, J. A. Davis, P. M. Fox, K. H. Williams, P. E. Long, K. M Handley, R. Bernier-Latmani, and J. R. Bargar. Speciation and reactivity and uranium products formed during in situ bioremediation in a shallow alluvial aquifer. Environmental Science & Technology, 48:12841 – 12850, 2014.

[7] S. Amaryi, T. Reich, T. Arnold, G. Geipel, and G. Bernhard. Spectroscopic characterizations of alkaline earth uranyl carboates. Solid State Chemistry, 178:567 – 577, 2005.

[8] M. P. Anderson, W. W. Woessner, and R. J. Hunt. Applied Groundwater Modeling: Simulation of Flow and Advective Transport. Elsivier, 2015.

[9] R. T. Anderson, H. A. Vrionis, I. Ortiz-Bernad, C. T. Resch, P. E. Long, R. Dayvault, K. Karp, S. Marutzky, D. R. Metzler, A. Peacock, D. C. White, M. Lowe, and D. R. Lovley. Stimulating the in situ activity *geobacter* species to remove uranium from the groundwater of a uranium-contaminated aquifer. Applied and Environmental Microbiology, 69(10):5884 – 5891, 2003.

[10] C. A. J. Appelo and M. Rolle. PHT3D: A reactive multicomponent transport model for saturated porous media. Groud Water Software Spotlight.

[11] World Nuclear Association. Geology of uranium deposits. online, 2015.

[12] A. C. Bagtzoglou and P. M. Oates. Chaotic advection and enhanced groundwater remediation. Journal of Materials in Civil Engineering, 19(1):75 – 83, 2007.

[13] J. R. Bargar, R. Bernier-Latmani, D. E. Giammar, and B. M. Tebo. Biogenic uraninite nanoparticles and their importance for uranium remediation. Elements, 4(6):407 – 412, 2008.

[14] J. R. Bargar, K. H. Williams, K. M. Campbell, P. E. Long, J. E. Stubbs, E. I. Suvorova, J. S. Lezama-Pacheco, D. S. Alessi, M. Stylo, S. M. Webb, J. A. Davis, D. E. Giammar, L. Y. Blue, and R. Bernier-Latmani. Uranium redox transition pathways in acetate-amended sediments. Proceedings of the National Academy of Sciences, 110(12):4506 – 4511, 2013.

[15] M. Barlett, K. Zhuang, R. Mahadevan, and D. Lovley. Integrative analysis of *geobacter spp.* and sulfate-reducing bacteria during uranium bioremediation. Biogeosciences, 9(3):1033 – 1040, 2012.

[16] H. R. Beller. Anaerobic, nitrate-dependent oxidation of U(IV) oxide minerals by the chemolithoautotrophic bacterium *thiobacillus denitrificans*. Applied Environmental Microbiology, 71(4):2170 – 2174, 2005.

[17] H. R. Beller, T. C. Legler, F. Bourguet, T. E. Letain, S. R. Kane, and M. A. Coleman. Identification of c-type cytochromes involved in anaerobic, bacterial U(IV) oxidation. Biodegradation, 20(1):45 – 53, 2009.

[18] R. Bencheikh-Latmani and J. O. Leckie. Association of uranyl with the cell wall of *pseudomonas fluorescens* inhibits metabolism. Geochimica et Cosmochimica Acta, 67(21):4057 – 4066, 2003.

[19] R. Bernier-Latmani, H. Veeramani, E. D. Vecchia, P. Junier, J. S. Lezama-Pacheco, E. I. Suvorova, J. O. Sharp, N. S. Wigginton, and J. R. Bargar. Non-uraninite products of microbial U(VI) reduction. Environmental Science & Technology, 44:9456 – 9462, 2010.

[20] B. Beyenal, R. K. Sani, B. M. Peyton, A. C. Dohnalkova, J. E. Amonette, and Z. Lewandowski. Uranium immobilization by sulfate-reducing biofilms. Environmental Science & Technology, 38:2067 – 2074, 2004.

[21] Y. Bi and K. F. Hayes. Nano-FeS inhibits UO_2 reoxidation under varied oxic conditions. Environmental Science & Technology, 48(1):632 – 640, 2013.

[22] Y. Bi and K. F. Hayes. Surface passivation limited UO_2 oxidative dissolution in the presence of FeS. Environmental Science & Technology, 48(22):13402 – 13411, 2014.

[23] Y. Bi, S. P. Hyun, R. K. Kukkadapu, and K. F. Hayes. Oxidative dissolution of UO_2 in a simulated groundwater containing synthetic nanocrystalline mackinawite. Geochimica et Cosmochimica Acta, 102:175 – 190, 2013.

[24] Y. Bi, M. Stylo, R. Bernier-Latmani, and K. F. Hayes. Rapid mobilization of nanocrystalline U(IV) coupled with FeS oxidation. Environmental Science & Technology, 50:1403 – 1411, 2015.

[25] S. E. Bone, J. J. Dynes, J. Cliff, and J. R. Bargar. Uranium(IV) adsorption by natural organic matter in anoxic sediments. Proceedings of the Natural Academy of Sciences, 114(4):711 – 716, 2017.

[26] T. Le Borgne, M. Dentz, D. Bolster, J. Carrera, J. R. deDreuzy, and P. Dazy. Non-fickian mixing: Temporal evolution of the scalar dissipation rate in heterogeneous porous media. Advances in Water Resources, 33(12):1468–1475, 2010.

[27] M. I. Boyanov, K. E. Fletcher, M. J. Kwon, X. Rui, E. J. O'Loughlin, F. E. Loffler, and K. M. Kemner. Solution and microbial controls on the formation of reduced U(IV) species. Environmental Science & Technology, 45:8336 – 8344, 2011.

[28] S. C. Brooks, J. K. Fredrickson, S. L. Carroll, D. W. Kennedy, J. M. Zachara, A. E. Plymale, S. D. Kelly, K. M. Kemner, and S. Fendorf. Inhibition of bacterial U(VI) reduction by calcium. Environmental Science & Technology, 37:1850 – 1858, 2003.

[29] D. Burgge and R. Goble. The history of uranium mining and the Navajo People. American Journal of Public Health, 92(9):1410 – 1419, 2002.

[30] W. D. Burgos, J. T. McDonough, J. M. Senko, G. X. Zhang, A. C. Dohnalkova, S. D. Kelly, Y. Gorby, and K. M. Kemner. Characterization of uraninite nanoparticles produced by *shewanella oneidensis* MR-1. Geochimica et Cosmochimica Acta, 72(20):4901 – 4915, 2008.

[31] C. F. Cai, H. Dong, H. Li, X. Xiao, G. Ou, and C. Zhang. Mineralogical and geochemical evidence for coupled bacterial uranium mineralization and hydrocarbon oxidation in the Shashagetai Deposit, NW China. Chemical Geology, 236:167 – 179, 2007.

[32] C. F. Cai, H. Li, M. Qin, X. Luo, F. Wang, and G. Ou. Biogenic and petroleum-related ore-forming processes in the Dongsheng Uranium Deposit, NW China. Ore Geology Reviews, 32:262 – 274, 2007.

[33] K. M. Campbell, R. K. Kukkadapu, N. P. Qafoku, A. D. Peacock, E. Lesher, K. H. Williams, J. R. Bargar, M. J. Wilkins, L. Figueroa, J. Ranville, J. A. David, and P. E. Long. Geochemical, mineralogical and microbiological characteristics of sediment from naturally reduced zone in a uranium-contaminated aquifer. Applied Geochemistry, 29:1499 – 1511, 2012.

[34] J. M. Cerrato, M. N. Ashner, D. S. Alessi, J. S. Lezama-Pacheco, R. Bernier-Latmani, J. R. Bargar, and D. E. Giammar. Relative reactivity of biogenic and chemogenic uraninite and biogenic noncrystalline U(IV). Environmental Science & Technology, 47:9756 – 9763, 2013.

[35] V. S. Chakravarthy and J. M. Ottino. Mixing studies using horseshoes. International Journal of Bifurcation and Chaos, 5(2):519–530, 1995.

[36] Y.-J. Chang, P. E. Long, R. Geyer, A. D. Peacock, C. T. Resch, K. Sublette, S. Pfiffner, A. Smithgall, R. T. Anderson, H. A. Vrionis, J. R. Stephen, R. Dayvault, I. Ortiz-Bernad, D. R. Lovley, and D. C. White. Microbial incorporation of 13 ^{C}-labeled acetate at the field scale: Detection of microbes responsible for reduction of U(VI). Environmental Science & Technology, 39:9039 – 9048, 2005.

[37] D. L. Clark, D. E. Hobart, and M. P. Neu. Actinide carbonate complexes and their importance in environmental chemistry. Chemistry Review, 95, 1995.

[38] C. F. Jove Collon, C. Sanpawanichakit, H. Xu, R. T. Cygan, J. A. Davis, D. M. Meece, and R. L. Hervig. A combined analytical study to characterize uranium soil and sediment contamination: The case of the Naturita UMTRA site and the role of grain coatings. Technical report, Sandia National Laboratories, Albuquerque, NM, USA, 2006.

[39] C. E. Colten. A historical perspective on industrial wastes and groundwater contamination. Geographical Review, 81(2):215–228, 1991.

[40] Cameco Corporation. Uranium 101. online, 2017.

[41] National Research Council. Alternatives for managing the nation's complex contaminated groundwater sites. Technical report, National Research Council, 2013.

[42] J. P. Crimaldi, J. R. Cadwell, and J. B. Weiss. Reaction enhancement of isolated scalars by vortex stirring. Physics of Fluids, 2008.

[43] G. P. Curtis. Field scale model development conversation. Personal communication, October 2017.

[44] G. P. Curtis. Tracer test results discussion. Personal Communication, January 2017.

[45] G. P. Curtis, J. A. David, and D. I. Naftz. Simulation of reactive transport of uranium(VI) in groundwater with variable chemical conditions. Water Resources Research, 42(4), 2006.

[46] R. Danczak, S. Yabusaki, K. Williams, Y. Fang, C. Hobson, and M. J. Wilkins. Snowmelt induced hydrologic perturbations drive dynamic microbiological and geochemical behaviors across a shallow riparian aquifer. Frontiers in Earth Science, 4.10.3389/feart2016.0057, 2016.

[47] J. A. Davis and G. P. Curtis. Application of surface complexation modeling to describe uranium(VI) adsorption and retardation at the uranium tailings site at Naturita, Colorado. Technical report, United States Geological Survey, Menlo Park, California, USA, 2003.

[48] J. A. Davis, T. E. Payne, and T. D. Waite. Simulating the ph and pCO_2 dependence on uranium (vi) adsorption by a weathered schist with surface complexation models. In P.-C. Zhang and P. V. Brady, editors, Geochemistry of Soil Radionuclides, volume SSSA Special Publication Number 59, pages 61 – 86. Soil Science Society of America, Madison, WI, USA, 2002.

[49] J. A. Davis, T. E. Payne, and T. D. Waite. Simulating the pH and pCO_2 dependence of uranium(VI) adsorption by a weathered schist with surface complexation models. In P.-C. Zhang and P. V. Brady, editors, Geochemistry of Soil Radionuclides, volume SSSA Special Publication Number 59, pages 61 – 86. Soil Science Society of America, Madison, WI, 2002.

[50] M. Dentz and J. Carrera. Effective solute transport in temporally fluctuation flow through heterogeneous media. Water Resources Research, 2005.

[51] M. Descostes, Schlegel M. L., N. Eglizaud, F. Descamps, F. Miserque, and E. Simoni. Uptake of uranium and trace elements in pyrite (FeS_2) suspensions. Geochimica et Cosmochimica Acta, 74(5):1551 – 1562, 2010.

[52] J. L. Durhan, M. E. Conrad, K. H. Williams, L. N'Guessan, P. E. Long, and S. S. Hubbard. Sulfur isotopes as indicators of amended bacterial sulfate reduction processes. Environmental Science & Technology, 42:7842 – 7849, 2008.

[53] P. H. Eichstaedt. If You Poison Us. Red Crane Books, Sante Fe, NM, 1994.

[54] Y. Fang, S. B. Yabusaki, S. J. Morrison, J. P. Amonette, and P. E. Long. Multicomponent reactive transport modeling of uranium bioremediation field experiments. Geochimica et Cosmochimica Acta, 73(20):6029 – 6051, 2009.

[55] Y. Fang, S. B. Yabusaki, S. J. Morrison, J. P. Amonette, and P. E. Long. Multicomponent reactive transport modeling of uranium bioremediation field experiments. Geochimica et Cosmochimia Acta, 73:6029 – 6051, 2009.

[56] M. D. Finn, S. M. Cox, and H. M. Byrne. Mixing measures for a two-dimensional chaotic stokes flow. Journal of Engineering Mathematics, 2004.

[57] K. T. Finneran, R. T. Anderson, K. P. Nevin, and D. R. Lovley. Potential for bioremediation of uranium-contaminated aquifers with microbial U(VI) reduction. Soil and Sediment Contamination, 11:339 – 357, 2002.

[58] C. R. Fitts. Groundwater Science. Elsevier, Inc., 2 edition, 2013.

[59] K. E. Fletcher, M. I. Boyanov, S. H. Thomas, Q. Wu, K. M. Kemner, and F. E. L´offler. U(VI) reduction to mononuclear U(IV) by *desulfitobacterium* species. Environmental Science & Technology, 44:4705 – 4709, 2010.

[60] Inc. Ford, Bacon & Davis Utah. Naturita Site, Naturita, Colorado, engineering assessment of inactive uranium mill tailings. Technical report, United States Department of Energy, Albuquerque Operation Office, 1981.

[61] P. M. Fox, J. A. Davis, R. Kukkadapu, D. M. Singer, J. Bargar, and K. H. Williams. Abiotic U(VI) reduction by sorbed Fe(II) on natural sediments. Geochimica et Cosmochimica Acta, 117:266 – 282, 2013.

[62] P. M. Fox, J. A. Davis, and J. M. Zachara. The effect of calcium on aqueous uranium(VI) speciation and adsorption to ferrihydrite and quartz. Geochimica et Cosmochimica Acta, 70:1379 – 1387, 2006.

[63] M. Ginder-Vogel, B. Stewart, and S. Fendorf. Kinetic and mechanistic constraints on the oxidation of biogenic uraninite by ferrihydrite. Environmental Science & Technology, 44(1):163 – 169, 2010.

[64] Y. A. Gorby and D. R. Lovley. Enzymic uranium precipitation. Environmental Science & Technology, 26:205 – 207, 1992.

[65] J. A. Greene. Optimization of well placement for engineered injection and extraction during in situ groundwater remediation. In Proceedings of the World Environmental and Water Resources Congress, pages 185–192, 2016.

[66] I. Grenthe, J. Fuger, R. J. M. Konings R. J. Lemire, A. B. Muller, C. Nguyen-Trung, and H. Warner. Chemical Thermodynamics of Uranium, volume 1. North-Holland Amsterdam, 1992.

[67] D. Hadka and P. Reed. Borg: An auto-adaptive many-objective evolutionary computing framework. Evolutionary Computation, 21:231–259, 2013.

[68] K. J. Halford and R. T. Hanson. User guide for the drawdown-limited, multi-node well (MNW) package for the US Geological Survey's modular three-dimensional finite-difference ground-water flow model, versions MODFLOW-96 and MODFLOW-2000. Technical report, United States Geological Survey, Sacramento, CA, USA, 2002.

[69] A. W. Harbaugh. MODFLOW-2005, the US Geological Survey modular ground-water model – the ground-water flow process. In US Geological Survey Techniques and Methods, volume 6, chapter A16. United States Geological Survey, 2005.

[70] C. H. Ho and N. H. Miller. Formation of uranium oxide in soils in bicarbonate solutions. Journal of Colloid and Interface Science, 113(1):232 – 240, 1986.

[71] D. A. Holaday. History of the exposure of miners to radon. Health Physics, 16:547 – 552, 1969.

[72] D. E. Holmes, K. T. Finneran, R. A. O'Neil, and D. R. Lovley. Enrichment members of the family geobacteraceae associated with stimulation of dissimilatory metal reduction in uranium-contaminated aquifer sediments. Applied Environmental Microbiology, 68:2300 – 2306, 2002.

[73] K. T. Finneran M. E. Housewright and D. R. Lovley. Multiple influences of nitrate on uranium solubility during bioremediation of uranium-contaminated subsurface sediments. Environmental Microbiology, 4:510 – 516, 2002.

[74] B. Hua and B. L. Deng. Reductive immobilization of uranium(VI) by amorphous iron sulfide. Environmental Science & Technology, 42(23):8703 – 8707, 2008.

[75] B. Hua, H. F. Xu, J. Terry, and B. L. Deng. Kinetics of uranium(VI) reduction by hydrogen sulfide in anoxic aqueous systems. Environmental Science & Technology, 40(15):4666 – 4671, 2006.

[76] S. P. Hyun, J. A. Davis, K. Sun, and K. F. Hayes. Uranium(VI) reduction by Iron(II) monosulfide mackinawite. Environmental Science & Technology, 46(6):3369 – 3376, 2012.

[77] New Mexico Energy Institute. Uranium industry in New Mexico. Technical report, Albuquerque: Public Finance Research Program, University of New Mexico Energy Resources Board, 1976.

[78] J. P. Jaisi, H. L. Dong, and C. X. Liu. Influence of biogenic Fe(II) on the extent of microbial reduction of Fe(III) in clay minerals nontronite, illite, and chlorite. Geochimica et Cosmochimica Acta, 71:1145 – 1158, 2007.

[79] N. Janot, J. S. Lezama-Pacheco, D. Q. Pham, T. M. O'Brien, D. Hausladen, V. Noel, K. Maher, S. Fendorf, K. H. Williams, P. E. Long, J. R. Bargar, and F. Lallier. Physico-chemical heterogeneity of organic-rich sediments in the Rifle Aquifer, CO: Impact on uranium biogeochemistry. Environmental Science & Technology, 50(1):46 – 53, 2016.

[80] M. L. Jensen. Sulfur isotopes and the origin of sandstone-type uranium deposits. Economic Geology, 53:598 – 616, 1958.

[81] S. W. Jones and H. Aref. Chaotic advection in pulsed dipole sink systems. Physics of Fluids, 31(3):469–485, 1988.

[82] J. R. Kasprzyk, P. Reed, G. W. Characklis, and B. R. Kirsch. Many-objective *de novo* water supply portfolio planning under deep uncertainty. Environmental Modeling and Software, 34:87–104, 2012.

[83] M. C. Kavanaugh, P. Suresh, C. Rao, L. Abriola, J. Cherry, G. Destouni, R. Falta, D. Major, J. Mercer, C. Newell, T. Sale, S. Shoemaker, R. Siegrist, G. Teutsch, and K. Udell. The DNAPL remediation challenge: Is there a case for source depletion? Technical report, United States Environmental Protection Agency, 2003.

[84] S. D. Kelly, K. M. Kemner J. Carley, C. Criddle, P. M. Jardine, T. L. Marsh, D. Phillips, D. Watson, and W.-M. Wu. Speciation of uranium in sediments before and after in situ biostimulation. Environmental Science & Technology, 45:1558 – 1564, 2008.

[85] S. D. Kelly, W.-M. Wu, F. Yang, C. S. Criddle, T. L. Marsh, E. J. O'laughlin, B. Ravel, D. Watson, P. M. Jardine, and K. M. Kemner. Uranium transformations in static microcosms. Environmental Science & Technology, 44:236 – 242, 2010.

[86] M. Kohler, G. P. Curtis, D. B. Kent, and J. A. Davis. Experimental investigation and modeling of uranium(VI) transport under variable chemical conditions. Water Resources Research, 32(12):3539 – 3551, 1996.

[87] J. Komlos, R. K. Kukkadapu, J. M. Zachara, and P. R. Jaffe. Biostimulation of iron reduction and subsequent oxidation of sediment containing Fe-silicates and Fe-oxides: Effect of redox cycling on Fe(III) bioreduction. Water Resources Research, 41:2996 – 3004, 2007.

[88] J. Komlos, A. Peacock, R. K. Kukkadapu, and P. R. Jaffe. Long-term dynamics of uranium reduction/reoxidation under low sulfate conditions. Geochimica et Cosmochimica Acta, 72:3603 – 3615, 2008.

[89] R. K. Kukkadapu, J. M. Zachara, J. K. Fredrickson, J. P. McKinley, D. W. Kennedy, S. C. Smith, and H. L. Dong. Reductive biotransformation of Fe in shale-limestone saprolite containing Fe(III) oxides and Fe(II)/Fe(III) phyllosilicates. Geochimica et Cosmochimica Acta, 70:3662 – 3676, 2006.

[90] D. Langmuir. Aqueous Environmental Geochemistry. Prentice-Hall Inc., Upper Saddle River, NJ 07458, 1997.

[91] D. E. Latta, C. A. Gorski, M. I. Boyanov, E. J. O'Loughlin, K. M. Kemner, and M. M. Scherer. Influence of magnetite stoichiometry on U(VI) reduction. Environmental Science & Technology, 46(2):778 – 786, 2012.

[92] D. E. Latta, C. A. Gorski, M. I. Boyanov, E. J. O'Loughlin, K. M. Kemner, and M. M. Scherer. Influence of magnetite stoichiometry on U^{VI} reduction. Environmental Science & Technology, 46:778 – 786, 2012.

[93] D. E. Latta, K. M. Kemner, B. Mishra, and M. I. Boyanov. Effects of calcium and phosphate on Uranium(IV) oxidation: Comparison between nanoparticualte uraninite and amorphous U^{IV}–phosphate. Geochimica et Cosmochimica Acta, 174:122 – 142, 2016.

[94] D. E. Latta, B. Mishra, R. E. Cook, K. M. Kemner, and M. I. Boyanov. Stable U(IV) complexes form at high-affinity mineral surface sites. Environmental Science & Technology, 48(3):1683 – 1691, 2014.

[95] L. Li, C. I. Steefel, M. B. Kowalsky, A. Englert, and S. S. Hubbard. Effects of physical and geochemical heterogeneities on mineral transformation and biomass accumulation during biostimulation experiments at Rifle, Colorado. Journal of Contaminant Hydrology, 114:45 – 63, 2010.

[96] L. Li, C. I. Steefel, K. H. Williams, M. J. Wilkins, and S. S. Hubbard. Mineral transformation and biomass accumulation associate with uranium bioremediation at Rifle, Colorado. Environmental Science & Technology, 431:5429 – 5435, 2009.

[97] C. Liu, B.-H. Keon, J. M. Zachara, and Z. Wang. Influence of calcium on microbial reduction of solid phases U(VI). Biotechnology and Bioengineering, 97:1415 – 1422, 2007.

[98] P. E. Long. Microbiological, geochemical and hydrologic processes controlling uranium mobility: An Integrated Field Scale Subsurface Research Challenge Site at Rifle, Colorado February 2010 to January 2011. Technical report, United States Department of Energy Office of Science, Subsurface Biogeochemistry Research Program, 2011.

[99] P. E. Long, K. H. Williams, J. A. Davis, P. M. Fox, M. J. Wilkins, S. B. Yabusaki, Y. Fang, S. R. Waichler, E. S. F. Berman, M. Gupta, D. P. Chandler, C. Murray, A. D. Peacock, L. Giloteaux, K. M. Handley, D. R. Lovley, and J. F. Banfield. Bicarbonate impact on U(VI) bioreduction in a shallow alluvial aquifer. Geochimica et Cosmochimica Acta, 150:106 – 124, 2015.

[100] D. R. Lovley. Bioremediation of organic and metal contaminants with dissimilatory metal reduction. Journal of Industrial Microbioloy and Biotechnology, 14:89 – 93, 1995.

[101] D. R. Lovley, E. J. P. Phillips, Y. A. Gorby, and E. R. Landa. Microbial reduction of uranium. Nature, 350(6317):413 – 416, 1991.

[102] D. R. Lovley, E. E. Roden, E. J. P. Phillips, and J. C. Woodward. Enzymatic iron and uranium reduction by sulfate reducing bacteria. Marine Geology, 113:41 – 53, 1995.

[103] D. Lu, M. Ye, and G. P. Curtis. Maximum likelihood bayesian model averaging and its predictive analysis for groundwater reactive transport models. Journal of Hydrology, 529, 2015.

[104] M. T. Madigan, J. M. Martinko, P. V. Dunlap, and D. P. Clark. Brock Biology of Microorganisms. Pearson/Benjamin Cummings, San Francisco, 13 edition, 2010.

[105] D. C. Mays and R. M. Neupauer. Plume spreading in groundwater by stretching and folding. Water Resources Research, 48(7), 2012.

[106] M. Min, J. Chen, J. Wang, G. Wei, and M. Fayek. Mineral-hosted paragenesis and textures associated with sandstone-hosted roll-front uranium deposits, NW China. Ore Geology Reviews, 26:51 – 69, 2005.

[107] A. Mohaghegi, D. M. Updegraff, and M. B. Goldhaber. The role of sulfate-reducing bacteria in the deposition of sedimentary ores. Geomicrobiology Journal, 4(2):153 – 173, 1985.

[108] H. S. Moon, J. Komlos, and P. R. Jaffé. Biogenic U(IV) oxidation by dissolved oxygen and nitrate in sediment after prolonged U(VI)/Fe(III)/$SO_4{}^{2-}$ reduction. Journal of Contaminant Hydrology, 105(1 – 2):18 – 27, 2009.

[109] H. S. Moon, L. McGuinness, R. K. Kukkadapu, A. D. Peacock, J. Komlos, L. J. Kerkhof, P. E. Long, and P. R. Jaffe. Microbial reduction of uranium under iron- and sulfate- reducing conditions: Effect of amended goethite on microbial community composition and dynamics. Water Research, 44:415 – 428, 2010.

[110] S. J. Morrison, R. R. Spangler, and V. S. Tripathi. Adsorption of uranium(VI) on amorphous ferric oxyhydroxide at high-concentrations of dissolved carbon(IV) and sulfur(VI). Journal of Contaminant Hydrology, 17:333 – 346, 1995.

[111] S. J. Morrison, V. S. Tripathi, and R. R. Spangler. Coupled reaction transport modeling of a chemical barrier for controling uranium(VI) contamination in groundwater. Journal of Contaminant Hydrology, 17:347 – 363, 1995.

[112] L. N. Moyes, R. H. Parkman, J. M. Chamock, D. J. Vaughan, F. R. Livens, C. R. Hughes, and A. Braithwaite. Uranium uptake from aqueous solution by interactions with goethite, lepidocrocite, muscovite, and mackinawite: an x-ray absorption spectroscopy study. Environmental Science & Technology, 34:1062 – 1068, 2000.

[113] R. M. Neupauer and D. C. Mays. Engineered injection and extraction for in situ remediation of sorbing solutes in groundwater. Journal of Environmental Engineering, 141(6), 2015.

[114] R. M. Neupauer, J. D. Meiss, and D. C. Mays. Chaotic advection and reaction during engineered injection and extraction in heterogeneous porous media. Water Resources Research, 50:1433–1447, 2013.

[115] American Society of Civil Engineers. Ground water basin management. Technical report, American Society of Civil Engineers, 1961.

[116] United States Department of Energy. Soil and groundwater remediation.

[117] United States Department of Energy. United States mining and milling industry: A comprehensive review. a report to Congress from the President of the United States. Technical report, United States Department of Energy, Washington, DC, May 1984.

[118] United States Department of Energy. Environmental assessment of remedial action at the Naturita uranium processing site near Naturita, Colorado. Technical report, United States Department of Energy, Albuquerque Operation Office, Albuquerque, NM, 1994.

[119] United States Department of Energy. Site observational work plan for the Naturita, Colorado UMTRA Project site. Technical report, United States Department of Energy, 2002.

[120] United States Department of Energy. Environmental assessment of ground water compliance at Naturita, Colorado UMTRA Project site. Technical report, United States Department of Energy, 2003.

[121] United States Department of Energy. Legacy management geospatial environmental mapping system. Technical report, United States Department of Energy, 2012.

[122] United States Department of Energy Office of Legacy Management. Uranium mill tailings remediation control act sites, 2016.

[123] United States General Accounting Office. Report to congressional committees: Uranium mill tailings: Cleanup continues, but future costs are uncertain. Technical report, United States General Accounting Office, 1995.

[124] United States Government Accountability Office. Groundwater contamination DOD uses and develops a range of remediation technologies to clean up military sites. Technical report, United States Government Accountability Office, 2005.

[125] E. J. O'Loughlin, S. D. Kelly, R. E. Cook, R. Csencsits, and K. M. Kemner. Reduction of Uranium(VI) by mixed Iron(II)/Iron(III) hydroxide (green rust): Formation of UO_2 nanoparticles. Environmental Science & Technology, 37(4):721 – 727, 2003.

[126] Committee on the Biological Effects of Ionizing Radiation. Health Effects of Exposure to Radon (BEIR VI). National Academies Press, Washington, DC, USA, 1999.

[127] I. Ortiz-Bernad, R. T. Anderson, H. A. Vrionis, and D. R. Lovley. Resistance of solid-phase U(VI) to microbial reduction during in situ bioremediation of uranium-contaminated groundwater. Applied Environmental Microbiology, 70:7558 – 7560, 2004.

[128] J. M. Ottino. The Kinematics of Mixing: Stretching, Chaos, and Transport. Cambridge University Press, 1989.

[129] J. M. Ottino, S. C. Jana, and V. S. Chakravarthy. From reynolds stretching and folding to mixing studies using horseshoe maps. Physics of Fluids, 6(2):685–699, 1994.

[130] R. T. Pabalan, F. P. Bertetti, J. D. Prikryl, and D. R. Turner. Uranium(VI) sorption onto selected mineral surfaces: Key geochemical parameters. In Abstracts of Papers of the American Chemical Society. American Chemical Society, 1996.

[131] J. D. Pablo, L. Casas, J. Gimenez, M. Molera, M. Rovira, L. Duro, and J. Bruno. The oxidative dissolution mechanism of uranium dioxide. 1. the effect of temperature in hydrogen carbonate medium. Geochimica et Cosmochimica Acta, 63(19 – 20), 3097 – 3103.

[132] D. L. Parkhurst. Redox modeling. online, 2002.

[133] D. L. Parkhurst and C. A. J. Appelo. Description of input and examples for PHREEQC version 3 – a computer program for speciation, batch-reaction, one-dimensional transport, and inverse geochemical calculations. In US Geological Survey Techniques and Methods, volume 6, chapter A43, page 497. United States Geological Survey, 2013.

[134] J. Pearson. Hazard visibility and occupational health problem solving: the case of the uranium industry. Journal of Community Health, 6:136 – 147, 1980.

[135] J. M. Phillippi, V. A. Loganathan, M. J. McIndoe, T. P. Clement, and E. E. Roden. Theoretical solid/solution ratio effects on adsorption and transport: Uranium(vi) and carbonate. Soil Science Society of America Journal, 71(2):239 – 335, 2007.

[136] A. N. Piscopo, J. R. Kasprzyk, and R. M. Neupauer. An interative approach to multi-objective engineering design: Optimization of engineered injection and extraction for enhanced groundwater remediation. Environmental Modelling & Software, 69:253–261, 2015.

[137] A. N. Piscopo, R. M. Neupauer, and J. R. Kasprzyk. Optimal design of active spreading systems to remediate sorbing groundwater contaminants in situ. Journal of Contaminant Hydrology, 190:29 – 43, 2016.

[138] A. N. Piscopo, R. M. Neupauer, and D. C. Mays. Engineered injection and extraction to enhance reaction for improved in situ remediation. Water Resources Research, 49(6), 2013.

[139] M. Posfai, P. R. Buseck, D. A. Bazylinski, and R. B. Frankel. Reaction sequence of iron sulfide minerals in bacteria and their use as biomarkers. Science, 280(5365):880 – 883, 1998.

[140] S. W. Poulton. Sulfide oxidation and iron dissolution kinetics during the reaction of dissolved sulfide with ferrihydrite. Chemical Geology, 202:79 – 94, 2003.

[141] S. W. Poulton, M. D. Krom, and R. Raiswell. A revised scheme for reactivity of iron (oxy-hydr)oxide minerals towards dissolved sulfide. Geochimica et Cosmochimca Acta, 68(18):3703 – 3715, 2004.

[142] H. Prommer and V. Post. A Reactive Multicomponent Transport Model for Saturated Porous Media, 2.10 edition, 2010.

[143] A. J. Pyzik and S. E. Sommers. Sedimentary iron monosulfides: Kinetics of formation. Geochimica et Cosmochimica Acta, 45:687 – 698, 1981.

[144] A. E. Ray, J. R. Bargar, V. Sivaswamy, A. C. Dohnalkova, Y. Fujita, B. M. Peyton, and T. S. Magnuson. Evidence for multiple modes of uranium immobilzation by an anaerobic bacterium. Geochimica et Cosmochimia Acta, 75:2684 – 2695, 2011.

[145] R. L. Reynolds, M. B. Goldhaber, and D. J. Carpenter. Biogenic and nonbiogenic ore-forming processes in the South Texas Uranium District: Evidence from the panna maria deposit. Economic Geology, 77:541 – 556, 1982.

[146] D. T. Rickard. Kinetics and mechanism of the sulfidation of goethite. American Journal of Science, 274:941 – 952, 1974.

[147] D. T. Rickard. Kinetics of FeS precipitation: Part 1. competing reaction mechanisms. Geochimica et Cosmochimica Acta, 59(21), 1995.

[148] D. T. Rickard. The solubility of FeS. Geochimica et Cosmochimica Acta, 70(23):5779 – 5789, 2006.

[149] D. T. Rickard and G. W. Luther. Chemistry of iron sulfides. Chemical Reviews, 107:514 – 562, 2007.

[150] R. C. Ringholtz. Uranium Frenzy: Boom and Bust on the Colorado Plateau. WW Norton & Co, New York, NY, USA, 1989.

[151] P. Robinson. Uranium mill tailings remediation performed by the US DOE: An overview. Technical report, Southwest Research and Information Center, Albuquerque, NM, USA, 2004.

[152] R. K. Sani, B. M. Peyton, A. Dohnalkova, and J. E. Amonette. Reoxidation of reduced uranium and iron(III) (hydr)oxides under sulfate-reducing conditions. Environmental Science & Technology, 39(7):2059 – 2066, 2005.

[153] K. E. Saxton and W. J. Rawls. Soil water characteristic estimates by texture and organic matter for hydrologic solutions. Soil Science Society of America Journal, 70(5):1569 – 1578, 2006.

[154] M. A. A. Schoonen. Mechanisms of sedimentary pyrite formation. In J. P. Amend, K. J. Edwards, and T. W. Lyons, editors, Sulfur Biogeochemistry - Past and Present, pages 117 – 134. Geological Society of America Special Paper, Boulder, Colorado, 2004.

[155] G. L. Shumway. A History of the Uranium Industry on the Colorado Plateau. PhD thesis, University of Southern California, 1970.

[156] Robert L. Siegrist, Michelle Crimi, and Richard A. Brown. In situ chemical oxidation: Technology description and status. In Robert L. Siegrist, Michelle Crimi, and Thomas J. Simpkin, editors, In Situ Chemical Oxidation for Groundwater Remediation. Springer Science and Business Media, LLC, 2011.

[157] D. M. Singer, S. M. Chatman, E. S. Ilton, K. M. Rosso, J. F. Banfield, and G. W. Waychunas. Identification of simultaneous U(VI) sorption complexes and U(IV) nanoprecipitates on the magnetite (111) surface. Environmental Science & Technology, 46(7):3811 – 3820, 2012.

[158] D. M. Singer, K. Maher, and Jr. G. E. Brown. Uranyl-chlorite sorption/desorption: Evaluation of different U(VI) sequestration processes. Geochimica et Cosmochimica Acta, 73:59589 – 6007, 2009.

[159] V. Sivaswamy, M. I. Boyanov B. M. Peyton, S. Viamajala, R. Gerlach, W. A. Apel, R. K. Sani, A. Dohnalkova, K. M. Kemner, and T. Borch. Multiple mechanisms of uranium immobilization by *cellulomonas sp.* strain es6. Biotechnology and Bioegnineering, 108:264 – 276, 2011.

[160] F. N. Skomurski, S. Kerisit, and K. M. Russo. Structure, charge distribution, and electron hopping dynamics in magnetite (Fe_3O_4) (1 0 0) surfaces from first principals. Geochimica et Cosmochimica Acta, 74:4234 – 4248, 2010.

[161] G. Sposito. Chaotic solute advection by unsteady groundwater flow. Water Resources Research, 42(W06D03), 2006.

[162] N. F. Spycher, M. Issarangkun, B. D. Stewart, S. S. Seng'or, E. Belding, T. R. Ginn, B. M. Peyton, and R. K. Sani. Biogenic uraninite precipitation and its reoxidation by Iron(III) (hydr)oxides: A reaction model approach. Geochimica et Cosmochimica Acta, 75, 2011.

[163] B. Steinhardt. Testimony before the Subcomittee on Energy and Environment, Committee on Science, House of Representatives. Technical report, United States General Accounting Office, 1996.

[164] B. D. Stewart, J. Neiss, and S. Fendorf. Quantifying constraints imposed by calcium and iron on bacterial reduction of uranium(VI). Journal of Environmental Quality, 36:363 – 372, 2007.

[165] M. A. Stremler, F. R. Haselton, and H. Aref. Designing for chaos: Applications of chaotic advection at the microscale. Philosophical Transactions of the Royal Society A, 362(1818):1019–1036, 2004.

[166] H. F. Stroo and C. H. Ward, editors. In Situ Remediation of Chlorinated Solvent Plumes. Springer Science and Business Media, LLC, 2010.

[167] M. Stylo, D. S. Alessi, P. P. Shao, J. S. Lezama-Pacheco, J. R. Bargar, and R. Bernier-Latmani. Biogeochemical controls on the product of microbial U(VI) reduction. Environmental Science & Technology, 47:12351 – 12358, 2013.

[168] Y. Suzuki, S. D. Kelly, K. M. Kemner, and J. F. Banfield. Direct microbial reduction and subsequent preservation of uranium in natural near-surface sediment. Applied Environmental Microbiology, 71:1790 – 1797, 2005.

[169] M. Trefry, D. Lester, G. Metcalfe, A. Ord, and K. Regenauer-Lieb. Toward enhanced intervention methods using chaotic advection. Journal of Contaminant Hydrology, 127(1–4):15–29, 2012.

[170] National Park Service United States Department of the Interior. Vanadium Corporation of America (VCA) Naturita Mill. Technical report, Cultural Resource Historians, Fort Collins, CO, 1994.

[171] United States Environmental Protection Agency. Radiation protection. online, 2017.

[172] H. Veeramani, D. S. Alessi, E. I. Suvorova, J. S. Lezama-Pacheco, J. E. Stubbs, J. O. Sharp, U. Dippon, A. Kappler, J. R. Bargar, and R. Bernier-Latmani. Productions of abiotic U(VI) reduction by biogenic magnetite and vivianite. Geochimica et Cosmochimica Acta, 75(9):2512 – 2538, 2011.

[173] H. A. Vrionis, R. T. Anderson, I. Ortiz-Bernad, K. R. O'Neill, C. T. Resch, A. D. Peacock, R. Dayvault, D. C. White, P. E. Long, and D. R. Lovley. Microbiological and geochemical heterogeneity in an in situ uranium bioremediation field site. Applied and Environmental Microbiology, 71(10):6308 – 6318, 2005.

[174] T. D. Waite, J. A. Davis, T. E. Payne, G. A. Waychunas, and N. Xu. Uranium(VI) adsorption to ferrihydrite; application of a surface complexation model. Geochimica et Cosmochimica Acta, 58(24):5465 – 5478, 1994.

[175] Z. Wang, K.-U. Ulrich, C. Pan, and D. E. Giammar. Measurement and modeling of U(IV) adsorption to metal oxide minerals. Environmental Science & Technology Letters, 2:227 – 232, 2015.

[176] P. Wersin, Jr. M. F. Hochella, P. Persson, G. Redden, J. O. Leckie, and D. W. Harris. Interaction between aqueous Uranium(VI) and sulfide minerals: Spetroscopic evidence for sorption and reduction. Geochimica et Cosmochimica Acta, 58(13):2829 – 2843, 1994.

[177] Wikipedia. Uranium mining. online, 2017.

[178] K. H. Williams, P. E. Long, J. A. Davis, M. J. Wilkins, L. N'Guessan, C. I. Steefal, L. Yang, D. Newcomer, F. A. Spane, L. J. Kerkof, L. McGuinness, R. Dayvault, and D. R. Lovley. Acetate availability and its influence on sustainable bioremediation of uranium-contaminated groundwater. Geomicrobiology Journal, 28:519 – 539, 2010.

[179] W.-M. Wu, J. Carley, T. Gentry, M. A. Ginder-Vogel, M. Fienen, T. Mehlhorn, H. Yan, S. Caroll, M. N. Pace, J. Nyman, J. Luo, M. E. Gentile, M. W. Fields, R. F. Hickey, B. Gu, D. Watson, O. A. Cirpka, J. Zhou, S. Fendorf, P. K. Kitanidis, P. M. Jardine, and C. S. Criddle. Pilot-scale in situ bioremedation of uranium in a highly contaminated aquifer. 2. reduction of U(VI) and geochemical control of U(VI) bioavailability. Environmental Science & Technology, 40(12):3986 – 3995, 2006.

[180] S. Yabusaki, S. Sengor, and Y. Fang. A uranium bioremediation reactive transport benchmark. Computational Geosciences, 19(3):551 – 567, 2015.

[181] S. B. Yabusaki, Y. Fang, P. E. Long, C. T. Resch, A. D. Peacock, J. Komlos, P. R. Jaffe, S. J. Morrison, R. D. Dayvault, D. C. White, and R. T. Anderson. Uranium removal from groundwater via in situ biostimulation: Field-scale modeling of transport and biological processes. Journal of Contaminant Hydrology, 93:216 – 235, 2007.

[182] S. B. Yabusaki, Y. Fang, K. H. Williams, C. J. Murray, A. L. Ward, R. D. Dayvault, S. R. Waichler, D. R. Newcomer, F. A. Spane, and P. E. Long. Variably saturated flow and multicomponent biogeochemical reactive transport modeling of a uranium bioremediation field experiment. Journal of Contaminant Hydrology, 126:271 – 290, 2011.

[183] S. B. Yabusaki, M. J. Wilkins, Y. Fang, K. H. Williams, B. Arora, J. Bargar, H. R. Beller, N. J. Bouskill, E. L. Brodie, J. N. Christensen, M. E. Conrad, R. E. Danczak, E. King, M. R. Soltanian, N. F. Spycher, C. I. Steefel, T. K. Tokunga, R. Versteeg, S. R. Waichler, and H. M. Wainwright. Water table dynamics and biogeochemical cycling in a shallow variably-saturated floodplain. Environmental Science & Technology, 51:3307 – 3317, 2017.

[184] P. F. Zhang, S. L. Devries, A. Dathe, and A. C. Bagtzoglou. Enhanced mixing and plume containment in porous media under time-dependent oscillatory flow. Environmental Science & Technology, 43(16):6283–6288, 2009.

[185] C. Zheng and P. P. Wang. A modular three-dimensional multi-species transport model for simulation of advection, dispersion and chemical reactions of contaminants in groundwater systems: Documentation and user's guide. Technical report, United States Army Engineer Research and Development Center, Vicksburg, VA, 1999.

[186] Z. P. Zheng, T. K. Tokunaga, and J. M. Wan. Influence of calcium carbonate on U(VI) sorption to soils. Environmental Science & Technology, 37:5603 – 5608, 2003.

Appendix A

Non-technical Summary

Decades of uranium mining and processing activity throughout the American Southwest during the mid-20th century have left former sites contaminated with uranium. Until the beginning of the 21st century, processed ores left on these sites were subject to leaching of residual uranium left in ores into underlying aquifers. Remediation conducted by the United States Department of Energy (US DOE) removed most of the sources of uranium – processed tailings and former processing infrastructure. However, uranium entered underlying aquifers while these sources existed on sites. At the majority of sites, legal frameworks have been established to allow contaminants to exist at above normal regulatory levels. These frameworks also prohibit subsequent land and groundwater use at these sites. Although the sites are considered closed from a regulatory standpoint, elevated uranium concentrations still exist in underlying aquifers.

Uranium occurs in two valence states in the environment – U(VI) and U(IV). Much of the uranium present in aquifers from mining and processing sources occurs as U(VI), which forms aqueous complexes and therefore travels with ambient groundwater flow. Its counterpart, U(IV), forms solid phases and therefore does not travel with ambient groundwater flow. To cull regional transport of uranium present in groundwater, remediation techniques occurring in the subsurface attempt to transform U(VI) into U(IV) through stimulating native bacteria present in the contaminated aquifers. Injecting acetate, food for bacteria, promotes the growth of bacteria. Just as humans use oxygen to breathe, microbes present in aquifer environments can use metals and other compounds – iron, sulfur, and uranium – as part of their respiration. The respiration pro-

cess involves consumption of acetate coupled with the reduction of metals used in the respiration process. When uranium is used in the respiratory process, U(VI) is transformed to U(IV). This transformation is beneficial because it promotes the formation of uranium compounds that do not travel with groundwater flow and therefore do not spread contamination into previously unaffected areas.

Transformation of uranium facilitated by bacteria occurs over the course of months, so the injected acetate needs to remain at elevated concentrations in the uranium-contaminated area of the aquifer to promote a large amount of bacterial growth and subsequent uranium removal. However, regional groundwater flow decreases the concentrations of acetate present in the aquifer through attenuation. Lower acetate concentrations promote less bacterial growth and therefore less uranium is removed in areas with smaller acetate concentrations. The technique investigated here, called Engineered Injection and Extraction (EIE), involves injection and pumping of clean water from wells surrounding the aquifer area where acetate has been injected to combat attenuation of acetate in the aquifer. In this investigationm, this technique is tested for its ability to keep an elevated concentration of acetate in the aquifer against an *in situ* technique employed in field research at the Old Rife uranium contaminated site in Rifle, Colorado. This work uses a groundwater flow and reactive transport model developed based on physical and chemical conditions at the Naturita uranium contaminated site outside of Naturita, CO coupled with a biogeochemical reaction framework developed based on field work conducted at the Old Rifle site.

This work shows that EIE creates conditions within the aquifer to keep acetate present at an elevated concentration in the aquifer at the end the remediation period relative to the remediation system investigated at the Old Rifle site. This conclusion shows that EIE may be more effective at immobilizing uranium present in aquifers underlying the Naturita site.